UNIVERSIDADE FEDERAL DE MINAS GERAIS
Programa de Pós-Graduação em Engenharia Metalúrgica, Materiais e de Minas

TESE DE DOUTORADO

MODIFICAÇÃO SUPERFICIAL DO MAGNÉSIO LAMINADO A QUENTE PARA UTILIZAÇÃO EM ENGENHARIA DE TECIDOS ÓSSEOS

Autora: Jorgimara de Oliveira Braga
Orientador: Prof. Dr. Eduardo Henrique Martins Nunes

Setembro/2021

Jorgimara de Oliveira Braga

MODIFICAÇÃO SUPERFICIAL DO MAGNÉSIO LAMINADO A QUENTE PARA UTILIZAÇÃO EM ENGENHARIA DE TECIDOS ÓSSEOS

Tese de doutorado apresentada ao Programa de Pós-Graduação em Engenharia Metalúrgica, Materiais e de Minas da Escola de Engenharia da Universidade Federal de Minas Gerais, como requisito para obtenção do Grau de Doutora em Engenharia Metalúrgica, Materiais e de Minas.

Área de Concentração: Metalurgia física e de transformação.
Orientador: Prof. Dr. Eduardo Henrique Martins Nunes

Belo Horizonte
Universidade Federal de Minas Gerais
Escola de Engenharia
2021

Braga, Jorgimara de Oliveira.
B813m Modificação superficial do magnésio laminado a quente para utilização em engenharia de tecidos ósseos [recurso eletrônico] / Jorgimara de Oliveira Braga. - 2021.
1 recurso online (95 f. : il., color.) : pdf.

Orientador: Eduardo Henrique Martins Nunes.

Tese (doutorado) - Universidade Federal de Minas Gerais, Escola de Engenharia.

Apêndices: f. 94-95.

Inclui bibliografia.
Exigências do sistema: Adobe Acrobat Reader.

1. Engenharia metalúrgica - Teses. 2. Metalurgia física - Teses. 3. Metalurgia de Transformação - Teses. 3. Biocompatibilidade - Teses. 4. Corrosão - Teses. 5. Magnésio - Teses. 6. Revestimentos - Teses. I. Nunes, Eduardo Henrique Martins. II. Universidade Federal de Minas Gerais. Escola de Engenharia. III. Título.

CDU: 669(043)

Ficha catalográfica elaborada pelo bibliotecário Reginaldo Cesar Vital dos Santos CRB/6 2165
Biblioteca Prof. Mário Werneck, Escola de Engenharia da UFMG

UNIVERSIDADE FEDERAL DE MINAS GERAIS
ESCOLA DE ENGENHARIA
Programa de Pós-Graduação em Engenharia Metalúrgica, Materiais e de Minas

PPGEM

Tese intitulada **"Modificação superficial do magnésio laminado a quente para utilização em engenharia de tecido ósseo"**, área de concentração: Metalurgia de Transformação, apresentada pela candidata **Jorgimara de Oliveira Braga**, para obtenção do grau de Doutora em Engenharia Metalúrgica, Materiais e de Minas, aprovada pela comissão examinadora constituída pelos seguintes membros:

Prof. Eduardo Henrique Martins Nunes
Orientador - Dr. (UFMG)

Prof. Manuel Houmard
Dr. (UFMG)

Profª. Vanessa de Freitas Cunha Lins
Drª. (UFMG)

Prof. Fernando Cotting
Dr. (UFMG)

Prof. Marcello Rosa Dumont
Dr. (CEFET/MG)

Prof. Daniel Dornellas Athayde
Dr. (FUMEC)

Coordenador do Programa de Pós-Graduação em Engenharia Metalúrgica, Materiais e de Minas/UFMG

Belo Horizonte, 16 de setembro de 2021

Dedico esta tese ao meu orientador Prof. Eduardo Henrique Martins Nunes por todo apoio, amizade e ensinamentos durante o desenvolvimento deste trabalho.

AGRADECIMENTOS

Agradeço à Deus por ter me abençoado durante toda essa caminhada e me sustentado nos dias difíceis.

À minha mãe Maria José pelo amor incondicional, por sempre interceder por mim em suas orações e de fazer dos meus sonhos os seus também. Te amo!

Ao meu pai amado Reginaldo (*In memoriam*) que não presenciou em vida o quão longe eu cheguei, mas com certeza estaria muito orgulhoso.

À minha irmã Jorgileia e meu cunhado Rubem pelas orações, incentivo aos estudos e por estarem sempre dispostos a me ajudar.

À Mariana por ser a minha pessoa nesse mundo, melhor amiga e por compreender a ausência durante esse período.

Aos meus irmãos e sobrinhos pelo amor, torcida, momentos de alegria e descontração que vocês me proporcionam.

Ao Prof. Eduardo Nunes pela orientação humanizada nesse trabalho, encorajamento, disponibilidade e principalmente a amizade que construímos durante esse tempo. Serei eternamente grata por tudo.

Aos professores Vanessa Lins e Fernando Cotting por abrirem as portas do Laboratório de Engenharia de Superfície e Corrosão, pela contribuição nesse trabalho e as oportunidades que me deram durante esse período.

Ao Professor Manuel Hourmad pela valiosa contribuição em ideias, sugestões para melhorar o trabalho e disposição em nos ajudar.

Ao doutorando Diogo Maia por toda ajuda na execução do trabalho experimental e discussão do trabalho.

À Ursula pela grande amizade, conselhos, apoio e por sempre me lembrar de deixar os pés no chão e não desistir.

Aos amigos Dayana, Igor e Gustavo vocês foram os maiores presentes que o PPGEM me deu e imprescindíveis nessa jornada. Obrigada por toda ajuda.

Aos técnicos Patrícia, Leonardo e Samuel pela amizade e disponibilidade em realizar as análises desse trabalho.

Ao corpo docente do PPGEM-UFMG pelas excelentes aulas e oportunidade de aprendizado

Ao Programa de Engenharia Metalúrgica, Materiais e de Minas.

À CAPES pela bolsa concedida para realização desse trabalho.

RESUMO

O magnésio (Mg) é um material metálico não-ferroso com propriedades como baixa densidade e módulo de elasticidade próximo ao do osso humano. Trata-se de elemento essencial para o corpo humano, o que o torna um potencial candidato para produção de implantes ósseos. Contudo, sua alta taxa de corrosão e de liberação de gás hidrogênio em meios fisiológicos limitam sua utilização. Dessa forma, a investigação de estratégias para redução da taxa de corrosão do magnésio sem comprometer sua biocompatibilidade é um desafio enfrentado por diversos autores. Este trabalho consistiu em modificar a superfície do Mg com recobrimento cerâmico à base de fosfato dicálcico dihidratado (DCPD) e filme híbrido composto por álcool polivinílico (PVA) e vidro bioativo (BG). O Mg utilizado nesse estudo foi inicialmente processado por laminação a quente visando garantir que esse material possuísse resistência mecânica favorável para aplicação como implante ósseo. Os resultados obtidos nesse estudo são apresentados no formato de dois artigos científicos. O primeiro deles abordou a deposição do DCPD sobre o Mg por meio da sua imersão em banho de fosfatização. No segundo artigo se avaliou a deposição por processo *dip coating* de filme híbrido PVA/BG sobre o recobrimento de DCPD previamente produzido. Avaliou-se a estrutura, a resistência à corrosão em meio corpóreo simulado e a biocompatibilidade dos materiais preparados. Foi observado que a deposição do revestimento de DCPD aumenta a resistência à corrosão do Mg, além de promover uma rápida formação de hidroxiapatita (HAp) sobre o material. A formação de HAp é um importante indício da biocompatibilidade de um material, visto que se trata da fase mineral do osso humano, favorecendo a integração do biomaterial com o meio fisiológico. Ensaios de citometria de fluxo demonstraram que o material modificado com DCPD não apresentou toxicidade em células de rim de embrião humano. A posterior modificação da superfície do Mg/DCPD com filmes híbridos PVA/BG aumentaram ainda mais sua resistência à corrosão em fluido corporal simulado (*simulated body fluid*-SBF), alcançando valores superiores de módulo de impedância e melhor resposta de viabilidade celular (acima de 90%). Esse estudo contribui para uma aplicação mais efetiva do Mg em engenharia de tecidos ósseos.

PALAVRAS-CHAVE: Magnésio; corrosão; biocompatibilidade; engenharia de tecidos ósseos; revestimentos.

ABSTRACT

Magnesium (Mg) is a non-ferrous metallic material with properties such as low density and modulus of elasticity close to that of bone. It is an essential element for the human body, making it a potential candidate to produce bone implants. However, its high rate of corrosion and hydrogen gas release in physiological media limit its use. Thus, the investigation of strategies to reduce the corrosion rate of magnesium without compromising its biocompatibility is a challenge faced by several authors. This work consisted in modifying the Mg surface with a ceramic coating based on dicalcium phosphate dihydrate (DCPD) and a hybrid film composed of polyvinyl alcohol (PVA) and bioactive glass (BG). The Mg used in this study was initially processed by hot rolling to ensure that this material had favorable mechanical strength for application as a bone implant. The results obtained in this study are presented in the format of two scientific articles. The first one deals with the deposition of DCPD on Mg by means of its immersion in a phosphating bath. The second article evaluated the deposition by dip-coating process of a PVA/BG hybrid film on the previously produced DCPD coating. The structure, corrosion resistance in simulated body environment, and biocompatibility of the prepared materials were evaluated. It was observed that the deposition of the DCPD coating increases the corrosion resistance of Mg and promotes a rapid formation of hydroxyapatite (HAp) on the material. The formation of HAp is an important indication of the biocompatibility of a material since it is the mineral phase of human bone, which favors the integration of the biomaterial with the physiological environment. Flow cytometry test evaluated that the material modified with DCPD did not present toxicity in human embryonic kidney cells. Therefore, the subsequent surface modification of Mg/DCPD with PVA/BG hybrid films further increased its corrosion resistance in simulated body fluid (SBF), achieving higher impedance modulus values and better cell viability response (above 90%). This study contributes to a more effective application of Mg in bone tissue engineering.

KEYWORDS: Magnesium; corrosion; biocompatibility; bone tissue engineering; coatings.

LISTA DE FIGURAS

Figura 1 – (a) Fotografia de *scaffold* poroso da liga AZ91 e (b) modelo desenvolvido por simulação computacional (CAD – *Computer-Aided Design*). Adaptado de ZHENG *et al*. (2014)..... 20
Figura 2 – (a) Atividade metabólica de SAOS-2 expostas por 24 h a amostras de Mg obtidas por diferentes processamentos termomecânicos. (b) Status vital das células SAOS-2 determinado no ensaio LIVE / DEAD. Células vivas são indicadas pela fluorescência verde, enquanto as mortas são assinaladas pela cor vermelha. Adaptado de (SILVA *et al.*, 2017)). 21
Figura 3- Representação do processo de corrosão do Mg em meio fisiológico. Adaptado de ZHENG *et al.* (2014) 22
Figura 4- Diagrama E-pH para o sistema Mg-H_2O a 25 °C e 1 atm. 23
Figura 5 – Diagramas de Nyquist para diferentes tempos de OCP para o (a) Mg puro (b) e (c) compósito Mg/HAp. Adaptado de LOPES *et al.* (2020). 25
Figura 6 – Mg laminado e processado em 4 passes por (a) ECAP a 200 ºC com tamanho de grão próximo a 3,6 μm. (b) Material processado por ECAP em 4 passes a 300 ºC com tamanho de grão entre 100 e 200 μm. Adaptado de (a) (SILVA *et al.*, 2017) e (b) (SONG *et al.*, 2010). 26
Figura 7 – Microestruturas de Mg fundido e processado por ECAP (a) após 1, 2 e 4 passes. (b) Curvas de polarização potenciodinâmica obtidas em meio fisiológico HBSS. Adaptado de *(LI et al., 2013)*. 27
Figura 8 – Microestrutura da liga AZ31 processada por (a) laminação (tipo I) e (b) ECAP (tipo II). Diagrama de Nyquist das amostras tipo I e II em (c) NaCl e (d) PBS. Adaptado de (ALVAREZ-LOPEZ *et al.*, 2010). 28
Figura 9- Diagramas de Nyquist para o (a) Mg puro, Mg/DCPD e Mg/DCPD/HAp. (b) Mg puro e Mg/DCPD/HAp. (c) Circuito elétrico equivalente simulado para as amostras examinadas. Adaptado de (ZALUDIN *et al.*, 2018)..... 29
Figura 10 – Viabilidade de células L-929 expressa pela densidade óptica após (a) 1 dia e (b) 3 dias de ensaio sobre liga ZK60 não revestida, liga ZK60 revestida com DCPD e liga ZK60 revestida com DCPD e tratada termicamente. Adaptado de (LI et al., 2012). 30
Figura 11 – Morfologias da superfície do Mg revestido com BG/CaP imerso em solução de SBF por 7 dias (a − c), 15 dias (d − f) e 30 dias (g − i). Adaptado de (ZHANG *et al.*, 2014). 31

Figura 12 - Diagrama de Bode para liga Mg-Ca-Zn em SBF. 32
Figura 13 – Visão geral dos processos de revestimento a úmidos empregados na deposição de filmes inorgânicos e orgânicos. Adaptado de (HORNBERGER *et al.*, 2012). 33
Figure 14- XRD patterns taken in this study. The JCPDS cards used as the reference in these analyses are also shown for comparison purposes. 46
Figure 15-SEM micrographs of samples prepared in this work. The scale bars exhibited in these images correspond to either 100 or 500 μm. SEM images obtained using secondary electrons. 47
Figure 16 – (a) AFM images collected from the bare Mg substrate. (b) Thickness evaluated for the DCPD coating deposited on different samples. Inset: cross-sectional SEM micrograph of DCPD-coated sample obtained after 24 h of immersion in the phosphating bath. 47
Figure 17 – Bode plots obtained from EIS tests. (a) Phase angle and (b) impedance modulus as a function of frequency. (c) Impedance modulus evaluated at a constant frequency of 30 mHz. 50
Figure 18 – SEM micrographs and EDS spectra of samples previously used in the corrosion tests (CaP-24h and CaP-24h-HT). SEM images obtained with backscattered electrons. 51
Figure 19 – XRD patterns of CaP-24h before and after soaking in HBSS for 1 day. Similar patterns were obtained for samples soaked for different times and they are not displayed for sake of clarity. The JCPDS cards used as the reference in these analyses are also shown for reference purposes. 53
Figure 20 – ATR/FTIR spectra of CaP-24h before and after soaking in HBSS for different times. No normalization was applied to these spectra. 54
Figure 21 – SEM micrographs for (a) bare Mg substrate and (b) CaP-24h after soaking in HBSS for 21 days. (c) EDS spectrum collected over a selected area and (d) compositional map obtained for CaP-24h after the immersion step. Please refer to the online version of this paper to see Figure 7d in color. SEM micrographs obtained using secondary electrons. 56
Figure 22 – Results obtained from (a) LIVE/DEAD and (b) MTT assays. The scale bars displayed in Fig. 8a correspond to 100 μm. The dashed line exhibited in Fig. 24b is associated with a cell viability of 70%. 57
Figure 23 – SEM micrographs taken after the cell viability assays. (a) and (b) are associated with the bare Mg substrate and CaP-24h, respectively. The scale bars displayed in these images correspond to 50 μm. SEM images obtained with secondary electrons. 59
Figure 24 – Schematic representation of the methodology used to prepare the coated samples. 71

Figure 25 – (a) XRD pattern, (b) particle size distribution, (c) FTIR spectrum, and (d) N_2 sorption isotherm of the BG sample prepared here. Insets: (b) SEM micrograph of BG particles, and (d) pore size distribution evaluated by NLDFT method. 74
Figure 26 – SEM images of (a) bare and (b) DCPD-coated Mg substrates. (c) XRD patterns of an Mg sample before and after the deposition of DCPD on it. The JCPDS file numbers 35-0821 and 72-1240 were used as references for Mg and DCPD, respectively. 75
Figure 27 – SEM micrographs of Mg_DCPD_PVA/BG composites prepared using different BG loadings. The concentration of BG in (a), (b), and (c) are 2, 6, 10 vol.%, respectively. 76
Figure 28 – Composition map obtained by EDS for Mg_DCPD_PVA/BG (10 vol.%). 76
Figure 29 – Typical ATR-FTIR spectrum obtained for the Mg_DCPD_PVA/BG composites prepared here. The BG loading in this sample was 10 vol.%. Reference spectra of BG, CA, PVA, and DCPD are also exhibited in this Figure. 78
Figure 30 – Bode plots obtained from EIS tests: (a) phase angle and (b) impedance modulus as a function of frequency. Equivalent electrical circuits evaluated for (c) bare Mg and Mg_DCPD_PVA/BG, and (d) Mg_DCPD. Inset: cross-sectional SEM micrograph of Mg_DCPD_PVA/BG (10 vol.%). 80
Figure 31 – SEM micrographs of (a) bare Mg and (b) Mg_DCPD_PVA/BG (10 vol.%) after 7 days of soaking in SBF. The EDS spectrum exhibited in Figure 7b was taken at a HAp nodule. The inset displayed in this image brings an SEM micrograph of Mg_DCPD_PVA/BG (10 vol.%) after 21 days of soaking in SBF. 83
Figure 32 – ATR-FTIR spectra collected for Mg_DCPD_PVA/BG (10 vol.%) before and after immersion in SBF for 1, 3, and 7 days. A reference spectrum taken for a HAp sample is also exhibited. 84
Figure 33 – DRX patterns of Mg_DCPD_PVA/BG (10 vol.%) (a) before and (b) after its soaking in SBF for 7 days. The JCPDS cards used the reference for HAp, Mg, and DCPD are also displayed for comparison purposes. 85
Figure 34- SEM micrographs of Mg_DCPD_PVA/BG (10 vol.%) samples prepared using CA as a cross-linker for PVA. The concentrations of CA were kept at (a) 2 wt.%, (b) 6 wt.%, and (c) 10 wt% of the BG loading. The scale bars exhibited in these images correspond to either 20 μm or 100 μm. 87
Figure 35 - Flow cytometry results of HEK-293 cells seeded on the surface of Mg_DCPD_PVA/BG (10 vol.%). (a) Contour plot of FSC versus V450-A. (b) Density plot of SSC versus V450-A. (c) SSC versus FSC, where the live cells are represented by red dots and

the dead cells by purple dots. (d) Histograms of cells cultured on the composite surface and in the negative control group as a function of V450-A. 88
Figure 36- Light microscopy images of HEK-293 cells cultured in the negative control group or seeded on the Mg_DCPD_PVA/BG (10 vol.%) surface. The scale bars displayed in these images correspond to 20 μm. 89
Figura 37- Laminação do Mg comercialmente puro. (a) Mg passando através dos rolos de laminação e (b) Mg após o seu processamento. 101
Figura 38- Microestrutura do Mg (a) fundido e (b) laminado. 102

SIGLAS E ABREVIAÇÕES

ARB – colagem acumulativa de rolos (*accumulative roll bonding*).

BG – vidro bioativo (*bioactive glass*).

CaP – fosfato de cálcio (*calcium phosphate*).

DCPD – fosfato dicálcico dihidratado (*dicalcium phosphate dihydrate*).

ECAP – prensagem angular de canal igual (*equal channel angular pressing*).

EIS – espectroscopia de impedância eletroquímica (*electrochemical impedance spectroscopy*).

HAp – hidroxiapatita (*hydroxyapatite*).

HBSS – solução salina balanceada de Hank (*Hank's balanced salt solution*).

HPT – torção de alta pressão (*high pressure torsion*).

MAO – oxidação por micro arco (*micro arc oxidation*).

MSCs – células-tronco mesenquimais (*mesenchymal stem cells*)

MTT – 3-(4,5-dimethylthiazol-2-yl)-2,5-diphenyltetrazolium bromide.

OCP – circuito de potencial aberto (*open potential circuit*).

PVA – álcool polivinílico (*polyvinyl alcohol*)

SAOS – células humanas de osteosarcoma (*human osteosarcoma cells*).

SBF – fluido corporal simulado (simulated body fluid).

SCE – eletrodo saturado de calomelano (*saturated calomel electrode*).

UFG – grãos ultrafine (*ultrafine grains*).

SUMÁRIO

1. INTRODUÇÃO 16
2. OBJETIVOS 18
2.1. OBJETIVO GERAL 18
2.2. OBJETIVOS ESPECÍFICOS 18
3. REVISÃO DE LITERATURA 19
3.1. UTILIZAÇÃO DO MAGNÉSIO COMO BIOMATERIAL 19
3.2. CORROSÃO DO MG EM MEIOS FISIOLÓGICOS 22
3.3. ESTRATÉGIAS UTILIZADAS PARA AUMENTO DA RESISTÊNCIA À CORROSÃO DO MG 25
3.3.1. REFINAMENTO DE GRÃO 25
3.3.2. MODIFICAÇÃO DA SUPERFÍCIE DO MG COM REVESTIMENTOS BIOCOMPATÍVEIS 28
- MÉTODOS DE DEPOSIÇÃO DE REVESTIMENTOS 32
3.4. REFERÊNCIAS 34
4. OBTENÇÃO E CARACTERIZAÇÃO DE REVESTIMENTOS À BASE DE DCPD SOBRE SUBSTRATOS DE MAGNÉSIO 38
4.1. INTRODUCTION 40
4.2. MATERIALS AND METHODS 41
4.3. RESULTS AND DISCUSSION 44
4.4. CONCLUSIONS 59
4.5. REFERENCES 60
5. MODIFICAÇÃO DA SUPERFÍCIE DO MAGNÉSIO COM REVESTIMENTO COMPÓSITO PARA APLICAÇÃO EM ENGENHARIA DE TECIDO ÓSSEO 66
5.1. INTRODUCTION 68
5.2. MATERIALS AND METHODS 69
5.2.1. PREPARATION OF MG SUBSTRATES 69
5.2.2. SOL-GEL SYNTHESIS OF BG 69
5.2.3. COATING PROCESS 70

5.2.4. CHARACTERIZATIONS....71
5.2.5. *IN VITRO* ASSAYS....72
5.3. RESULTS AND DISCUSSION.... 73
5.3.1. STRUCTURAL CHARACTERIZATION....73
5.3.2. CORROSION TESTS....78
5.3.3. BIOLOGICAL ASSAYS....82
5.4. CONCLUSIONS.... 89
5.5. REFERENCES.... 90
6. CONSIDERAÇÕES FINAIS.... 98
6.1. CONCLUSÕES.... 98
6.2. SUGESTÕES PARA TRABALHOS FUTUROS.... 100
APÊNDICE.... 101
- PROCESSAMENTO MECÂNICO E CARACTERIZAÇÃO DO Mg UTILIZADO NESSE ESTUDO.... 101

1. INTRODUÇÃO

O magnésio (Mg) tem sido muito investigado nos últimos anos por ser um material biocompatível e não-tóxico, com grande potencial de aplicação em implantes biodegradáveis como placas, vasos conectores e parafusos, dentre outros itens essenciais em procedimentos cirúrgicos. O conceito da utilização de um material biodegradável como implante é bastante atrativo, visto que este só permaneceria no corpo até ser completamente absorvido, consumido e excretado, sem a necessidade de outra intervenção cirúrgica para retirá-lo (MORDIKE e EBERT, 2001). Contudo, a aplicação do Mg como implante ósseo exige que alguns requisitos sejam satisfeitos, valendo citar: boa resistência mecânica, integridade estrutural até que a região tratada esteja totalmente recuperada, boa resistência à corrosão e que os subprodutos de corrosão gerados não ocasionem efeitos adversos no paciente. Dessa forma, o maior desafio para a aplicação clínica desse material é a sua alta taxa de corrosão, visto que durante esse processo ocorre excessiva liberação de gás hidrogênio (H_2) e grupos hidroxila (OH^-). A formação dessas espécies pode gerar problemas como formação bolhas de gás e alcalinização do pH sanguíneo. Contudo, durante a oxidação do Mg tem-se também a liberação de íons Mg^{2+}, sendo este um elemento essencial para o corpo humano. Até o momento, nenhum estudo apontou que implantes biodegradáveis de magnésio leva a hipermagnesemia, ou seja, excesso de Mg^{2+} no corpo de forma maléfica (WANG *et al.*, 2016)

Dentre as estratégias citadas na literatura para redução da taxa de corrosão do Mg e suas ligas em meios fisiológicos, vale citar a adição de elementos químicos para produção de materiais biocompósitos, a modificação da sua microestrutura e a alteração da sua superfície (SHI *et al.*, 2009; SILVA *et al.*, 2017; ZALUDIN *et al.*, 2018; CASTRO *et al.*, 2019; BRAGA *et al.*, 2020). A modificação superficial do Mg por meio da deposição de filmes é uma forma efetiva de reduzir sua taxa de biocorrosão. Existem várias tecnologias disponíveis para esse fim como os processos de anodização, conversão química, oxidação por micro arcos e processamento sol-gel, dentre outros. Essas técnicas, além de mitigar a corrosão do Mg, contribuem para sua bioatividade, favorecendo sua interação com o tecido ósseo e o processo de osteogênese.

Este trabalho teve como principal objetivo investigar o efeito da deposição de revestimento à base de fosfato dicálcico dihidratado (DCPD) e filme híbrido composto por álcool polivinílico (PVA) e vidro bioativo (BG) sobre a taxa de corrosão e a biocompatibilidade de substratos de Mg previamente processados por laminação a quente. Os resultados obtidos são apresentados nesse documento no formato de dois artigos científicos. O primeiro deles abordou a deposição

do DCPD sobre o Mg por meio da sua imersão em banho fosfatizado. No segundo artigo se avaliou a deposição por processo de revestimento por imersão (*dip-coating*) de filme híbrido PVA/BG sobre o recobrimento de DCPD previamente produzido. Foram avaliadas as propriedades texturais, a taxa de corrosão em meio corpóreo simulado e a biocompatibilidade dos materiais preparados. O capítulo 2 dessa tese apresenta os objetivos geral e específicos desse estudo. O capítulo 3 traz uma revisão da literatura segundo o estado-da-arte do tema abordado. Nos capítulos 4 e 5 são apresentados e discutidos os resultados obtidos nesse estudo. No capítulo 6 são difundidas as principais conclusões decorrentes dessa pesquisa, bem como apresentadas sugestões para trabalhos futuros.

2. OBJETIVOS

2.1. OBJETIVO GERAL

Investigar o efeito da modificação superficial do Mg laminado a quente com DCPD e filme híbrido PVA/BG sobre sua resistência à corrosão, biocompatibilidade e citotoxicidade.

2.2. OBJETIVOS ESPECÍFICOS

- Realizar a modificação superficial do Mg por processo de conversão química para deposição de revestimento de DCPD.

- Realizar o tratamento superficial do Mg utilizando filme híbrido PVA/BG preparado por processo *dip coating*.

- Caracterizar os materiais obtidos segundo suas propriedades estruturais, de resistência à corrosão, biocompatibilidade e citotoxicidade.

3. REVISÃO DE LITERATURA

3.1. UTILIZAÇÃO DO MAGNÉSIO COMO BIOMATERIAL

Materiais metálicos desempenham importante papel como biomateriais, pois são capazes de reparar ou mesmo substituir o tecido ósseo comprometido em decorrência de processo de fratura ou degeneração. Ademais, metais suportam grandes esforços devido à sua elevada resistência mecânica e tenacidade à fratura em comparação a outros materiais(NASSIF e GHAYAD, 2013). Ainda é muito difundida a utilização como biomateriais do aço inoxidável, titânio e ligas à base de cromo e cobalto, apesar de esses materiais poderem exibir propriedades físicas e mecânicas bem diferentes daquelas observadas para o osso humano. O Mg apresenta características que o tornam um forte candidato para utilização como biomaterial. Trata-se de um material com menor densidade comparado ao alumínio e aço, com tenacidade à fratura maior que materiais cerâmicos. Ainda, possui módulo de elasticidade mais próximo ao do osso humano do que qualquer outro biomaterial comumente utilizado como implante ósseo (STAIGER *et al.*, 2006).

Diversos estudos têm sido realizados com o intuito de investigar a utilização do Mg e suas ligas como biomateriais. Essas pesquisas se basearam na avaliação das propriedades mecânicas, da resistência à corrosão, biocompatibilidade e citotoxicidade do Mg. Diferentes configurações de biomateriais à base Mg têm sido estudadas. ZHENG *et al.* (2014) prepararam amostras porosas com geometria de arcabouços (*scaffolds*) (Figura 1). Materiais com tal porosidade permitem a migração de tecidos, vasos sanguíneos e células através da sua estrutura. WITTE *et al.* (2007) desenvolveram compósito utilizando matriz da liga AZ91 (composição mássica (%): 90 Mg – 9 Al – 1 Zn) reforçada com partículas de HAp. Observou-se que o material preparado apresentou boa biocompatibilidade. Os autores notaram que a distribuição de tamanho e o arranjo das partículas de HAp possuem grande efeito sobre as propriedades mecânicas e corrosivas do material.

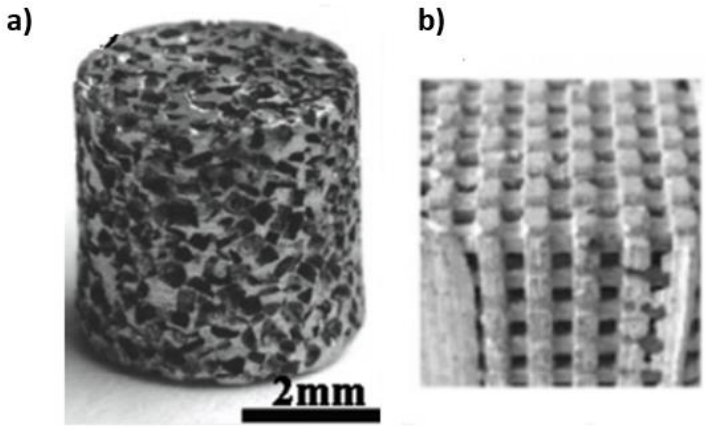

Figura 1 – (a) Fotografia de *scaffold* poroso da liga AZ91 e (b) modelo desenvolvido por simulação computacional (CAD – *Computer-Aided Design*). Adaptado de ZHENG *et al*. (2014).

A citotoxicidade de um material é fundamental para a avaliação da sua utilização como biomaterial. No que se refere ao Mg, tais ensaios permitem avaliar os efeitos nocivos provocados pelo aumento de pH e pela liberação de íons Mg^{2+} durante a degradação do Mg no organismo. ZHEN *et al.* (2015) investigaram a compatibilidade celular e a hemocompatibilidade do Mg. Foi observado que o processo de hemólise, caracterizado pela ruptura da membrana das hemácias e a consequente liberação de hemoglobina e outras substâncias no sangue, está mais relacionado ao aumento de pH do meio fisiológico do que com o aumento da concentração de íons Mg^{2+} devido à corrosão do Mg. SILVA *et al.* (2017) estudaram amostras de Mg processadas por diferentes técnicas de deformação plástica severa, com objetivo de reduzir o tamanho de grão do material e verificar o impacto dessa propriedade em sua biocompatibilidade. Foi observado que o Mg processado por técnicas como fundição, laminação e deformação plástica severa (prensagem angular de canal igual (ECAP – *equal channel angular pressing*) e torção de alta pressão (HPT – *high pressure torsion*) não apresentaram citotoxicidade a células humanas de osteosarcoma (SAOS-2) (Figura 2). Análises quantitativas conduzidas pela técnica de MTT (3-(4,5-dimethylthiazol-2-yl)-2,5-diphenyltetrazolium bromide) indicaram que células expostas por 24 h ao Mg não apresentaram alterações significativas em sua atividade metabólica mitocondrial. Ainda, se observou que os grupos testados produziram níveis de função celular acima de 50%. A análise de citotoxicidade usando o método LIVE / DEAD revelaram de forma qualitativa que boa parte das células expostas a materiais à base de Mg por 24 h se mantiveram vivas. Nesse teste células vivas exibem fluorescência verde, enquanto as mortas se mostram vermelhas. As células vivas foram

observadas em grande concentração em todos os grupos examinadas, indicando que os resultados de LIVE / DEAD estão de acordo com aquele obtido por MTT.

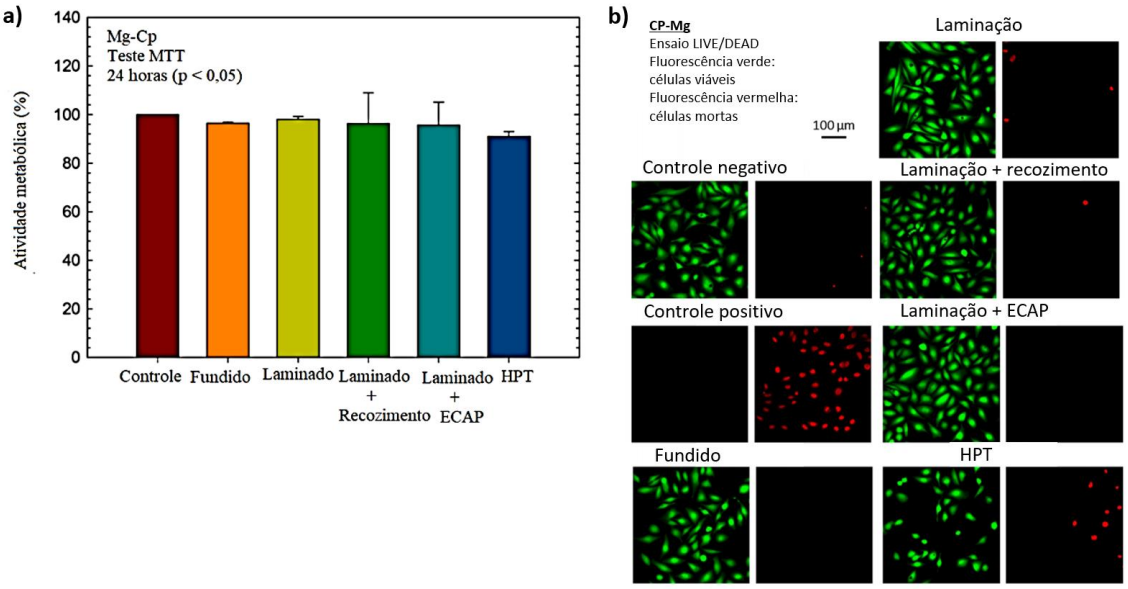

Figura 2 – (a) Atividade metabólica de SAOS-2 expostas por 24 h a amostras de Mg obtidas por diferentes processamentos termomecânicos. (b) Status vital das células SAOS-2 determinado no ensaio LIVE / DEAD. Células vivas são indicadas pela fluorescência verde, enquanto as mortas são assinaladas pela cor vermelha. Adaptado de (SILVA *et al.*, 2017)).

Em outro trabalho conduzido por LOPES *et al.* (2019), foram avaliadas amostras de Mg e algumas de suas ligas obtidas pelo processo HPT. Os ensaios de citotoxicidade realizados não indicaram diferenças significativas na atividade mitocondrial de células expostas às diferentes ligas por 24 h em comparação ao grupo controle negativo. A atividade metabólica celular foi superior a 80%, indicando uma alta viabilidade celular. Os resultados de LIVE / DEAD indicaram que a maioria das células expostas às amostras de Mg por 24 h preservou o seu status vital. CASTRO *et al.* (2019) processaram tanto o Mg quanto a liga AZ91 em conjunto com partículas de HAp e BG 58S (composição em peso (%): 58 SiO_2 – 33 CaO – 9 P_2O_5) para produção de compósitos bioativos. Nesse trabalho as partículas de BG e HAp foram incorporadas e compactadas em conjunto com partículas de Mg e da liga AZ91. Foi observada rápida corrosão nos compósitos com vidro bioativo e, após duas horas de imersão em solução de Hank (HBSS – *Hanks balanced salt solution*), notou-se a deposição de CaP na superfície dos materiais. Contudo, os compósitos com HAp exibiram melhor desempenho em relação à corrosão, além de melhor resposta nos ensaios mecânicos.

3.2. CORROSÃO DO Mg EM MEIOS FISIOLÓGICOS

A maior preocupação com relação à utilização do Mg como biomaterial se refere à sua corrosão acelerada em meios fisiológicos. Como demonstrado na Equação (3.1), a corrosão do Mg culmina na formação de gás hidrogênio (H_2) e na liberação de íons Mg^{2+} para o meio. A formação dessas espécies pode gerar problemas como a formação bolhas de gás e a alcalinização do pH sanguíneo (SONG e SONG, 2007).

$$Mg_{(s)} + 2H_2O_{(l)} \longrightarrow Mg^{2+}_{(aq.)} + 2OH^-_{(aq.)} + H_{2(g)} \quad (3.1)$$

Na Figura 3 é ilustrado o mecanismo de corrosão do Mg em meio fisiológico. Inicialmente observa-se a oxidação do metal e a liberação de cátions Mg^{2+} para o meio. Os cátions gerados podem reagir com íons OH^- provenientes da redução da água, dando origem a uma camada de $Mg(OH)_2$ sobre a superfície do Mg (Equação (3.2)).

$$Mg^{2+}_{(aq.)} + 2OH^-_{(aq.)} \longrightarrow Mg(OH)_{2(s)} \quad (3.2)$$

Entretanto, a camada de $Mg(OH)_2$ não resiste por muito tempo na superfície do material, pois a solução fisiológica é rica em íons cloreto que rompem essa camada protetora (ZHENG *et al.*, 2014).

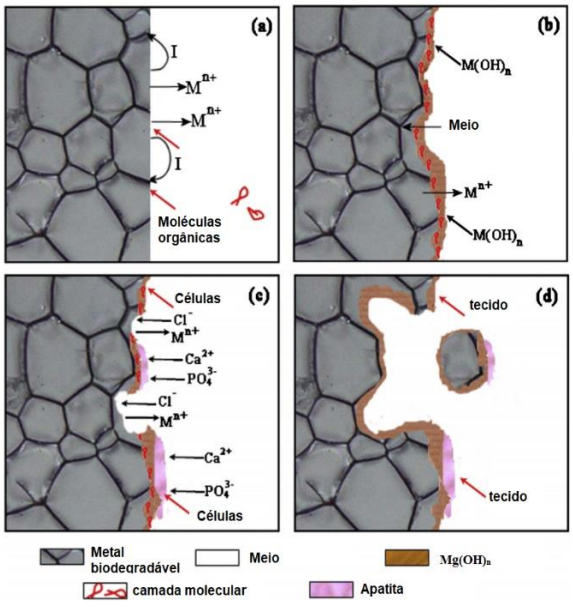

Figura 3- Representação do processo de corrosão do Mg em meio fisiológico. Adaptado de ZHENG *et al.* (2014)

O comportamento eletroquímico do Mg e suas ligas ainda tem sido destaque em muitos estudos devido à sua importância tecnológica. Do ponto de vista da corrosão, o Mg é altamente reativo em ambientes aquosos. Isto se deve em parte ao seu potencial altamente negativo, em torno de -2,37 V_{NHE}. Ainda, deve-se considerar que a reação catódica resultante dessa corrosão é a redução da água, conforme mostrado na Equação (3.3).

$$2H_2O_{(l)} + 2e^- \longrightarrow H_{2(g)} + 2OH^-_{(aq.)} \quad (3.3)$$

Nota-se que a Equação (3.3) ocorre sem a necessidade da presença de oxigênio. Isso permite que a corrosão do Mg ocorra livremente em pH inferiores a 11, como mostrado no diagrama exibido na Figura 4 (BIRBILIS *et al.*, 2013).

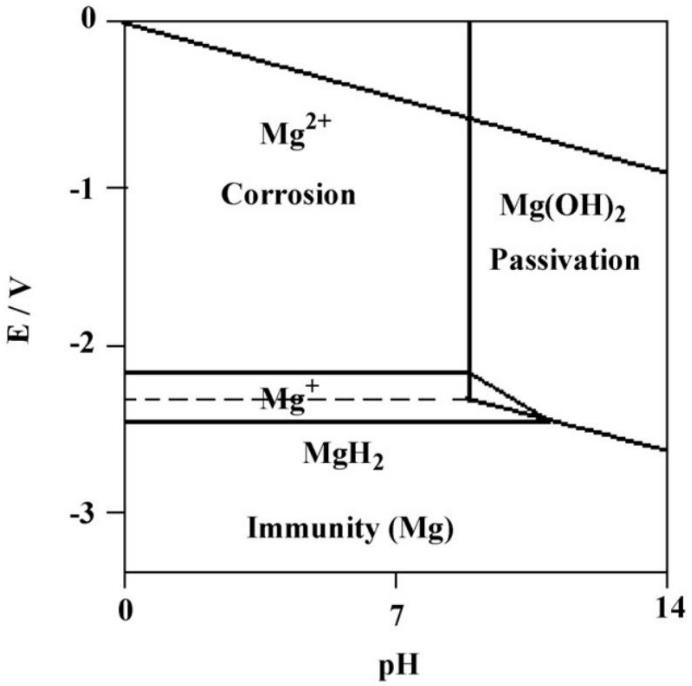

Figura 4- Diagrama E-pH para o sistema Mg-H_2O a 25 °C e 1 atm.
Adaptado de (POURBAIX, 1974).

A partir do diagrama de Pourbaix (Figura 4) é possível obter informações importantes sobre a estabilidade do Mg em meios aquosos, o qual todo o domínio de estabilidade do magnésio está bem abaixo do da água. O magnésio, portanto, se dissolve como Mg^+ e Mg^{2+} juntamente com a evolução de hidrogênio.

Tratando-se de Mg em fluido corporal simulado, observa-se que este reage fortemente com a água, líquido abundante em fluido corporal, produzindo H_2 e $Mg(OH)_2$ de acordo com o

mostrado no diagrama de Pourbaix e com as reações apresentadas pelas equações 3.1 e 3.2. Em ambientes com pH elevado (acima de 11,5), o $Mg(OH)_2$ atua como uma camada protetora sobre a superfície do Mg. Contudo, em pH inferiores o $Mg(OH)_2$ é instável, ocorrendo a corrosão do Mg (SALAHSHOOR e GUO, 2012).

É importante compreender o processo de corrosão do Mg em fluido corpóreo simulado (SBF – *simulated body fluid*), para então desenvolver um biomaterial baseado nesse metal. WANG *et al.* (2008) investigaram processos físicos e químicos observados quando o Mg é mantido no SBF por diferentes tempos. Os autores notaram que o Mg degrada de forma heterogênea, sendo que sua taxa de corrosão aumenta com o tempo de imersão via processo de corrosão localizada. KALB *et al.* (2012) também pesquisaram a corrosão do Mg quando imerso em SBF. Foi observado mecanismo de corrosão micro galvânica devido à presença de partículas catódicas de ferro. Nesse processo, o ferro proveniente de impurezas age como um cátodo micro galvânico, favorecendo a corrosão. ZENG *et al.* (2015) avaliaram a resposta à corrosão do Mg em soluções de HBSS e de cloreto de sódio (NaCl, 0,9% vol./vol.). Os autores variaram os teores de glicose nessas soluções de modo simular o comportamento do Mg em pessoas portadoras de diabetes. Foi observado que a taxa de corrosão do Mg aumentou com a elevação do teor de glicose na solução de NaCl, devido à diminuição de pH em decorrência da transformação da glicose ($C_6H_{12}O_6$) em ácido glucônico ($C_6H_{12}O_7$). Esse efeito promove a absorção de íons cloreto de forma mais acelerada sobre a superfície do Mg. Contudo, na solução de HBSS o aumento do teor de glicose diminui a taxa de corrosão do Mg. Isso se deve à associação da glicose a íons Ca^{2+} na solução HBSS, promovendo a formação de compostos à base de fosfato de cálcio (CaP) na superfície do Mg (ZENG *et al.*, 2015).

LOPES *et al.* (2020) estudaram o comportamento corrosivo do Mg quando associado à HAp em HBSS. A incorporação da HAp no Mg foi conduzida por meio de processamento HPT. O ensaio de impedância eletroquímica (EIS – *electrochemical impedance spectroscopy*) com diferentes tempos de estabilização do potencial de circuito aberto (OCP – *open circuit potential*) foi uma das formas de analisar a corrosão. Foi observado que o material compósito produzido exibe impedância mais baixa que o Mg puro após curtos tempos de imersão em HBSS (Figura 5). A maior resistência à corrosão do compósito Mg/HAp foi atribuída à formação de camada protetora à base de MgO e de compostos ricos em Ca, P e O sobre a superfície do material.

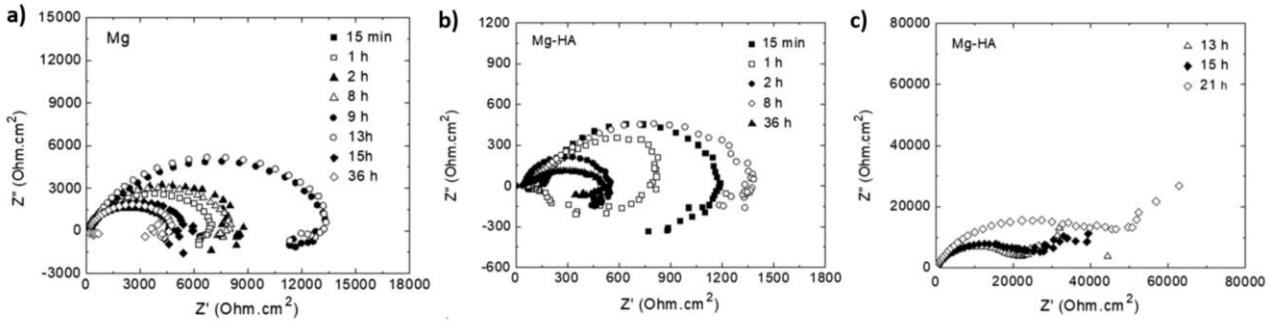

Figura 5 – Diagramas de Nyquist para diferentes tempos de OCP para o (a) Mg puro (b) e (c) compósito Mg/HAp. Adaptado de LOPES *et al.* (2020).

3.3. ESTRATÉGIAS UTILIZADAS PARA AUMENTO DA RESISTÊNCIA À CORROSÃO DO Mg

3.3.1. REFINAMENTO DE GRÃO

O Mg possui baixa resistência à corrosão em meios fisiológicos, acarretando na fragilização do material. Como consequência, a utilização do Mg como biomaterial é comprometida pela ocorrência da sua degradação, fato que o impede de suportar grandes solicitações mecânicas por longos tempos (SAHA *et al.*, 2015). Dessa forma, estudos têm sido realizados para contornar o problema da corrosão do Mg e a consequente perda de estabilidade mecânica. Nesse contexto, técnicas de processamento termomecânico têm sido utilizadas para refinar os grãos do Mg e aumentar sua resistência à corrosão. Dentre os métodos mais difundidos, vale citar laminação e técnicas de deformação plástica severa, incluindo ECAP, HPT e colagem acumulativa de rolos (ARB – *accumulative roll bonding*) (SAHA *et al.*, 2015; MIYAMOTO, 2016). É sabido que o tamanho de grão possui influência direta sobre o mecanismo de corrosão do Mg; a ocorrência de corrosão localizada e corrosão intragranular diminui com a redução do tamanho de grão do material. Contudo, o mecanismo de corrosão generalizada é favorecido quando o tamanho de grão do Mg é reduzido (MIYAMOTO, 2016).

SONG *et al.* (2010) avaliaram o efeito do refino de grão do Mg por ECAP sobre seu comportamento corrosivo utilizando solução salina contendo NaCl. Os autores observaram que o refino de grãos ocasionou na reduçao da resistência à corrosao do Mg. Por outro lado, SILVA *et al.* (2017) obtiveram resultados contrários àqueles descritos por SONG *et al.* (2010). Os autores justificaram tal efeito ao maior refinamento de grão atingido em razão de diferenças no

processamento termomecânico utilizado. A Figura 6 exibe micrografias de materiais preparados nos dois estudos. Nota-se que o tamanho de grão é menor na amostra 6a do que na 6b.

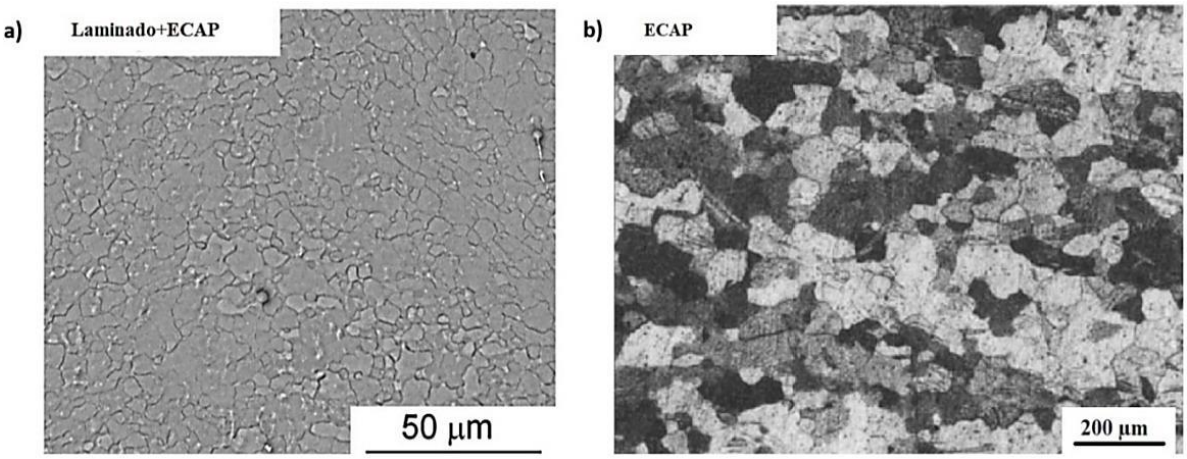

Figura 6 – Mg laminado e processado em 4 passes por (a) ECAP a 200 ºC com tamanho de grão próximo a 3,6 μm. (b) Material processado por ECAP em 4 passes a 300 ºC com tamanho de grão entre 100 e 200 μm. Adaptado de (a) (SILVA *et al.*, 2017) e (b) (SONG *et al.*, 2010).

O efeito do refino de grão do Mg sobre sua resistência à corrosão também foi avaliado por LI *et al.* (2013). Na Figura 7a é observado que o material fundido apresentou granulometria bastante grosseira (1500 μm). Após a deformação do material por ECAP em diferentes temperaturas (primeiro passe a 360 ºC e os demais a 200 ºC), houve considerável refino de grão e aumento da resistência à corrosão do Mg (Figura 7b). Notou-se que o material processado em dois passes apresentou potencial de corrosão mais nobre e maiores correntes de corrosão. Para passes adicionais esse potencial reduziu. Além disso, a corrente de corrosão indicou uma tendência de variação similar para os diferentes números de passes.

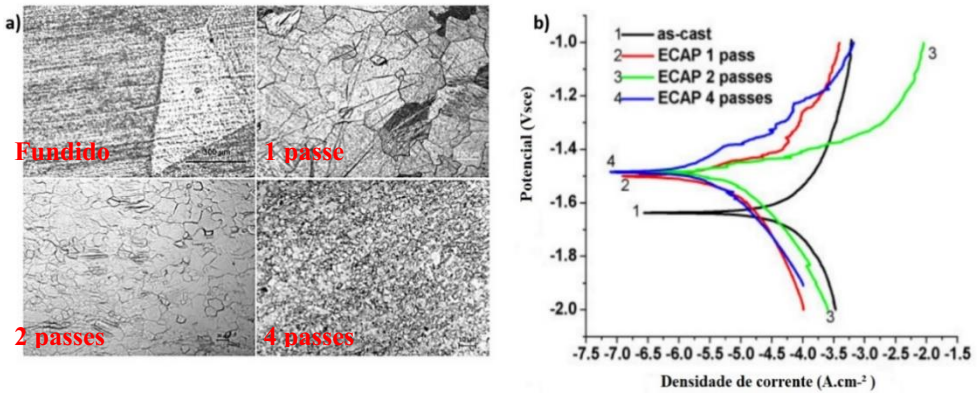

Figura 7 – Microestruturas de Mg fundido e processado por ECAP (a) após 1, 2 e 4 passes. (b) Curvas de polarização potenciodinâmica obtidas em meio fisiológico HBSS. Adaptado de *(LI et al., 2013)*.

ALVAREZ-LOPEZ *et al.* (2010) estudaram o efeito do tamanho de grão sobre o comportamento eletroquímico da liga AZ31 (composição mássica (%): 97 Mg – 2,5-3,5 Al – 0,6-1,4 Zn – 0,2 Mn) em solução de NaCl (8 $g.L^{-1}$) e soro fisiológico fosfatado (PBS – *phosphate-buffered saline*). As ligas estudadas foram submetidas a diferentes tipos de processamento, tais como laminação (tipo I) e ECAP seguido de laminação (tipo II). Os resultados reportados apontaram uma maior resistência à corrosão para o material com granulometria mais refinada. Foi também notado que o meio fisiológico também teve influência significativa nos resultados obtidos. A solução PBS induziu a formação de um composto compacto contendo fósforo que juntamente com o $Mg(OH)_2$, garantiu uma maior proteção da superfície do material contra o ataque de íons cloreto. A Figura 8 apresenta as microestruturas observadas após o processamento do Mg, bem como os ensaios eletroquímicos realizados.

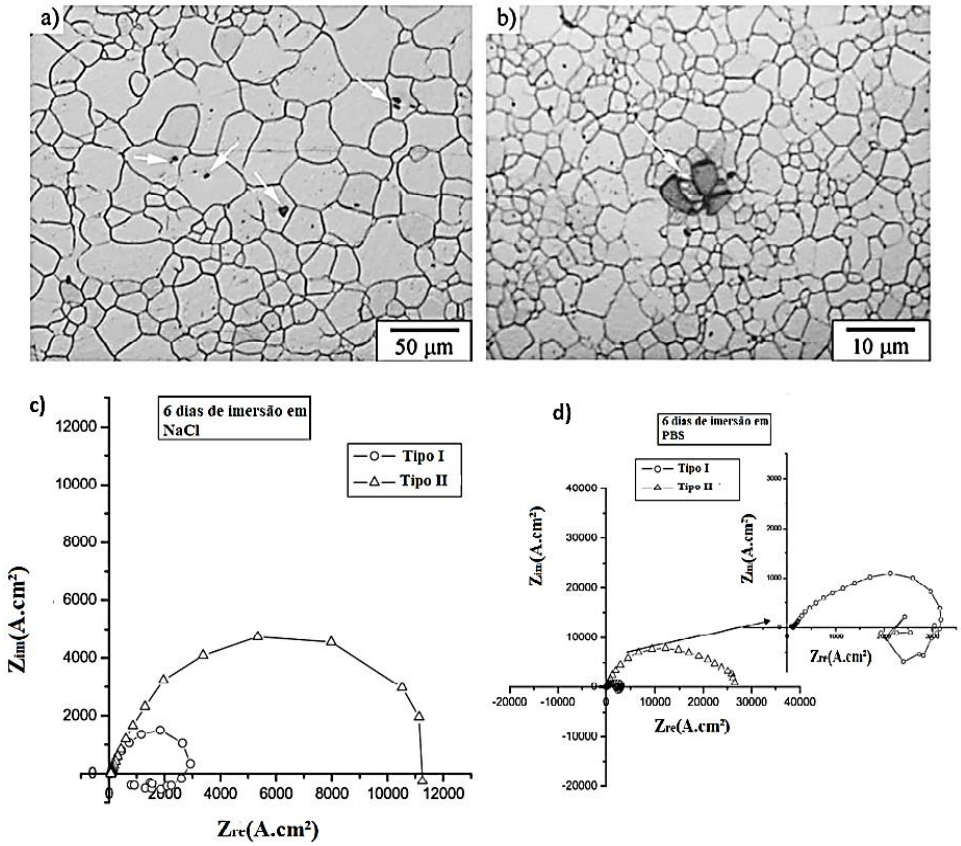

Figura 8 – Microestrutura da liga AZ31 processada por (a) laminação (tipo I) e (b) ECAP (tipo II). Diagrama de Nyquist das amostras tipo I e II em (c) NaCl e (d) PBS. Adaptado de (ALVAREZ-LOPEZ *et al.*, 2010).

3.3.2. MODIFICAÇÃO DA SUPERFÍCIE DO Mg COM REVESTIMENTOS BIOCOMPATÍVEIS

Os fosfatos de cálcio pertencem ao grupo de minerais denominados ortofosfatos. Estruturas biológicas como ossos e dentes os contêm em suas composições. As fases presentes em ortofosfatos são classificadas de acordo com a razão Ca/P que possuem. Dentre esses materiais, vale citar o DCPD, a HAp e o fosfato tricálcico (TCP – *tricalcium phosphate*) (SHADANBAZ e DIAS, 2012).

CHENG *et al.* (2014) depositaram camada de DCPD sobre substrato de AZ91. Nesse estudo os autores utilizaram banhos de fosfatização com diferentes teores de $C_6H_4O_5NSNa$ e Na_2MoO_4, com objetivo de uniformizar e densificar o recobrimento. Observou-se que a adição de Na_2MoO_4 deu origem ao molibdato de magnésio ($MgMoO_4$) que atuou como sítio de nucleação e crescimento de cristais de fosfatos. Foi também notada a influência do pH do banho de

fosfatização sobre a formação do recobrimento. Em pH 2,5 notou-se que o substrato de Mg foi consumido, havendo liberação de grande fração de $H_{2(g)}$. Quando o pH do banho foi ajustado para 3,0, um revestimento uniforme e denso foi obtido. Para valores superiores de pH foram obtidos revestimentos porosos, compostos por longos cristais de fosfato.

ZALUDIN *et al.* (2018) avaliaram o comportamento eletroquímico de substratos de Mg modificados com DCPD por meio de ensaios de polarização potenciodinâmica e EIS (Figura 9). Os autores também realizaram deposições com um subsequente tratamento alcalino com objetivo de obter HAp estabilizada na camada de DCPD. As Figuras 9a e 9b mostram as análises eletroquímicas de EIS e revelam que ambos os revestimentos melhoraram a resistência à corrosão do Mg em SBF. Contudo, o revestimento sem tratamento alcalino (curva vermelha na Figura 9a) composto unicamente por DCPD apresentou maior resistência à corrosão em comparação àquele preparado por tratamento alcalino. Notou-se que o tratamento alcalino provocou a erosão da superfície das amostras tratadas, diminuindo sua resistência à corrosão.

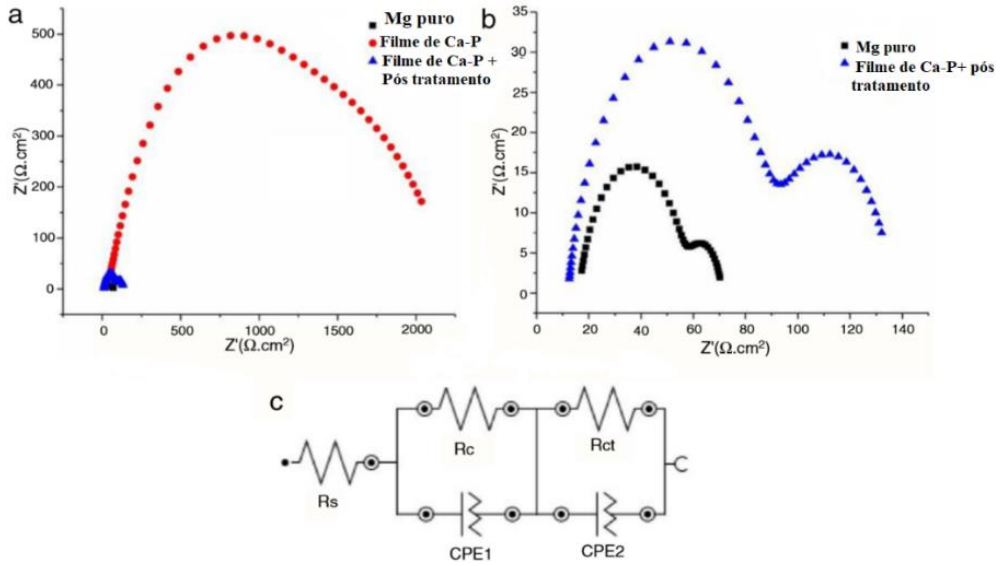

Figura 9- Diagramas de Nyquist para o (a) Mg puro, Mg/DCPD e Mg/DCPD/HAp. (b) Mg puro e Mg/DCPD/HAp. (c) Circuito elétrico equivalente simulado para as amostras examinadas. Adaptado de (ZALUDIN *et al.*, 2018)

WANG *et al.* (2009) depositaram revestimento de DCPD em substrato de Mg e avaliaram seu desempenho frente à corrosão em SBF. Para isso, foi considerada a perda de massa registrada em função do tempo de imersão. Notou-se que as perdas de massas em amostras recobertas com DCPD foram inferiores às observadas para amostras sem revestimento. Ainda, o aumento de pH do SBF foi menor no grupo revestido do que no grupo sem revestimento. Os autores observaram que nos primeiros 3 dias de imersão em SBF, o revestimento DCPD ainda se

mostrava intacto e cobria totalmente o substrato. A dissolução do DCPD tornou-se visível no 5º dia de imersão, mas essa camada se manteve sobre o Mg durante os 21 dias de imersão.

LI *et al.* (2012) depositaram revestimento de DCPD sobre a superfície da liga ZK60 (composição mássica (%): 94 Mg – 4,8-6,2 Zn – ≥ 0,45 Zr). A citotoxicidade dos materiais obtidos foi avaliada através de ensaios de MTT, utilizando células L-929 de fibroblastos de camundongos. Extratos foram preparados conforme sugerido na norma ISO 10993-5 e, em seguida, diluídos a 25%, 50%, 75% e 100%. Por fim, as soluções obtidas foram incubadas por 72 h a 37 °C em atmosfera rica em CO_2. A viabilidade celular foi avaliada através de ensaio MTT (Figura 10). Os materiais ensaiados foram: ZK60 puro, ZK60/DCPD e ZK60/DCPD tratado termicamente a 300 ºC por 3 h. Notou-se que as amostras de ZK60 recobertas não exibiram modificação após um dia de cultura nas diferentes concentrações de extratos. Após três dias de cultura celular (Figura10b), observou-se uma redução da densidade óptica para todas as amostras em todas as concentrações do extrato. Esse efeito foi mais pronunciado para o extrato de 100%. Nota-se que os materiais revestidos com DCPD e, especialmente aqueles tratados termicamente, apresentaram uma maior viabilidade celular após três dias de cultura. Testes *in vitro* conduzidos em amostras de Mg e suas ligas sugeriram que quanto menor a resistência à corrosão do material, maior o valor de pH do meio e maior é a sua citotoxicidade. Dessa maneira, era esperado que com a redução da taxa de corrosão da liga após seu revestimento com DCPD, menor seria sua citotoxicidade (LI *et al.*, 2012).

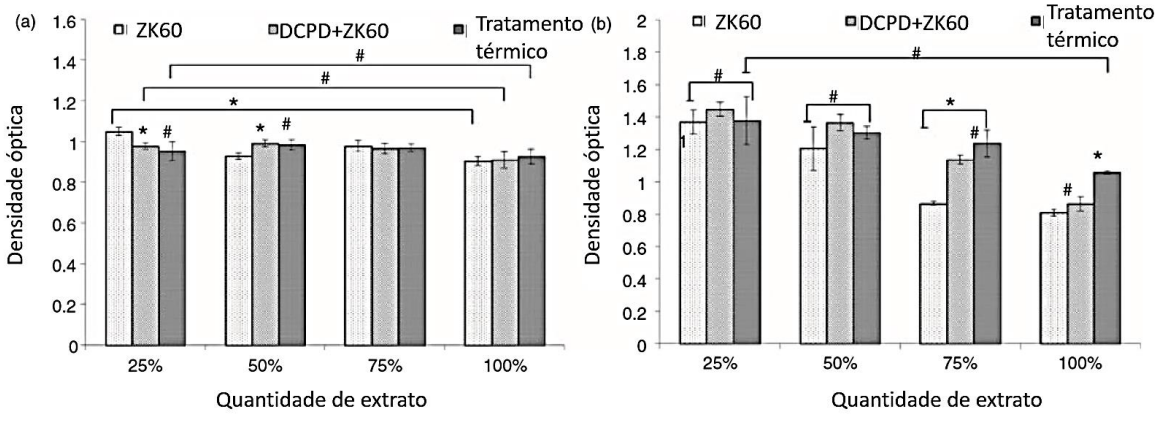

Figura 10 – Viabilidade de células L-929 expressa pela densidade óptica após (a) 1 dia e (b) 3 dias de ensaio sobre liga ZK60 não revestida, liga ZK60 revestida com DCPD e liga ZK60 revestida com DCPD e tratada termicamente. Adaptado de (LI et al., 2012).

Materiais cerâmicos como BG e vitrocerâmicas têm sido amplamente utilizados em aplicações biomédicas devido às suas grandes bioatividades. O BG, em particular, possui grande

capacidade de formar ligações interfaciais com tecidos vivos, contribuindo para restauração de órgãos e sistemas defeituosos. Ademais, possui capacidade de se degradar no corpo humano, sendo gradativamente substituído pelo tecido regenerado (SOLA *et al.*, 2011). Dessa forma, a aplicação do BG como material de revestimento sobre o Mg e suas ligas não apenas combina sua bioatividade com as boas propriedades mecânicas dos materiais metálicos, mas também melhora a estabilidade química do substrato (LIU e MIAO, 2004).

ZHANG *et al.* (2014) recobriram substratos de Mg com CaP e filmes compósitos BG/CaP. Na primeira etapa do processo de fabricação, foi obtida camada de CaP por conversão química. Em um segundo estágio, BG particulado foi obtido por meio de rota sol-gel. Na terceira etapa o BG produzido foi adicionado a banho fosfático para produção de revestimento compósito BG-CaP. Verificou-se que o material revestido exibiu formação de camada de HAp mais efetiva que o Mg puro, sobretudo após 30 dias de imersão em SBF (Figura 11). Notou-se que a densidade da corrente de corrosão obtida para o Mg revestido com BG/CaP foi mais baixa do que a do Mg não revestido ou recoberto com CaP.

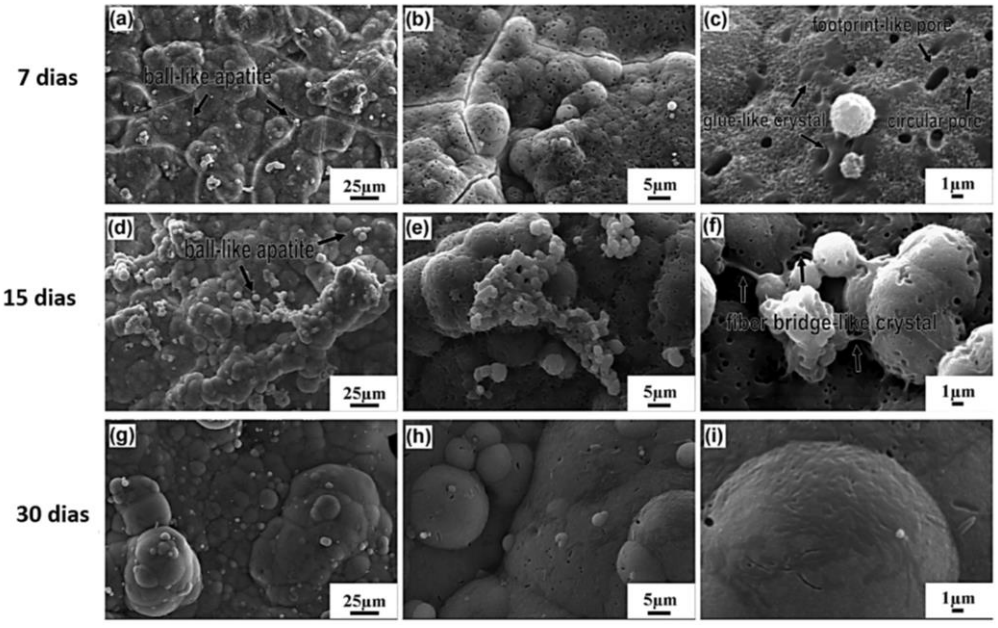

Figura 11 – Morfologias da superfície do Mg revestido com BG/CaP imerso em solução de SBF por 7 dias (a − c), 15 dias (d − f) e 30 dias (g − i). Adaptado de (ZHANG *et al.*, 2014).

Revestimentos híbridos orgânicos-inorgânicos também têm sido empregados em aplicações biomédicas. Segundo (SAVELEVA *et al.*, 2019), esses materiais são candidatos promissores, pois são hidrofílicos, são capazes de acumular íons na interface superfície/meio fisiológico e podem proteger o substrato contra íons agressivos responsáveis pela sua corrosão. Biopolímeros como poliésteres alifáticos sintéticos e polímeros naturais também podem ser

empregados para revestir materiais metálicos devido às suas múltiplas funções. São materiais versáteis, com biocompatibilidade e biodegradabilidade adequadas(AGARWAL *et al.*, 2016; SONG *et al.*, 2020). Nesse trabalho, optou-se por utilizar o álcool polivinílico (PVA) para produzir revestimentos híbridos biocompatíveis e anticorrosivos. O PVA é um polímero sintético hidrofílico e biodegradável, bastante utilizado em engenharia de tecidos. Ademais, possui boa estabilidade química, térmica e mecânica (IBRAHIM *et al.*, 2017; TEIXEIRA *et al.*, 2019).

Na literatura existem vários trabalhos relacionados à produção de compósitos a partir da combinação de PVA e BG. Entretanto, a maior parte deles é focada na produção de *scaffolds* (GAO *et al.*, 2012; MANSUR *et al.*, 2012; TEIXEIRA *et al.*, 2019). DILSHAD *et al.* (2019) recobriram uma liga Mg/Ca com filme compósito PVA/fosfato de magnésio. Os autores observaram que as amostras recobertas exibiram maior fração de Ca e P sobre suas superfícies. Ainda, essas amostras apresentaram grande bioatividade após 72 h de imersão em SBF. BAKHSHESHI-RAD *et al.* (2015) avaliaram uma liga Mg-Ca-Zn revestida com recobrimento híbrido composto por policaprolactona (PLC), HAp e ortofosfato de cálcio. Por meio de ensaio de EIS em SBF, foi observado que a presença do filme híbrido aumentou a resistência à corrosão da liga examinada (Figura 12).

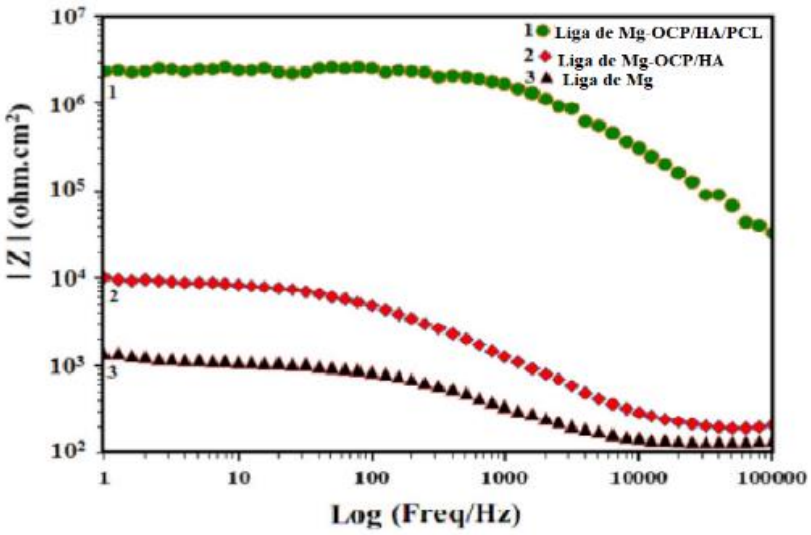

Figura 12 - Diagrama de Bode para liga Mg-Ca-Zn em SBF.
Adaptado de (BAKHSHESHI-RAD *et al.*, 2015).

- MÉTODOS DE DEPOSIÇÃO DE REVESTIMENTOS

Recobrimentos orgânicos e inorgânicos podem ser produzidos por meio de suspensões coloidais, a partir de métodos denominados processos de revestimentos a úmido (*wet coating*). Dentre esses métodos, vale citar pintura, revestimento rotativo (*spin-coating*), eletrodeposição, pulverização e imersão (*dip-coating*) (Figura 13). A técnica de *dip-coating* consiste, de forma geral, na imersão de um substrato em uma solução contendo o material a ser depositado, em sua retirada do meio líquido a uma velocidade constante, na secagem e no tratamento térmico do material preparado. Mediante monitoramento de variáveis como a viscosidade do meio líquido e a velocidade de retirada do substrato, é possível controlar a espessura do revestimento produzido (HORNBERGER *et al.*, 2012). Trata-se de técnica versátil, amplamente empregada em processos industriais em uma variedade de substratos (metálicos, cerâmicos e poliméricos) com diferentes geometrias (TANG e YAN, 2017).

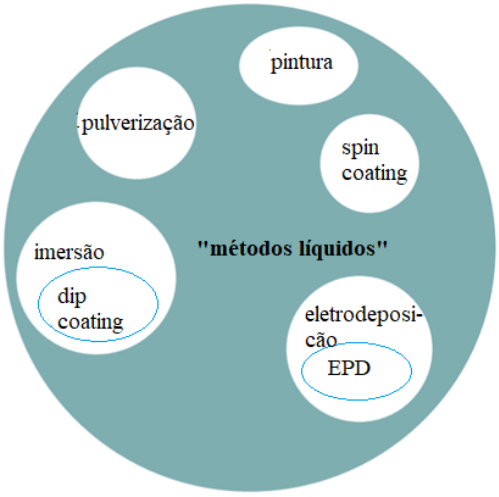

Figura 13 – Visão geral dos processos de revestimento a úmidos empregados na deposição de filmes inorgânicos e orgânicos. Adaptado de (HORNBERGER *et al.*, 2012).

Outra maneira efetiva de realizar a modificação superficial do Mg de forma prática e barata é através de processo denominado conversão química. Esse método consiste em manter o substrato de Mg em uma solução contendo os compostos que se deseja depositar sobre o material. No caso do DCPD, a solução utilizada é geralmente constituída por nitrato de cálcio, óxido de cálcio e ácido fosfórico. Durante a imersão do Mg nessa mistura, há a formação de DCPD sobre sua superfície. O mecanismo envolvido nesse processo é descrito em detalhes no capítulo 4. Trata-se de técnica simples que dá origem a recobrimentos aderentes, uniformes e bastante adequados para se revestir substratos com geometrias complexas (SU *et al.*, 2016).

3.4. REFERÊNCIAS

AGARWAL, S. *et al.* Biodegradable Magnesium Alloys for Orthopaedic Applications: A Review on Corrosion, Biocompatibility and Surface Modification. Materials Science & Engineering 68 p.948-963, 2016. DOI**:** i: 10.1016/j.msec.2016.06.02

ALVAREZ-LOPEZ, M. *et al.* Corrosion behaviour of AZ31 magnesium alloy with different grain sizes in simulated biological fluids. Acta Biomaterialia, 6 p.1763–1771, 2010. DOI**:**

BAKHSHESHI-RAD, H. R. *et al.* Synthesis and corrosion behavior of a hybrid bioceramic-biopolymer coating on biodegradable Mg alloy for orthopaedic implants. Journal of Alloys and Compounds, 648 p.1067-1071, 2015. DOI**:** doi.org/10.1016/j.jallcom.2015.07.075

BIRBILIS, N. *et al.* Grain character influences on corrosion of ECAPed pure magnesium. Corrosion Engineering, Science and Technology, 45 3 p. 224-230, 2013. DOI**:**

BRAGA, J. D. O. *et al.* Fabrication and characterization of dicalcium phosphate coatings deposited on magnesium substrates by a chemical conversion route. Surface & Coatings Technology, 385 p.1-11, 2020. DOI**:** doi.org/10.1016/j.surfcoat.2020.125505

CASTRO , M. M. *et al.* Magnesium-Based Bioactive Composites Processed at Room Temperature. Materials, 16 p.1-16, 2019. DOI**:** doi.org/10.3390/ma12162609

CASTRO, M. M. *et al.* Magnesium-Based Bioactive Composites Processed at Room Temperature. Materials, 12 16 p.1-17, 2019. DOI**:**

CHENG, Z. *et al.* Biocompatible DCPD Coating Formed on AZ91D Magnesium Alloy by Chemical Deposition and Its Corrosion Behaviors in SBF. Journal of Bionic Engineering, 11 p.610-619, 2014. DOI**:**

DILSHAD , T. T.; RAHIM, S. A.; T, H. Polyvinyl alcohol/magnesium phosphate composite coated Mg–Ca alloy for biodegradable orthopaedic implant applications. Materials Research Express, 6 p.1-11, 2019. DOI**:** doi.org/10.1088/2053-1591/ab4d83

GAO, C. *et al.* Preparation and in vitro characterization of electrospun PVA scaffolds coated with bioactive glass for bone regeneration. JOURNAL OF BIOMEDICAL MATERIALS RESEARCH A, 100A p.1324-1334, 2012. DOI**:** doi.org/10.1002/jbm.a.34072

HORNBERGER, H.; VIRTANEN, S.; BOCCACCINI, A. R. Biomedical coatings on magnesium alloys – A review. Acta Biomaterialia, 8 p.2442-2455, 2012. DOI**:** dx.doi.org/10.1016/j.actbio.2012.04.012

IBRAHIM, M. S.; EL-WASSEFY, N. A.; FARAHAT, D. S. Biocompatibility of dental biomaterials. Biomaterials for Oral and Dental Tissue Engineering, p.117-140, 2017. DOI**:** dx.doi.org/10.1016/B978-0-08-100961-1.00008-6

KALB, H.; RZANY, A.; HENSEL, B. Impact of microgalvanic corrosion on the degradation morphology of WE43 and pure magnesium under exposure to simulated body fluid Corrosion Science, 57 p.122-130, 2012. DOI**:**

LI, K. *et al.* Microstructure, in vitro corrosion and cytotoxicity of Ca-P coatings on ZK60 magnesium alloy prepared by simple chemical conversion and heat treatment. Journal of Biomaterials Applications 28 3 p. 375–384, 2012. DOI:

LI, Z. *et al.* Microstructure, mechanical and degradation properties of equal channel angular pressed pure magnesium for biomedical application. Materials Science and technology, 29 2 p.140-147, 2013. DOI:

LIU, J.; MIAO, X. Sol–gel derived bioglass as a coating material for porous alumina scaffolds. Ceramics International, 30 p.1781-1785, 2004. DOI:

LOPES, D. *et al.* Corrosion Behavior in Hank's Solution of a Magnesium–Hydroxyapatite Composite Processed by High-Pressure Torsion. Advanced engineering materials, 22 p.1-11, 2020. DOI: doi.org/10.1002/adem.202000765

LOPES, D. R. *et al.* Cytotoxicity and Corrosion Behavior of Magnesium and Magnesium Alloys in Hank's Solution after Processing by High-Pressure Torsion. Adv. Eng. Mater., 21 8 p.1-9, 2019. DOI:

MANSUR, H. S. *et al.* 3D-macroporous hybrid scaffolds for tissue engineering: Network design and mathematical modeling of the degradation kinetics. Materials Science and Engineering: C, 32 p.404-415, 2012. DOI: doi.org/10.1016/j.msec.2011.11.012

MIYAMOTO, H. Corrosion of Ultrafine Grained Materials by Severe Plastic Deformation, an Overview Materials Transactions, 57 5 p.559-572, 2016. DOI:

MORDIKE, B. L.; EBERT, T. Magnesium Properties — Applications — Potential. Materials Science & Engineering A, 302 p.37-45, 2001. DOI:

NASSIF, N.; GHAYAD, I. Corrosion protection and surface treatment of magnesium alloys used for orthopedic application. Advanced Engineering Materials, 2013 2 p.1-10, 2013. DOI:

POURBAIX, M. Atlas of Electrochemical Equilibria in Aqueous Solution 2. Houston: National Association of Corrosion Engineers - NACE 1974.

SAHA, P. *et al.* Effects of grain refinement on the biocorrosion and in vitro bioactivity of magnesium. Materials Science & Engineering C, 57 p.294–303 2015. DOI:

SALAHSHOOR, M.; GUO, Y. Biodegradable Orthopedic Magnesium-Calcium (MgCa) Alloys, Processing, and Corrosion Performance Materials, 5 p.135-155, 2012. DOI:

SAVELEVA, M. *et al.* The effect of hybrid coatings based on hydrogel, biopolymer and inorganic components on the corrosion behavior of titanium bone implants†. Journal of Materials Chemistry B, 7 2019. DOI: DOI: 10.1039/c9tb01287g

SHADANBAZ, S.; DIAS, G. J. Calcium phosphate coatings on magnesium alloys for biomedical applications: A review. Acta Biomaterialia, 8 p.20-30, 2012. DOI: doi.org/10.1016/j.actbio.2011.10.016

SHI, P. *et al.* Improvement of corrosion resistance of pure magnesium in hank's solution by microarc oxidation with sol-gel TiO_2 sealing. Journal of Alloys and Compounds, 469 p.286-292, 2009. DOI:

SILVA, C. L. P. *et al.* Effect of severe plastic deformation on the biocompatibility and corrosion rate of pure magnesium. Journal of Materials Science, 52 10 p.5992-6003, 2017. DOI:

SOLA, A. *et al.* Bioactive glass coatings: a review. Surface Engineering, 27 8 p.560-572, 2011. DOI:

SONG, D. *et al.* Corrosion behavior of equal-channel-angular-pressed pure magnesium in NaCl aqueous solution Corrosion Science, 52 p. 481–490, 2010. DOI:

SONG, G.; SONG, S. A Possible Biodegradable Magnesium Implant Material. Advanced Engineering Materials, 9 p.298-302, 2007. DOI:

SONG, J.; WINKELJANN, B.; LIELEG, B. Biopolymer-Based Coatings: Promising Strategies to Improve the Biocompatibility and Functionality of Materials Used in Biomedical Engineering. Advanced materials interfaces, 7 p.1-19, 2020. DOI: 10.1002/admi.202000850

STAIGER, M. P. *et al.* Magnesium and its alloys as orthopedic biomaterials: A review. Biomaterials, 27 9 p.1728 -1734, 2006. DOI:

SU, Y. *et al.* Preparation and corrosion behaviors of calcium phosphate conversion coating in magnesium alloy. Surface & Coatings Technology, 307 p.99–108, 2016. DOI:

TANG, X.; YAN, X. Dip-coating for fibrous materials: mechanism, methods and applications. Journal of Sol-Gel Science and Technology 81 p.378–404, 2017. DOI: 10.1007/s10971-016-4197-7

TEIXEIRA, M. A.; AMORIM, M. T. P.; FELGUEIRAS, H. P. Poly(Vinyl Alcohol)-Based Nanofibrous Electrospun Scaffolds for Tissue Engineering Applications. Polymers, 12 p.1-33, 2019. DOI: 10.3390/polym12010007

WANG, J. *et al.* Biodegradable Magnesium (Mg) Implantation Does Not Impose mRelated Metabolic Disorders in Rats with Chronic Renal Failure. Scientific Reports, 6 p.1-10, 2016. DOI: DOI: 10.1038/srep26341

WANG, Y.; WEI, M.; GAO, J. Improve corrosion resistance of magnesium in simulated body fluid by dicalcium phosphate dihydrate coating. Materials Science and Engineering C, 29 p.1311–1316, 2009. DOI:

WANG, Y. *et al.* Corrosion process of pure magnesium in simulated fluid. Materials Letters, 62 p.2181–2184, 2008. DOI:

WITTE, F. *et al.* Biodegradable magnesium–hydroxyapatite metal matrix composites. Biomaterials, 28 p.2163–2174, 2007. DOI:

ZALUDIN, M. A. F. *et al.* Fabrication of calcium phosphate coating on pure magnesium substrate via simple chemical conversion coating: surface properties and corrosion performance evaluations. Journal of Materials Research and Technology, 452 p.1-7, 2018. DOI:

ZENG, R. *et al.* In vitro degradation of pure Mg in response to glucose. Scientific Reports, 13026 5 p.1-14, 2015. DOI:

ZHANG, X. *et al.* Preparation and Characterizations of Bioglass Ceramic Cement/Ca−P Coating on Pure Magnesium for Biomedical Applications. ACS Appl. Mater. Interfaces 6 p.513−525, 2014. DOI**:**

ZHEN, Z. *et al.* Hemolysis and cytotoxicity mechanisms of biodegradable magnesium and its alloys. Materials Science & engineering C, 46 p.202 -206, 2015. DOI**:**

ZHENG, Y. F.; GU, X. N.; WITTE, F. Biodegradable Metals. Materials Science & Engineering R, 77 p.1-34, 2014. DOI**:**

4. OBTENÇÃO E CARACTERIZAÇÃO DE REVESTIMENTOS À BASE DE DCPD SOBRE SUBSTRATOS DE MAGNÉSIO

Esse trabalho teve como objetivo preparar revestimento de DCPD por meio da imersão de amostras de Mg em banho de fosfatização com pH em torno de 2,9 por diferentes tempos (entre 6 e 48 h). O DCPD possui razão Ca/P igual a 1, apresentando similaridade química com a fase mineral do osso e favorecendo a formação de HAp quando presente em meios fisiológicos. Compostos à base de CaP são uma boa opção para preparação de revestimentos para redução da taxa de corrosão do Mg e aumento da sua bioatividade. Os materiais obtidos foram examinados quanto às suas propriedades estruturais, resistência à corrosão, biocompatibilidade e citotoxicidade. As amostras obtidas após 24 h de imersão em banho fosfático se mostraram livres de trincas, mais compactas e espessas. Essas amostras exibiram a maior resistência à corrosão dentre os materiais examinados nesse trabalho.

Publicado em Surface & Coatings Technology (volume 386, 125505, 2020).
DOI: 10.1016/j.surfcoat.2020.125505

FABRICATION AND CHARACTERIZATION OF DICALCIUM PHOSPHATE COATINGS DEPOSITED ON MAGNESIUM SUBSTRATES BY A CHEMICAL CONVERSION ROUTE

Jorgimara de O. Braga, Sandhra M. de Carvalho, Lucas M.C. Silva, Renata B. Soares, Vanessa F.C. Lins, Eric M. Mazzer, Manuel Houmard, Roberto B. Figueiredo, Eduardo H.M. Nunes.

ABSTRACT

It is well established that magnesium (Mg) is a promising material for use in biomedical applications. Nonetheless, it exhibits an accelerated corrosion rate when present in physiological media, which may lead to premature degradation of the implant in the body. As a result, it is necessary to slow down the corrosion of Mg in order to ensure that the implant is able to maintain its mechanical integrity during the whole healing period. In this work, dicalcium phosphate dihydrate (DCPD) coatings were formed on hot-rolled Mg substrates by a chemical conversion route aiming to increase the corrosion resistance and biointegration of the latter. The materials prepared herein were examined by scanning electron microscopy, Fourier transform infrared spectroscopy, X-ray diffraction, electrochemical impedance spectroscopy, and *in vitro* assays. The sample obtained after immersing Mg in the phosphating bath for 24 h and with no heat treatment was the one with the highest corrosion resistance. This sample also exhibited the formation of a hydroxyapatite layer on its surface after soaking in Hank's balanced salt solution for times as short as 1 day. Moreover, this specimen showed no toxicity to rat mesenchymal stem cells, suggesting that it is a promising material for biomedical applications.

KEYWORDS: Magnesium; Bioimplant; Chemical conversion; Dicalcium phosphate dihydrate; Corrosion resistance; Structural evaluation.

4.1. INTRODUCTION

It is well established that metallic implants are promising candidates for use in orthopedic applications due to their enhanced mechanical stability when compared to polymers and ceramics [1,2]. Magnesium (Mg), for instance, has attracted great attention over the past years due to properties such as biodegradability, mechanical behavior similar to that displayed by natural bone, and compatibility with the physiological environment [3,4]. Moreover, Mg is non-toxic and it is unlikely that its dissolution causes adverse side effects in the human body [5,6]. Indeed, it has been reported that the presence of Mg is beneficial to bone strength and growth [7]. Nonetheless, Mg exhibits accelerated corrosion when present in physiological media [8], which may lead to premature degradation of the implant in the body. As a consequence, it is necessary to slow down the corrosion of Mg in order to ensure that the implant is able to maintain its mechanical integrity during the whole healing period. When Mg is soaked in physiological media, the contact between the fresh surface and electrolyte-containing solution causes the corrosion of Mg at high rates. This process involves both the release of hydrogen and alkalinization of the environment [9]. The mechanism of Mg biodegradation strongly depends on the medium in which it is immersed; each physiological solution will induce a different biocorrosion process. As a result, different corrosion products can be generated. For instance, MgO, $Mg(OH)_2$, and $MgCO_3$ are the main degradation products observed when Mg is exposed to Hank's balanced salt solution (HBSS), Kokubo's simulated body fluid (SBF), and Dulbecco's modified eagle medium (DMEM), respectively. However, despite the several works carried out in recent years focused on understanding the biocorrosion of Mg and its alloys, it is a consensus among researchers that the mechanisms involved in this process are still far from a complete understanding and much effort must be made to determine them [9,10].

Several strategies have been used to control the biodegradation rate of Mg, including alloying and surface modification [11–13]. Among these approaches, the deposition of coatings on Mg is a promising method. Calcium phosphate (CaP) coatings have been widely investigated because they are non-toxic and biocompatible, besides providing corrosion protection to Mg [14,15]. Su *et al.* [16] studied the deposition of CaP coatings on an AZ60 magnesium alloy by a chemical conversion method. The authors reported that the temperature and pH of the phosphating bath show a great effect on both the structure and corrosion behavior of the prepared coatings. Tan *et al.* [17] coated a biodegradable AZ31 alloy with CaP. They observed that the corrosion potential of the CaP coated alloy increased significantly and that human osteoblast-like cells showed good adherence, proliferation, and differentiation on the surface of

the coated alloy. Zaludin *et al.* [18] coated Mg substrates by combining a phosphating method with an alkaline treatment. They noticed that the phosphating approach led to the formation of a dicalcium phosphate dihydrate (DCPD, $CaHPO_4.2H_2O$) coating, whereas the alkaline treatment converted it into hydroxyapatite (HAp, $Ca_{10}(PO_4)_6(OH)_2$). It was also reported that both treatments improved the corrosion resistance of Mg. Li *et al.* [19] investigated the corrosion resistance of a ZK60 alloy coated with DCPD. The authors heat-treated coated samples in air at 300 °C for 3 h. They reported that the annealed samples displayed higher corrosion resistance than the as-prepared ones, which arises from the increase in density exhibited by the DCPD coatings after the heat treatment step. Nonetheless, as far as we know, there is no study in the literature that simultaneously addresses the structural properties, corrosion behavior, biocompatibility, and cytotoxicity of DCPD coatings deposited by chemical conversion on Mg substrates, as performed herein. Thus, this work brings new insights concerning the use of DCPD to slow down the biocorrosion of Mg.

In this work, DCPD coatings were deposited on Mg substrates by a chemical conversion method. It has been reported that this approach is a simple procedure to prepare uniform and well-adhered CaP coatings [16]. Hot-rolled Mg substrates were initially immersed in a phosphating bath for times ranging from 6 to 48 h. Next, they were heat-treated in air at 100°C for 6 h and examined by scanning electron microscopy (SEM), atomic force microscopy (AFM), Fourier transform infrared spectroscopy (FTIR), and X-ray diffraction (XRD). The corrosion behavior of the prepared samples in HBSS was evaluated by electrochemical impedance spectroscopy (EIS). The samples cytotoxicity was also examined by LIVE/DEAD and MTT (3-(4,5-dimethylthiazol-2-yl)-2,5-diphenyltetrazolium bromide) assays. The *in vitro* bioactivity was evaluated after soaking the prepared samples in HBSS for up to 21 days.

4.2. MATERIALS AND METHODS

4.2.1. SAMPLES PREPARATION

Commercial grade Mg (99.7% purity) was provided as ingots by RIMA (Bocaiúva-MG). Mg plates were obtained after multi-pass hot rolling (4 passes) at 300 °C in air. Substrates with dimensions of 20 × 20 × 1 mm^3 were then cut from the hot-rolled plates. The substrates were subsequently ground with SiC papers of different grain sizes (up to #4000 grit), cleaned with deionized Milli-Q water, and degreased by sonication in ethanol at room temperature for 15 min. The as-prepared substrates were then immersed in a bath of calcium nitrate tetrahydrate

($Ca(NO_3)_2.4H_2O$, 12 $g.L^{-1}$), calcium oxide (CaO, 1.2 $g.L^{-1}$) and phosphoric acid (H_3PO_4, 85 vol% in water, 8 $mL.L^{-1}$). The immersion time ranged from 6 to 48 h. The temperature and pH of the phosphating bath were kept constant at room temperature and 2.8 which, according to Su *et al.* [16], give rise to CaP coatings able to provide corrosion protection to Mg. After the immersion step, the coated samples were rinsed with deionized water. Some samples were subsequently heat-treated in air at 100 °C for 6 h to investigate the effect of this step on the behavior of the prepared coatings. The as-prepared samples were designated as CaP-Xh, where X represents the immersion time (h) in the phosphating bath. The heat-treated specimens were labeled as CaP-Xh-HT.

4.2.2. STRUCTURAL CHARACTERIZATION

XRD was carried out on a Philips-Panalytical PW 1710 system operating at 40 kV and 30 mA. XRD patterns were taken at a step size of 0.02° (2θ) and using CuKα as the radiation source (λ = 1.54 Å). The crystalline phases observed in obtained patterns were identified according to the JCPDS database (Joint Committee on Powder Diffraction Standards). SEM was conducted on Jeol JSM-6360LV and Fei Quanta FEG 3D microscopes at accelerating voltages ranging from 5 to 20 kV. The examined samples were previously sputter-coated with a 10 nm-thick gold film. Energy dispersive spectroscopy (EDS) was carried out with Thermo Noran systems available in the SEM microscopes. AFM was conducted on an Asylum Research MFP-3D microscope operating in the tapping mode. Silicon cantilevers with a spring constant of 26 $N.m^{-1}$ and resonance frequency of 300 kHz were employed in these tests. FTIR was conducted on a Bruker Alpha spectrometer using an attenuated total reflectance (ATR) accessory and a diamond crystal as the reflective element. The FTIR spectra were taken at a resolution of 4 cm^{-1} and 128 scans. EIS was conducted at 25 °C with an Autolab PGSTAT 100N potentiostat. Three electrodes were used in these tests, namely saturated calomel as the reference electrode, platinum as the counter-electrode, and the Mg sample as the working electrode. The surface area evaluated in these tests was kept constant at 1.2 cm^2. Samples were kept soaked in HBSS for 1 h prior EIS tests for stabilization purposes. EIS was performed at the corrosion potential using an amplitude of 10 mV within a frequency range of 10 kHz -10 mHz. The thicknesses of the prepared coatings were measured on a PosiTector 6000 FNS gauge. It was considered the average of 10 different test points distributed on the surface of the examined samples.

4.2.3. IN VITRO ASSAYS

Sample's cytotoxicity was evaluated using rat mesenchymal stem cells (MSCs) by direct contact through MTT and LIVE/DEAD assays. Female Wistar rats of 6-8 weeks old and 220-250 g in weight were used in this study. All procedures, care, and treatment of these animals were conducted as recommended in the Guide for the Care and Use of Laboratory Animals of the US National Institutes of Health [20]. The following antibodies obtained from BD Biosciences (San Jose, CA, USA) were used: anti-CD45 (clone 69 mouse), anti-CD54 (clone 1A29 mouse), anti-CD73 (clone 5 F / B9 mouse), and anti-CD90 (clone Ox-7 mouse). MSCs were initially cultured at 37 °C in a 5 %CO_2 environment for 72 h in a DMEM supplemented with fetal bovine serum (FBS – 10 vol%), streptomycin sulfate (10 mg.mL^{-1}), penicillin G sodium (10 units.mL^{-1}), and amphotericin-b (0.025 mg.mL^{-1}). All these reactants were supplied by Gibco BRL (NY, USA). The cultured cells were used for experiments in passage 3.

The square samples (3.5 × 3.5 mm^2) used in MTT assays were prepared as suggested in the ISO 10993-5:2009 standard [21]. These materials were initially exposed to ultraviolet radiation for 60 min on each side before culture initiation. Cell populations were initially synchronized in a serum-free medium for 24 h. Next, 3×10^5 cells/well were seeded on samples grown in 24-well plates. Controls were used with the cells and DMEM containing FBS. It was used as the positive control 1 vol% Triton X-100 in phosphate-buffered saline and as the negative control chips of sterile polypropylene Eppendorf tubes (1 mg.mL^{-1}). After 72 hours, the medium was aspirated and replaced by 210 µL culture medium with serum. Cells were incubated at 37 °C and 5 % CO_2 after adding 170 µL of MTT (5 mg.mL^{-1}). After 4 h, 80 µL of a solution of isopropyl alcohol and hydrochloric acid (4 vol%) was added to each well. Next, 100 µL was removed from each well and transferred to a 96-well plate to assess the absorbance in a Bio-Rad I Mark Microplate Reader at a wavelength of 595 nm. The cell viability (Cell%) was calculated by considering the absorbance measured for the samples ($Abs_{samples}$) and control groups ($Abs_{control}$) as described in Eq. (4.1):

$$\text{Cell}(\%)=\left(\frac{\text{Abs}_{\text{samples}}}{\text{Abs}_{\text{control}}}\right)\times100\ . \tag{4.1}$$

For LIVE/DEAD assays, MSCs were initially synchronized in a serum-free medium for 24 h. Next, 3×10^5 cells/well were seeded on the samples grown in 24-well plates. After 72 h the medium was aspirated, the cells were washed 3 times with phosphate-buffered saline and then treated for 30 min with a LIVE/DEAD viability/cytotoxicity kit following the supplier specifications (Life Technologies of Brazil, São Paulo). Images were obtained with a Leica

DMIL LED microscope and fluorescence was taken for calcein (530.0 ± 12.5 nm) and propidium iodide (645 ± 20 nm). The data obtained in MTT and LIVE/DEAD assays were examined with the Prism software (GraphPad Software, San Diego, CA, USA). The following parameters were considered in these statistical analyses: $P < 0.05$, $N = 6$, one-way ANOVA, Bonferroni test. The adhesion and spreading of MSCs on the examined samples were evaluated by SEM following the procedure described elsewhere [22]. Briefly, samples were initially fixed with 2% glutaraldehyde for 16 h and dehydrated after washing them with a series of aqueous ethanol solutions (ethanol concentration ranging from 20 to 100 vol%). The materials were subsequently dried in a nitrogen flowing reactor for 4 h and outgassed under vacuum for 12 h. Before the examination, samples were carefully sputter-coated by keeping them at the maximum distance from the gold target and at a low sputtering rate to prevent damages on their surface.

The *in vitro* bioactivity of the coated-samples was evaluated after soaking in HBSS for up to 21 days. HBSS and SBF are probably the most used solutions to mimic the ionic composition of human plasma and evaluate the bioactivity of biomaterials [23]. Although SBF has a stronger buffer capacity to keep pH around 7.4 due to the presence of tris(hydroxymethyl)aminomethane, this compound may both react with Ca^{2+} and inhibit the mineralization process [24]. Therefore, HBSS was selected in this study. The temperature and pH of this solution were kept at 37 °C and 7.4 during the test. The solution pH was checked twice a day and adjusted by slowly adding an aqueous solution of hydrochloric acid (0.1 M) into it. After removing samples from HBSS, they were rinsed with deionized water and air-dried at 100 °C overnight. They were subsequently examined by XRD, FTIR, SEM, and EDS.

4.3. RESULTS AND DISCUSSION

4.3.1. COATED SAMPLES

Fig. 14 displays the XRD patterns collected in this study. The bare substrate showed diffraction lines ascribed to Mg only, which reveals that no contamination or oxidation occurred during the hot rolling step. The coated samples exhibited additional lines associated with DCPD, indicating that a CaP coating was successfully formed on the Mg substrate. It has been reported that during the phosphating process, anodic (Eq. 4.2) and cathodic (Eq. 4.3) reactions may take place at different polarization sites on the Mg surface [16]:

$$Mg_{(s)} \rightarrow Mg^{2+}_{(aq)} + 2e^{-} \quad (4.2)$$

$$2H_2O_{(l)} + 2e^{-} \rightarrow H_{2(g)} + 2OH^{-}_{(aq)} \quad (4.3)$$

It has been also proposed that Mg^{2+} ions may react with OH^{-} species, which gives rise to a partially-protective $Mg(OH)_2$ film [25]:

$$Mg^{2+}_{(aq)} + 2OH^{-}_{(aq)} \rightarrow Mg\ (OH)_{2(s)} \quad (4.4)$$

However, Cl^{-} anions present in HBSS may both displace water molecules and transform $Mg(OH)_2$ into a water-soluble $MgCl_2$ phase [26]:

$$Mg(OH)_{2(s)} + 2Cl^{-}_{(aq)} \rightarrow MgCl_{2(s)} + 2OH^{-}_{(aq)} \quad (4.5)$$

CaO, H_3PO_4, and H_2O may also react in the phosphating bath:

$$CaO_{(s)} + 2H_3PO_{4\ (l)} + H_2O_{(l)} \rightarrow Ca(H_2PO_4)_2.2H_2O_{(s)} \quad (4.6)$$

However, $Ca(H_2PO_4)_2.2H_2O$ is unstable and may dissociate into different products:

$$Ca(H_2PO_4)_2.2H_2O_{(s)} \rightarrow CaPO^{-}_{4\ (aq)} + H_2PO^{-}_{4(aq)} + 2H^{+}_{(aq.)} + 2H_2O_{(l)} \quad (4.7)$$

The complex $CaPO_4^{-}$ can also dissociate in the phosphating bath:

$$CaPO^{-}_{4\ (aq)} \rightarrow Ca^{2+}_{(aq)} + PO^{3-}_{4\ (aq)} \quad (4.8)$$

Similar reactions to Eq. (4.6) to (4.8) have already been suggested for zinc phosphating baths [27,28]. The formation of DCPD may be related to Eq. (4.9) and (4.10) [29]:

$$2H_2PO^{-}_{4(aq)} + 2e^{-} \rightarrow 2HPO^{2-}_{4\ (aq)} + H_{2(g)} \quad (4.9)$$

$$Ca^{2+}_{(aq)} + HPO^{2-}_{4(aq)} + 2H_2O_{(l)} \rightarrow CaHPO_4.2H_2O_{(s)} \quad (4.10)$$

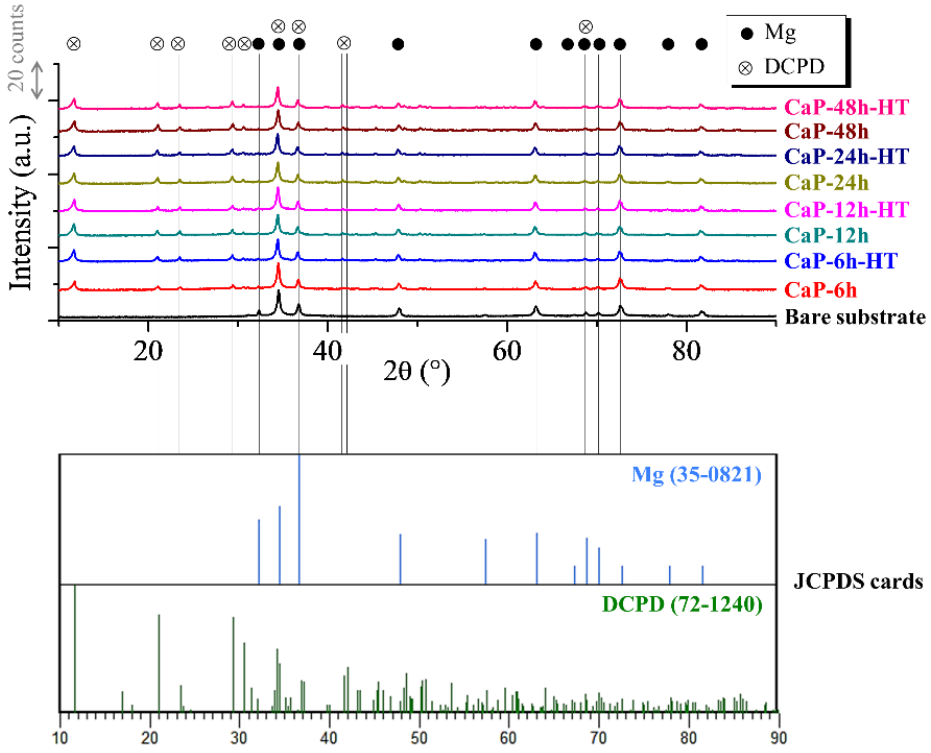

Figure 14- XRD patterns taken in this study. The JCPDS cards used as the reference in these analyses are also shown for comparison purposes.

Fig. 15 exhibits SEM micrographs obtained for samples prepared in this study. Grooves and scratches related to the hot rolling step are observed on the bare substrate. These features are also observed in the AFM images shown in Fig. 16.a. The roughness measured for the bare substrate according to two different parameters, namely Ra and RMS, was 63.7 ± 1.7 and 83.3 ± 0.8 μm, respectively. Ra is the roughness average of a surface measured considering peaks and valleys. RMS, on the other hand, is calculated as the root mean square of this roughness [30]. From Fig. 15, the coated samples displayed flakes with a flower-like shape associated with the DCPD phase [16,18,19]. This finding was also confirmed by EDS: the Ca/P ratio assessed in these analyses was about 1. It appears that the heat treatment of the coated samples at 100 °C for 6 h caused the formation of defects such as cracks and holes on their surface. Besides, a surface peeling was observed for some samples after the heat treatment step.

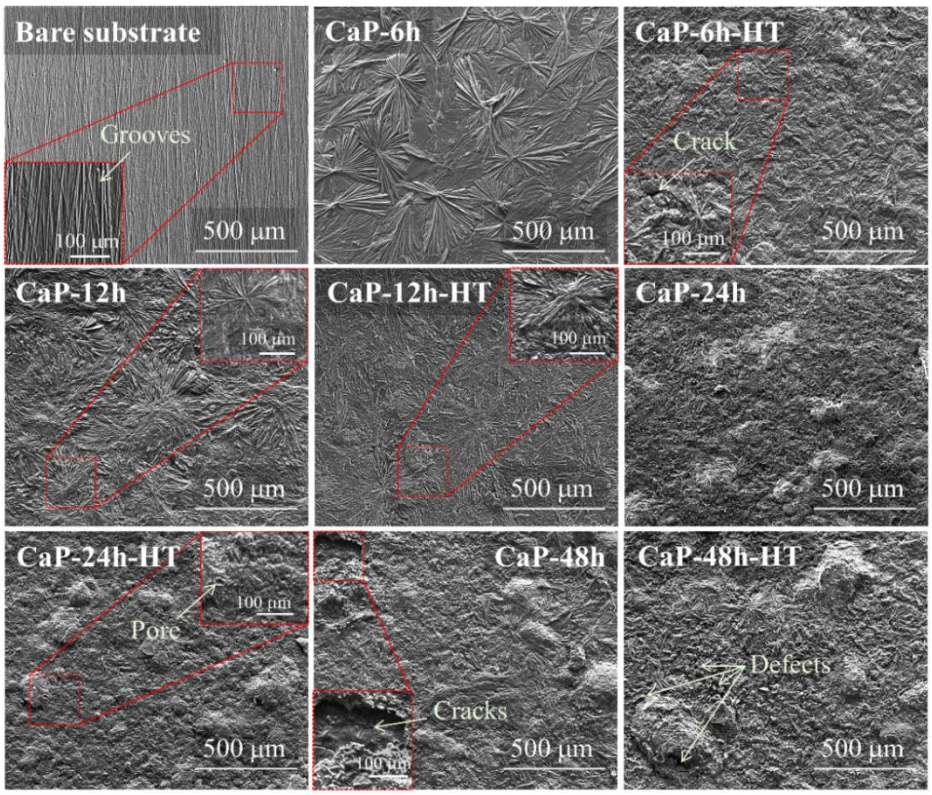

Figure 15-SEM micrographs of samples prepared in this work. The scale bars exhibited in these images correspond to either 100 or 500 µm. SEM images obtained using secondary electrons.

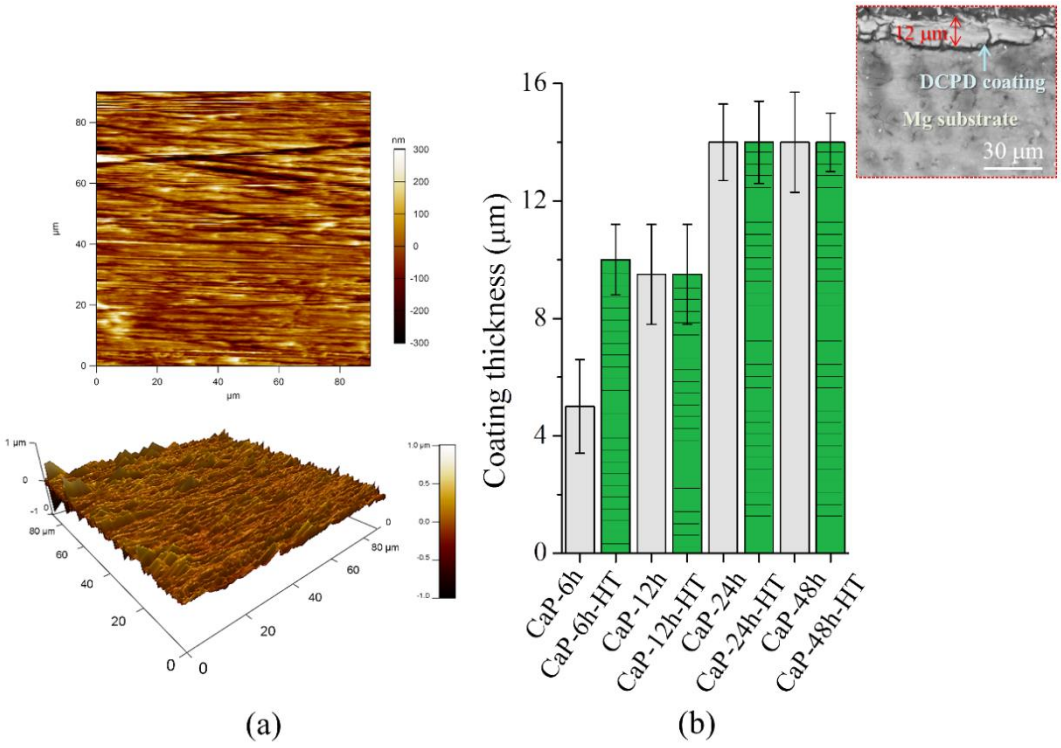

Figure 16 – (a) AFM images collected from the bare Mg substrate. (b) Thickness evaluated for the DCPD coating deposited on different samples. Inset: cross-sectional SEM micrograph of DCPD-coated sample obtained after 24 h of immersion in the phosphating bath.

Fig. 16.b depicts the thickness evaluated for DCPD coatings deposited on different samples. The increase of the soaking time of Mg in the phosphating solution from 6 to 12 and 24 h increased the coating thickness from 5.0 ± 1.6 to 9.5 ± 1.7 and 14.0 ± 1.3 μm, respectively. A further increase of the soaking time to 48 h did not affect the coating thickness since it remained around 14.0 ± 1.7 μm. The formation of DCPD on Mg has been related to the low solubility of the former in the phosphating bath, which favors the occurrence of Eq. (10) [31]. This phase accumulates on Mg during the immersion step, giving rise to a thick coating on it. It appears that the saturation of DCPD on the Mg surface takes place for a 24 h immersion time, justifying why no further increase in thickness was observed when the soaking time was increased from 24 to 48 h. The heat treatment of CaP-6h at 100 °C increased the coating thickness from 5.0 ± 1.6 to 10.0 ± 1.2 μm. However, a similar behavior was not observed for other samples. One observes from Fig. 15 that the heat treatment of CaP-6h caused the disappearance of flower-like structures related to DCPD. It is possible that the heat treatment step caused the transformation of DCPD into other calcium phosphate phases, which contributed to the observed change in thickness. This behavior was not observed for samples prepared after soaking times longer than 6 h probably because the thickness displayed by these materials in the as-prepared condition was much larger than that detected for CaP-6h. Further experiments are needed to fully understand this mechanism. The inset exhibited in Fig. 16 displays a cross-sectional SEM micrograph of a DCPD-coated sample obtained after 24 h of immersion in the phosphating bath. This image was obtained using backscattered electrons, which allowed distinguishing the Mg substrate from the DCPD coating. The thickness measured for this coating was about 12 μm, which is in line with the results shown in Fig. 16.b. The cracks observed between the coating and substrate in this micrograph is due to the preparation stage of the sample used in this examination, which involved both grinding and polishing steps.

Fig. 17 shows Bode plots obtained from EIS. Fig. 17.a exhibits the phase angle as a function of frequency. One observes that the resistive effect of the test solution is more evident at frequencies above 10^3 Hz. Zaludin *et al.* [18] reported that the dielectric properties of DCPD also contribute to this behavior. A capacitive behavior ascribed to the presence of the DCPD coating is observed at frequencies from about 10 to 10^2 Hz. CaP-6h-HT displayed a maximum phase angle of about 20°, revealing that it is the sample with the lowest corrosion resistance. On the other hand, CaP-12h and CaP-24h exhibited a maximum phase angle around 60° and the highest corrosion resistance. It seems that more than one time constant is observed for some samples, which suggests that Cl^- ions could penetrate the DCPD coating towards the metallic substrate and give rise to additional time constants [32]. Fig. 17.b depicts the impedance modulus (|Z|) as a function of frequency. It can be observed that CaP-24 h showed the largest |Z| at frequencies below 10^0 Hz, which reveals that this sample exhibits the highest polarization resistance (R_p). It can also be observed that there is a decrease of |Z| at frequencies around 10^{-3} Hz, which has been ascribed to the relaxation of adsorbed Mg^{2+} ions [33].

Fig. 17.c exhibits |Z| at a constant frequency of 30 mHz. This frequency was chosen because, at this value, the contributions due to either the resistive effect of the test solution or relaxation of adsorbed ions are minimized. One notes that the coating of Mg with DCPD led to materials with larger values of |Z| and consequently higher corrosion resistance. The immersion of Mg in the phosphating bath increased |Z| from 3.5×10^3 (bare substrate) to 8.3×10^3 (CaP-6h), 9.4×10^3 (CaP-12h), and 16.0×10^3 $\Omega.cm^2$ (CaP-24h). However, a further increase of the immersion time from 24 to 48 h decreased |Z| to 8.0×10^3 $\Omega.cm^2$ (CaP-48h). One notices from Fig. 17 that CaP-48h has cracks on its surface, which may favor both the penetration of Cl^- ions in the DCPD coating and corrosion of the Mg substrate. The heat treatment of the coated samples decreased their corrosion resistance since smaller values of |Z| were evaluated for these materials. Defects were noticed in the SEM micrographs of the heat-treated samples (Fig. 17), which may justify the lower corrosion resistance displayed by these specimens. Such defects may favor localized corrosion on the prepared materials, decreasing their corrosion resistance. Nonetheless, it can be observed that |Z| increased with increasing the immersion time for the heat-treated materials, which may be associated with the larger thickness of the DCPD coating (Fig. 17.b).

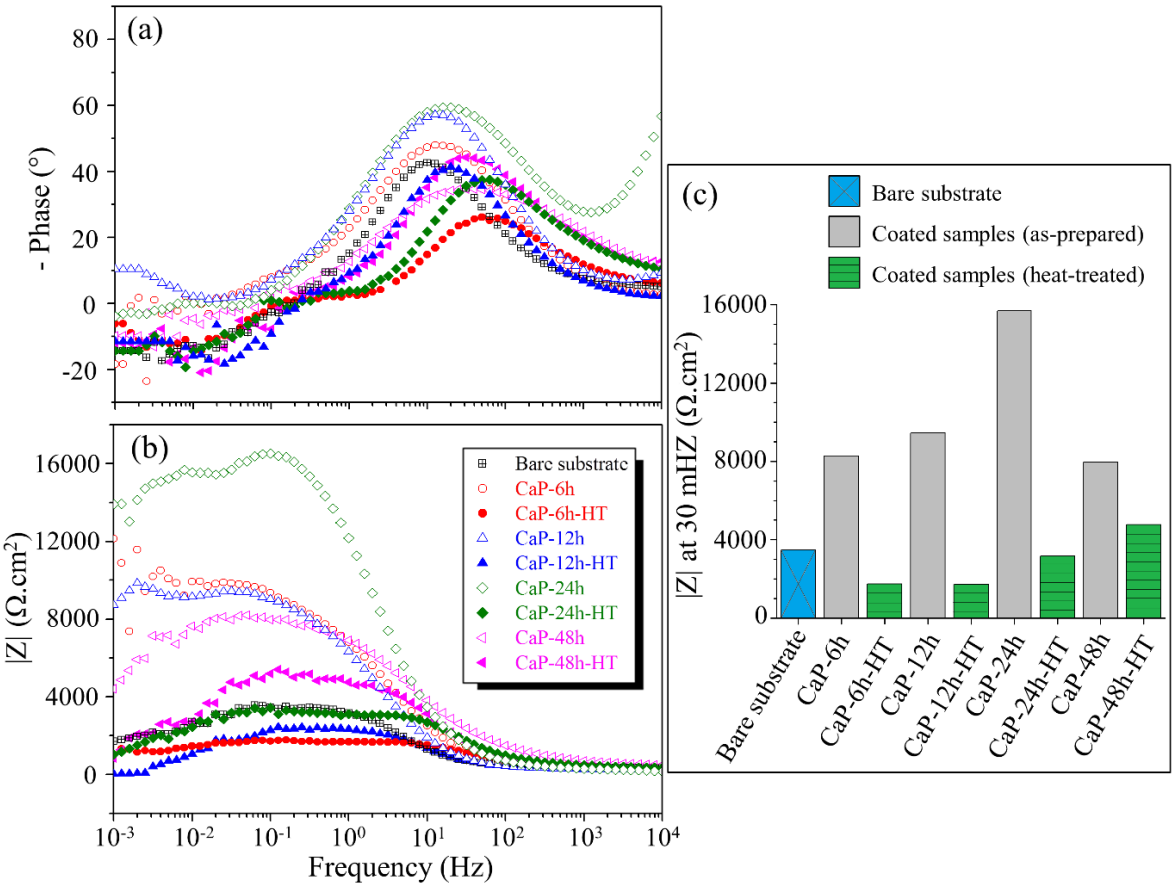

Figure 17 – Bode plots obtained from EIS tests. (a) Phase angle and (b) impedance modulus as a function of frequency. (c) Impedance modulus evaluated at a constant frequency of 30 mHz.

Figure 18 exhibits SEM micrographs and EDS spectra of samples previously used in EIS tests. Cracks are clearly observed in the heat-treated sample, which explains the low corrosion resistance displayed by this material (Fig. 17.c). Flower-like structures ascribed to DCPD are observed in both samples, but the Mg substrate is exposed in the annealed specimen. One observes in the EDS spectra provided in this Figure that a signal associated with an Mg-Kα transition is noted for CaP-24h-HT, confirming that the substrate was in direct contact with HBSS during the EIS tests. This contact causes the formation of an $Mg(OH)_2$ layer on Mg, as expressed in Eq. 4.4. However, this layer is highly soluble, which does not prevent the corrosion of Mg.

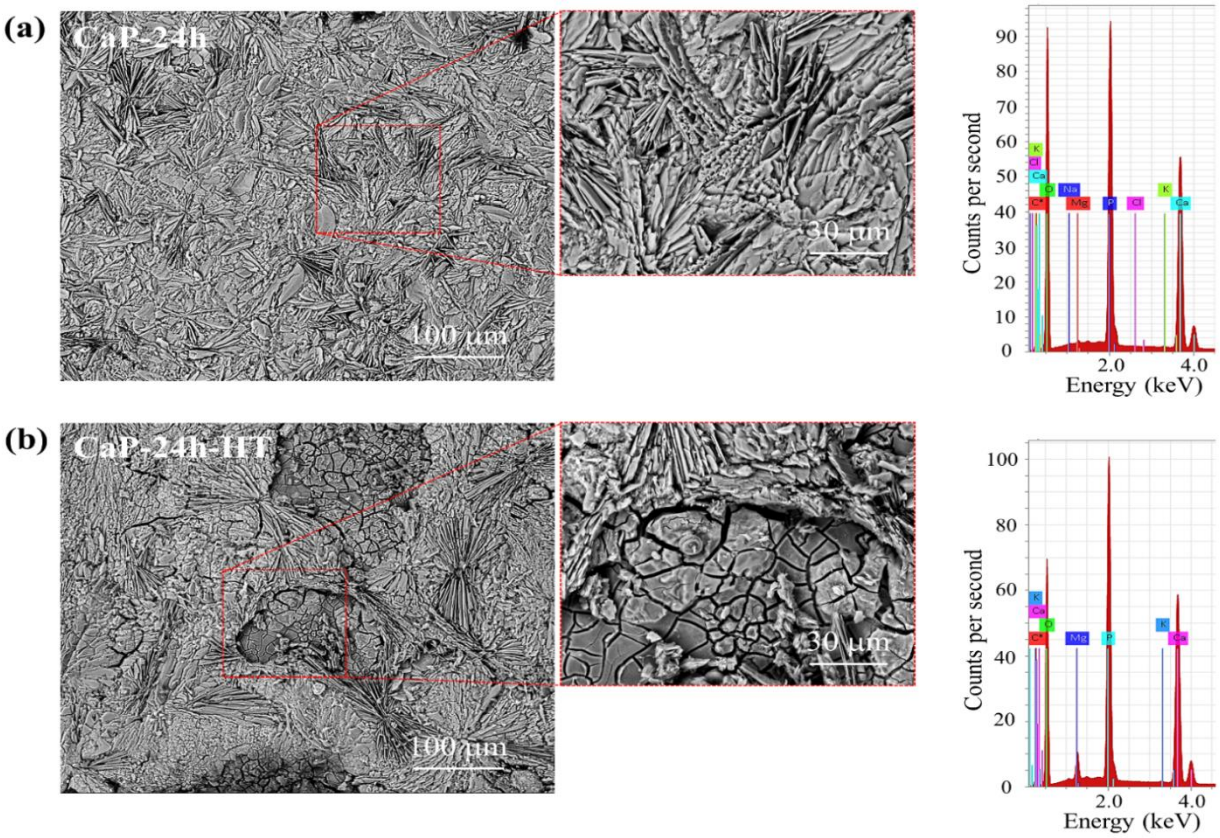

Figure 18 – SEM micrographs and EDS spectra of samples previously used in the corrosion tests (CaP-24h and CaP-24h-HT). SEM images obtained with backscattered electrons.

It appears that the chemical conversion method used in this work gave rise to a protective layer on the Mg substrate. Such a layer inhibited the chemical attack of Mg by Cl^- ions, which could decrease the corrosion rate of the latter in the human body. As discussed before, Mg displays accelerated corrosion in physiological media, which inhibits its application as a biomaterial. It is imperative that implants used as bone grafts should maintain their mechanical integrity during the whole healing period, which may take a long time. Thus, the presence of a DCPD coating could allow the use of Mg as a bone graft, besides improving the affinity of the implant with the human bone. As the sample CaP-24h showed the highest corrosion resistance among the examined materials, it was used for further *in vitro* tests. A bare Mg substrate was also used for comparison purposes.

4.3.2. SOAKING TESTS IN HBSS

Fig. 21 displays the XRD patterns of CaP-24h before and after soaking in HBSS. As discussed before, CaP-24h showed diffraction lines ascribed to Mg and DCPD (Fig. 14). Nonetheless, the major lines of DCPD at $2\theta \approx 12$, 21, and 29° experienced a dramatic decrease after the

immersion in HBSS. Indeed, some diffraction lines associated with DCPD are no longer observed after the soaking step (e.g., $2\theta \approx 31$ and 42°). On the other hand, diffraction lines related to HAp become visible after soaking CaP-24h in HBSS. Moreover, some lines exhibited a significant increase probably due to the overlapping of HAp lines to those of DCPD (e.g., $2\theta \approx 34$, 36, 63, and 72°). It is not possible to clearly distinguish the contribution of HAp due to peak overlap with magnesium. However, the decrease in DCPD suggests the formation of a new phase, HAp, which can be related to Eq. (4.11) and (4.12) [34,35]:

$$10CaHPO_4.2H_2O_{(s)} + 4Na_2HPO_{4(aq.)} \rightarrow Ca_{10}(PO_4)_6(OH)_{2(s)} + 8NaH_2PO_{4(aq.)} \quad (4.11)$$

$$10CaHPO_4.2H_2O_{(s)} + 12OH^-_{(aq.)} \rightarrow Ca_{10}(PO_4)_6(OH)_{2(s)} + 4PO^{3-}_{4(aq.)} + 30H_2O_{(l)} \quad (4.12)$$

It has been reported that DCPD is unstable in media with pH above 6-7, tending to transform into HAp [35]. It is worth recalling that HBSS was kept at pH 7.5 during the soaking tests, which could favor the formation of HAp. The ATR/FTIR spectra of CaP-24h before and after soaking in HBSS are shown in Fig. 20. No normalization procedure was applied to these spectra and the intensity of the absorption bands should not be compared between different samples. The absorption bands at about 400, 520, 575, and 655 cm^{-1} are due to the PO bending mode [36,37]. The presence of structural water in DCPD is evidenced by the bands at 785 and 1210 cm^{-1}, which are ascribed to O–H in-plane bending and H_2O oscillating motion, respectively [38]. The P–O(H) stretching is observed at 870 cm^{-1}, whereas the PO stretching is noticed at 985, 1055, 1120, and 1130 cm^{-1} [36–38]. All these bands are characteristic of DCPD and were observed in the spectrum of the as-prepared sample. However, the samples soaked in HBSS exhibited ATR/FTIR spectra different from that observed for DCPD. One observes that the soaked samples have three broad bands centered at about 550, 1020, and 1410 cm^{-1}, which have been ascribed to HAp [39]. This finding is in line with the behavior observed in XRD tests (Fig. 19).

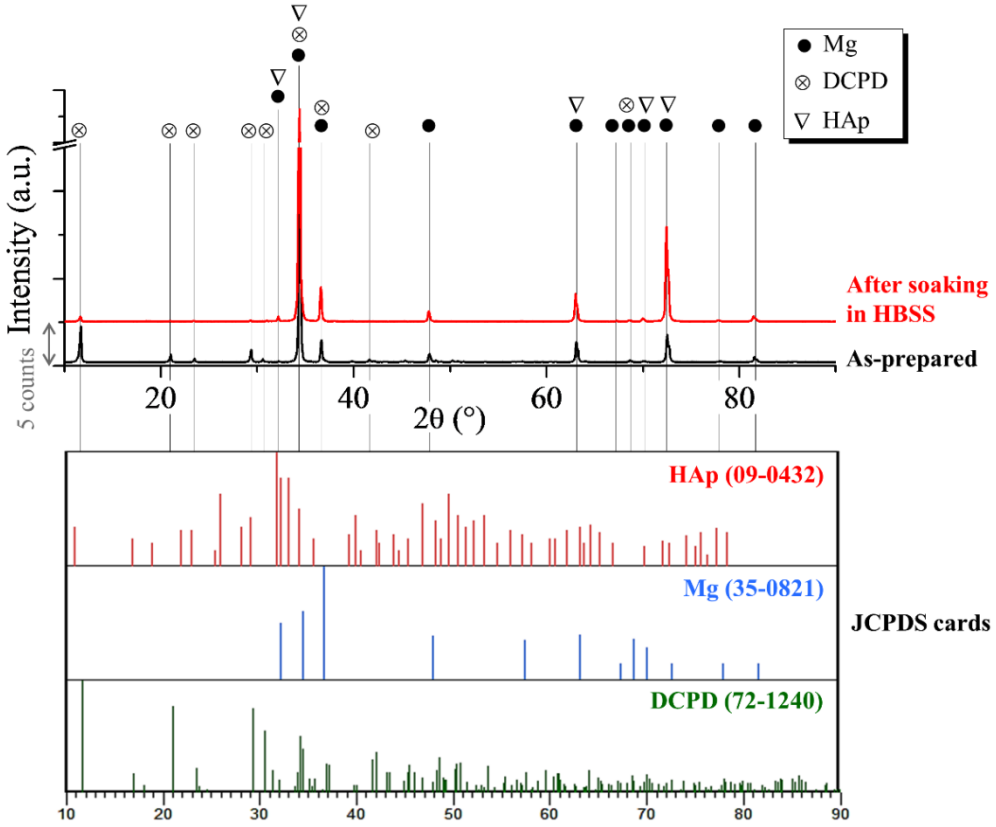

Figure 19 – XRD patterns of CaP-24h before and after soaking in HBSS for 1 day. Similar patterns were obtained for samples soaked for different times and they are not displayed for sake of clarity. The JCPDS cards used as the reference in these analyses are also shown for reference purposes.

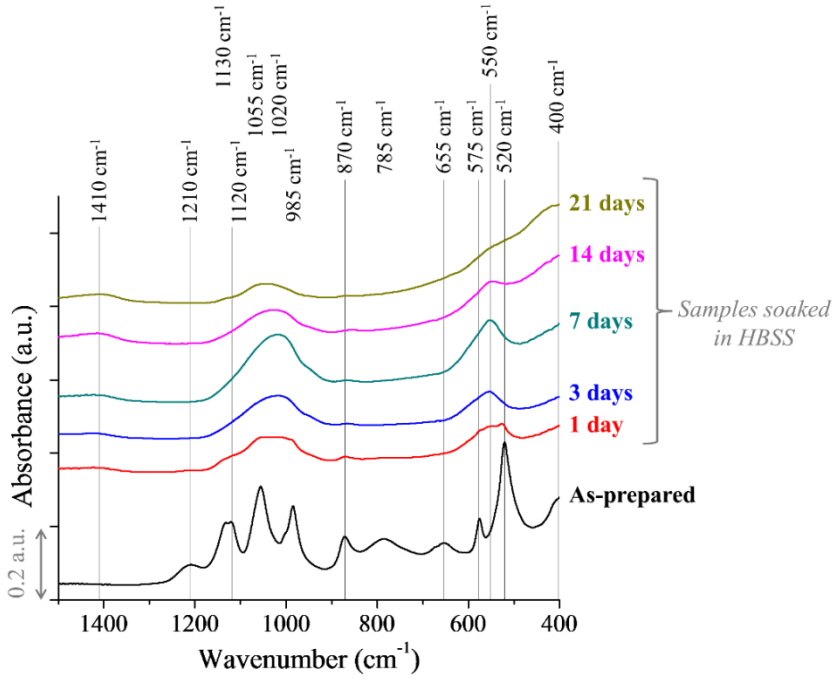

Figure 20 – ATR/FTIR spectra of CaP-24h before and after soaking in HBSS for different times. No normalization was applied to these spectra.

Figs. 21.a and 21.b display SEM micrographs of the bare Mg substrate and CaP-24h after soaking in HBSS for 21 days. The bare substrate experienced a significant degradation over time, showing cracking and peeling after this step. XRD lines ascribed to MgO were observed for this material, which is in agreement with the literature; it has been reported that the soaking of Mg in HBSS gives rise to a MgO layer on it [18]. On the other hand, HAp nodules are observed on the surface of CaP-24h upon soaking in HBSS. Fig. 21.c exhibits an EDS spectrum obtained over a selected area for CaP-24h. The Ca/P ratio in this spectrum is about 1.40, which is slightly smaller than the expected one for HAp (1.65). The nodules observed on CaP-24h have been related to HAp [40–42], which also supports the formation of this phase. The compositional map depicted in Fig. 21.d reveals that Ca and P are nearly homogeneously distributed on CaP-24h, whereas O and Mg show accumulation in specific areas. At this point, it is important to remember that characteristic X-rays may be excited from a depth of several micrometers in an EDS test. Therefore, not only signals derived from the HAp layer were detected in these tests but also from both the DCPD coating and Mg substrate. Thus, it is plausible to observe signals related to Mg in this compositional map, besides detecting a Ca/P ratio between 1.0 (DCPD) and 1.65 (HAp).

XRD, ATR/FTIR, and SEM-EDS examinations (Figs. 19 to 21) revealed that HAp was formed upon soaking CaP-24h in HBSS for times as short as 1 day, which reinforces the biocompatibility of this material. It has been reported that glucose favors the formation of CaP phases on Mg. According to Zeng *et al.* [25], the presence of glucose on the Mg surface induces the uptake of Ca^{2+} ions on it:

$$2RCOOH_{(l)} + Ca^{2+}_{(aq)} \rightarrow (RCOO)_2Ca_{(s)} + H_{2(g)} \quad (4.13)$$

where R is a $CH_2OH(CHOH)_4^-$ radical. The reaction of adsorbed Ca^{2+} ions with HPO_4^{2-} complexes can lead to the formation of HAp:

$$10Ca^{2+}_{(aq)} + 6HPO^{2-}_{4\,(aq)} + 8OH^-_{(aq)} \rightarrow Ca_{10}(PO_4)_6(OH)_{2(s)} + 6H_2O_{(l)} \quad (4.14)$$

Zeng *et al.* [25] also observed that glucose accelerates the corrosion of Mg. However, it is important to use a glucose-containing medium such as HBSS for evaluating the corrosion resistance of Mg because glucose is naturally present in the human blood plasma [43]. Thus, it is expected that glucose plays a key role in both the formation of HAp and the degradation of Mg in practical applications.

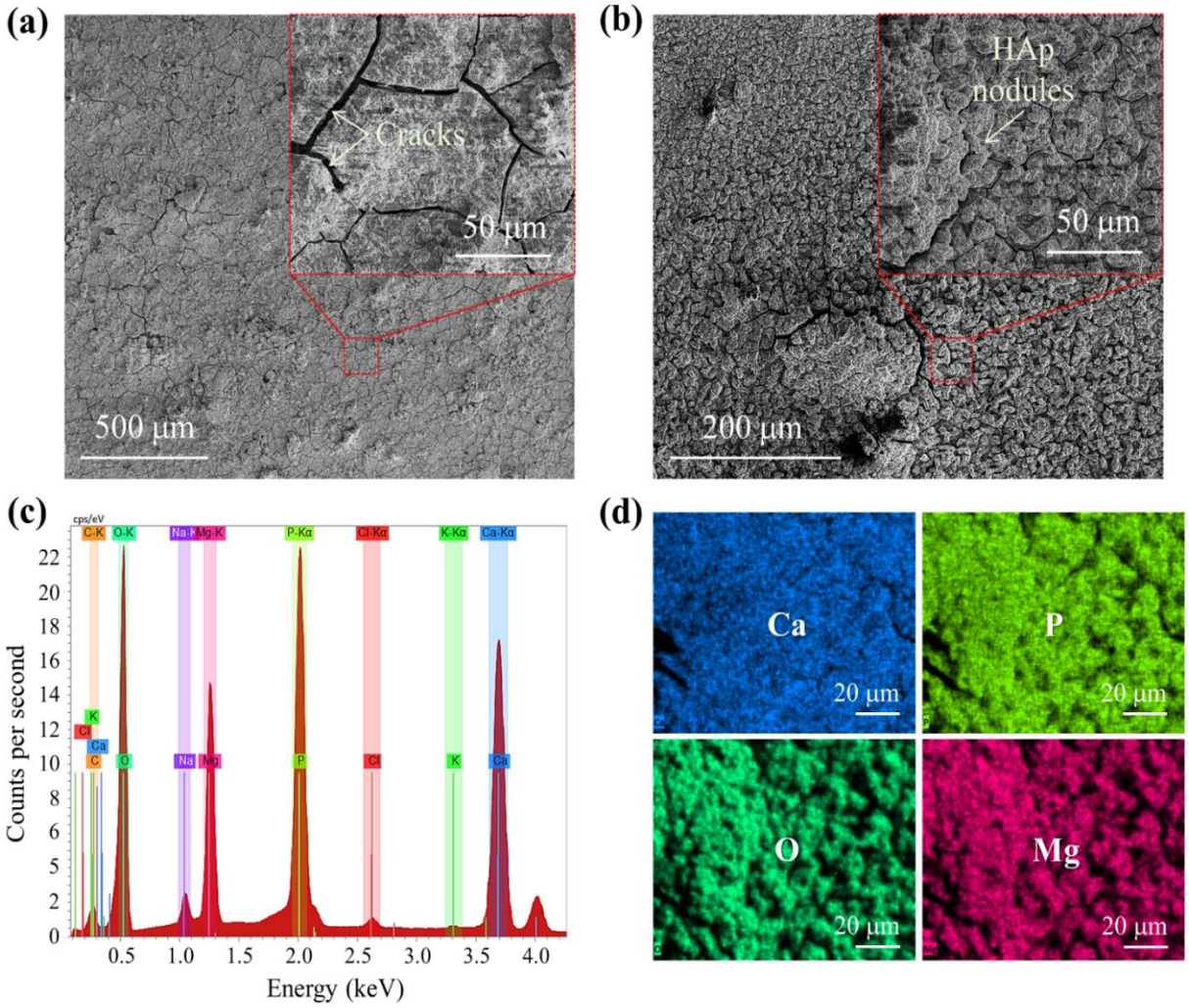

Figure 21 – SEM micrographs for (a) bare Mg substrate and (b) CaP-24h after soaking in HBSS for 21 days. (c) EDS spectrum collected over a selected area and (d) compositional map obtained for CaP-24h after the immersion step. Please refer to the online version of this paper to see Figure 7d in color. SEM micrographs obtained using secondary electrons.

4.3.3. CELL VIABILITY AND ADHESION

Fig. 22.a shows images obtained from LIVE/DEAD assays. This assay is a cell viability test based on the simultaneous evaluation of live and dead cells. Live and dead cells are identified as green and red luminescence, respectively. One observes that a smaller concentration of live cells is observed for the bare Mg substrate when it is compared to the control group. Moreover, a strong red luminescence related to dead cells is noticed for this material. On the other hand, CaP-24h displayed a concentration of live cells like the control group. A slight presence of dead cells is observed for CaP-24h. Fig. 22.b exhibits the results obtained from MTT assays. The dashed horizontal line drawn in this figure represents cell viability of 70%; samples with cell

viabilities below this value are considered cytotoxic. The bare substrate did not reach this cell viability, revealing that this material is cytotoxic to MSCs. This result agrees with the LIVE/DEAD assays where a low concentration of live cells was observed for this material. CaP-24h exhibited, in turn, cell viability above 70%, which suggests that this sample is not cytotoxic, which is also in line with the LIVE/DEAD assays.

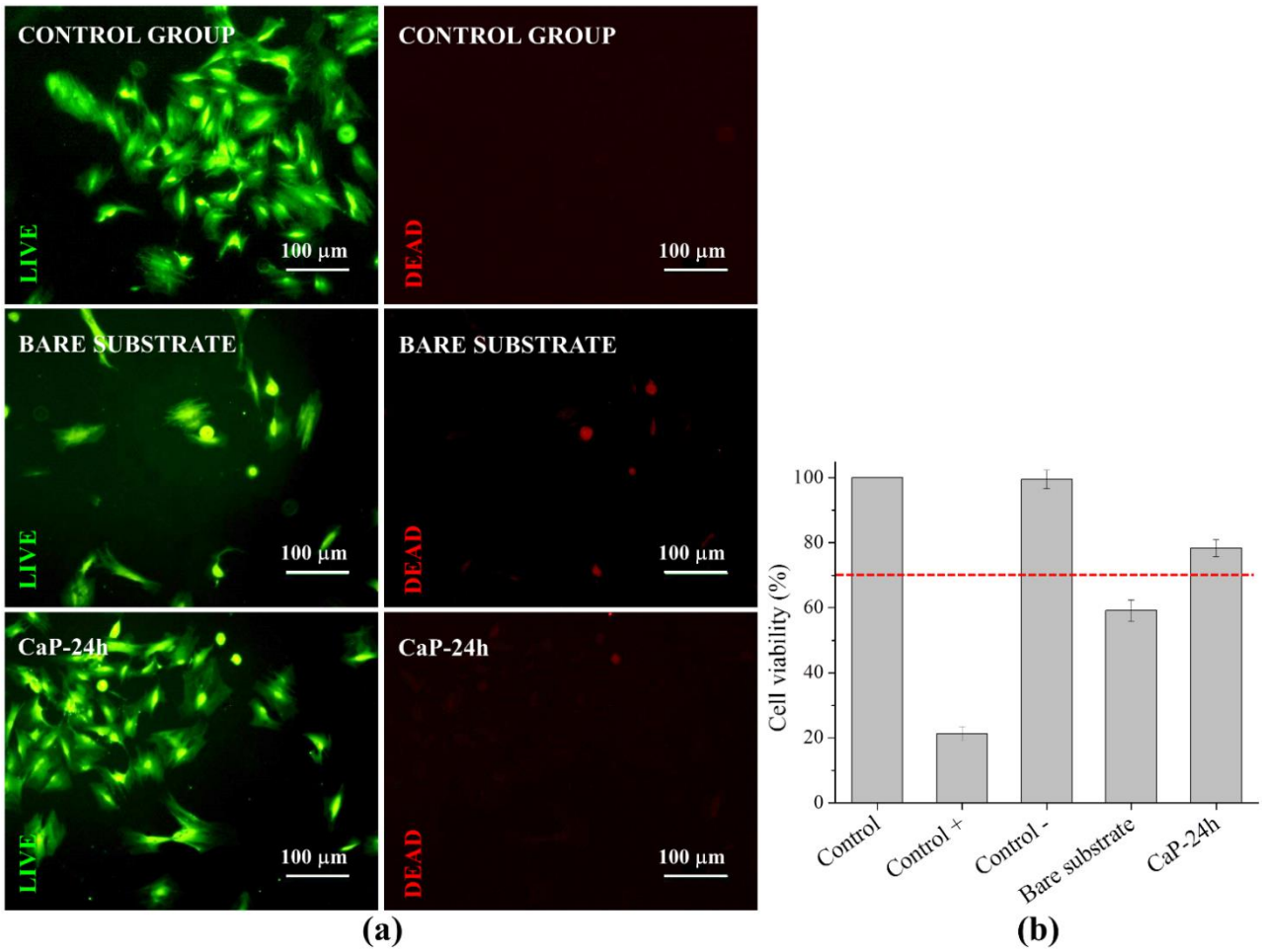

Figure 22 – Results obtained from (a) LIVE/DEAD and (b) MTT assays. The scale bars displayed in Fig. 8a correspond to 100 µm. The dashed line exhibited in Fig. 24b is associated with a cell viability of 70%.

The fact of the bare Mg substrate displays cell viability of 59.2 ± 3.3 % after 72 h (3 days) seems to be contradictory to the biocompatibility commonly attributed to this material. Charyeva *et al.* [44] investigated the compatibility of Mg implants to primary human stem cells. They observed a decrease in the cell viability of Mg as a function of time; this value decreased from 93.4 ± 25.3 % to 13.9 ± 5.0 % when the first and seventh days are compared. However, the cell viability changed to 24.0 ± 19.5 % on the twenty-first day. It has been reported [45] that the increase of Mg's biocompatibility with time is related to its reaction with the physiological

medium: the initial corrosion of Mg leads to both the release of Mg^{2+} ions (Eq. 4.2) and the formation of an $Mg(OH)_2$ layer (Eq. 4) on it. At this time the corrosion rate slows down, and a second layer consisting of amino acids and organic matter is formed. Such layers can shield the physiological environment around the material and enable cells to grow on it, which could explain the increase of the cell viability with time. The decrease of cell viability on the first days may also be associated with the release of H_2 during the corrosion of Mg (Eq. 4.3), which can give rise to H_2O_2:

$$H_{2(g)} + O_{2(g)} \rightarrow H_2O_{2(l)} \tag{4.15}$$

Competing reactions to Eq. (4.15) may also take place:

$$2H_{2(g)} + O_{2(g)} \rightarrow 2H_2O_{(l)} \tag{4.16}$$

$$2H_2O_{2(l)} \rightarrow 2H_2O_{(l)} + O_{2(g)} \tag{4.17}$$

According to Lunsford [46], Eq. (15) to (17) are thermodynamically favorable at normal conditions and the yield of H_2O_2 depends on their relative rates. The contact of living cells with H_2O_2 can increase oxidative stress, leading to their death [47].

Fig. 23 depicts SEM micrographs of samples used in the cell viability assays. MSCs are observed on the surface of these specimens. The detachment of cells is noticed for the bare substrate, revealing a poor interaction between MSCs and this sample. On the other hand, an MSC is observed attached to CaP-24h. This finding is in line with the cell viability results exhibited in Fig. 23.b, where it was demonstrated that the bare Mg substrate is cytotoxic whereas CaP-24h is not. It has been reported that cell adhesion and spreading are of great importance in living biological processes and are observed in several natural phenomena, such as wound healing, immune response, metastasis, and tissue regeneration [22,48]. Thus, the adhesion of MSCs on CaP-24h and its biocompatibility reveals that this material is a promising material for use in biomedical applications.

Figure 23 – SEM micrographs taken after the cell viability assays. (a) and (b) are associated with the bare Mg substrate and CaP-24h, respectively. The scale bars displayed in these images correspond to 50 µm. SEM images obtained with secondary electrons.

4.4. CONCLUSIONS

In this work, a DCPD coating was formed on hot-rolled Mg substrates aiming to increase the corrosion resistance of the latter. The DCPD coating was obtained after immersion of Mg substrates in a phosphating bath for times ranging from 6 to 48 h. Some samples were heat-treated in air at 100 °C for 6 h to evaluate the effect of this step on their structural properties and corrosion behavior. This study was supported by a series of experimental tests, including XRD, FTIR, SEM, EIS, and *in vitro* assays. It was observed that the heat treatment of the coated samples gave rise to defects on the surface and a consequent decrease in their corrosion resistance. The sample soaked in the phosphating bath for 24 h was the one with the highest corrosion resistance, displaying a $|Z|$ of 16×10^3 $\Omega.cm^2$ at 30 mHz. A 14.0 ± 1.3 µm thick DCPD coating was observed on this material. This sample also exhibited the formation of a HAp layer on its surface after the soaking in HBSS for times as short as 1 day. Moreover, it was observed that this specimen showed no toxicity to MSCs after a 3-day MTT test, suggesting that it is a promising material for biomedical applications.

4.5. REFERENCES

[1] S. SHADANBAZ, G.J. DIAS, Calcium phosphate coatings on magnesium alloys for biomedical applications: A review, Acta Biomater. 8 (2012) 20–30. doi:10.1016/j.actbio.2011.10.016.

[2] H. BREME, V. BIEHL, N. REGER, E. GAWALT, Chapter 1a Metallic Biomaterials: Introduction, in: W. Murphy, J. Black, G. Hastings (Eds.), Handb. Biomater. Prop., Springer New York, New York, NY, 2016: pp. 151–158. doi:10.1007/978-1-4939-3305-1_14.

[3] F. WITTE, Reprint of: The history of biodegradable magnesium implants: A review, Acta Biomater. 23 (2015) S28–S40. doi:https://doi.org/10.1016/j.actbio.2015.07.017.

[4] M. PRAKASAM, J. LOCS, K. SALMA-ANCANE, D. LOCA, A. LARGETEAU, L. BERZINA-CIMDINA, Biodegradable materials and metallic implants - A review, J. Funct. Biomater. 8 (2017) 44. doi:10.3390/jfb8040044.

[5] T.S.N. SANKARA NARAYANAN, I.S. PARK, M.H. LEE, Strategies to improve the corrosion resistance of microarc oxidation (MAO) coated magnesium alloys for degradable implants: Prospects and challenges, Prog. Mater. Sci. 60 (2014) 1–71. doi:10.1016/j.pmatsci.2013.08.002.

[6] S. FINTOVÁ, J. DRÁBIKOVÁ, B. HADZIMA, L. TRŠKO, M. BŘEZINA, P. DOLEŽAL, J. WASSERBAUER, Degradation of unconventional fluoride conversion coating on AZ61 magnesium alloy in SBF solution, Surf. Coatings Technol. 380 (2019) 125012. doi:10.1016/j.surfcoat.2019.125012.

[7] H. ZREIQAT, C.R. HOWLETT, A. ZANNETTINO, P. EVANS, G. SCHULZE-TANZIL, C. KNABE, M. SHAKIBAEI, Mechanisms of magnesium-stimulated adhesion of osteoblastic cells to commonly used orthopaedic implants, J. Biomed. Mater. Res. 62 (2002) 175–184. doi:10.1002/jbm.10270.

[8] S. MOHAJERNIA, S. HEJAZI, A. ESLAMI, M. SAREMI, Modified nanostructured hydroxyapatite coating to control the degradation of magnesium alloy AZ31 in simulated body fluid, Surf. Coatings Technol. 263 (2015) 54–60. doi:10.1016/j.surfcoat.2014.12.059.

[9] J. GONZALEZ, R.Q. HOU, E.P.S. NIDADAVOLU, R. WILLUMEIT-RÖMER, F. FEYERABEND, Magnesium degradation under physiological conditions – Best practice,

Bioact. Mater. 3 (2018) 174–185. doi:10.1016/j.bioactmat.2018.01.003.

[10] M. ESMAILY, J.E. SVENSSON, S. FAJARDO, N. BIRBILIS, G.S. FRANKEL, S. VIRTANEN, R. ARRABAL, S. THOMAS, L.G. JOHANSSON, Fundamentals and advances in magnesium alloy corrosion, Prog. Mater. Sci. 89 (2017) 92–193. doi:10.1016/j.pmatsci.2017.04.011.

[11] C.L. CHU, X. HAN, J. BAI, F. XUE, P.K. Chu, Fabrication and degradation behavior of micro-arc oxidized biomedical magnesium alloy wires, Surf. Coatings Technol. 213 (2012) 307–312. doi:10.1016/j.surfcoat.2012.10.078.

[12] J.W. GUO, S.Y. SUN, Y.M. WANG, Y. ZHOU, D.Q. WEI, D.C. Jia, Hydrothermal biomimetic modification of microarc oxidized magnesium alloy for enhanced corrosion resistance and deposition behaviors in SBF, Surf. Coatings Technol. 269 (2015) 183–190. doi:10.1016/j.surfcoat.2015.02.010.

[13] M.S. SONG, R.C. ZENG, Y.F. DING, R.W. LI, M. EASTON, I. COLE, N. BIRBILIS, X.B. CHEN, Recent advances in biodegradation controls over Mg alloys for bone fracture management: A review, J. Mater. Sci. Technol. 35 (2019) 535–544. doi:10.1016/j.jmst.2018.10.008.

[14] S. BRUNDAVANAM, G. EDDY, J. POINERN, D. FAWCETT, Growth of flower-like brushite structures on magnesium substrates and their subsequent low temperature transformation to hydroxyapatite, Am. J. Biomed. Eng. 4 (2014) 79–87. doi:10.5923/j.ajbe.20140404.02.

[15] M.B. KANNAN, Electrochemical deposition of calcium phosphates on magnesium and its alloys for improved biodegradation performance: A review, Surf. Coatings Technol. 301 (2016) 36–41. doi:10.1016/j.surfcoat.2015.12.044.

[16] Y. SU, Y. GUO, Z. HUANG, Z. ZHANG, G. LI, J. LIAN, L. REN, Preparation and corrosion behavior of calcium phosphate conversion coating on magnesium alloy, Surf. Coatings Technol. 307 (2016) 99–108. doi:10.1016/j.surfcoat.2016.08.065.

[17] L.L. TAN, Q. WANG, F. GENG, X.S. XI, J.H. QIU, K. YANG, Preparation and characterization of Ca-P coating on AZ31 magnesium alloy, Trans. Nonferrous Met. Soc. China. 20 (2010) s648–s654. doi:10.1016/S1003-6326(10)60555-9.

[18] M.A.F. ZALUDIN, Z.A. ZAHID JAMAL, M.N. DERMAN, M.Z. KASMUIN,

Fabrication of calcium phosphate coating on pure magnesium substrate via simple chemical conversion coating: Surface properties and corrosion performance evaluations, J. Mater. Res. Technol. 8 (2019) 981–987. doi:10.1016/j.jmrt.2018.06.017.

[19] K. LI, B. WANG, B. YAN, W. LU, Microstructure in vitro corrosion and cytotoxicity of Ca-P coatings on ZK60 magnesium alloy prepared by simple chemical conversion and heat treatment, J. Biomater. Appl. 28 (2013) 375–384. doi:10.1177/0885328212453958.

[20] N. GROSSBLATT, ed., Guide for the care and use of laboratory animals, National Academy Press, 1996.

[21] International Standads Organization, Biological evaluation of medical devices, ISO 10993 - 52009 Biol. Eval. Med. Devices - Part 5 Tests Vitr. Cytotox. (2009) 1–34.

[22] H.S. COSTA, A.A.P. MANSUR, M.M. PEREIRA, H.S. MANSUR, Engineered hybrid scaffolds of Poly(vinyl alcohol)/bioactive glass for potential bone engineering applications: Synthesis, characterization, cytocompatibility, and degradation, J. Nanomater. 2012 (2012) 1–16. doi:10.1155/2012/718470.

[23] S. NATH, R. TU, T. GOTO, Apatite formation in Hanks' solution on β-Ca_2SiO_4 films prepared by MOCVD, Surf. Coatings Technol. 206 (2011) 172–177. doi:10.1016/j.surfcoat.2011.07.014.

[24] P.A.A.P. MARQUES, A.P. SERRO, B.J. SARAMAGO, A.C. FERNANDES, M.C.F. MAGALHÃES, R.N. CORREIA, Mineralisation of two calcium phosphate ceramics in biological model fluids, J. Mater. Chem. 13 (2003) 1484–1490. doi:10.1039/b211402j.

[25] R.C. ZENG, X.T. LI, S.Q. LI, F. ZHANG, E.H. HAN, In vitro degradation of pure Mg in response to glucose, Sci. Rep. 5 (2015) 13026. doi:10.1038/srep13026.

[26] Y. ZONG, G. YUAN, X. ZHANG, L. MAO, J. NIU, W. DING, Comparison of biodegradable behaviors of AZ31 and Mg-Nd-Zn-Zr alloys in Hank's physiological solution, Mater. Sci. Eng. B Solid-State Mater. Adv. Technol. 177 (2012) 395–401. doi:10.1016/j.mseb.2011.09.042.

[27] G.Y. LI, J.S. LIAN, L.Y. NIU, Z.H. JIANG, Influence of pH of phosphating bath on the zinc phosphate coating on AZ91D magnesium alloy, Adv. Eng. Mater. 8 (2006) 123–127. doi:10.1002/adem.200500095.

[28] Q.Y. XIONG, Y. ZHOU, J.P. XIONG, The study of a phosphate conversion coating on magnesium alloy AZ91D: II. Effects of components and their content in phosphating bath, Int. J. Electrochem. Sci. 10 (2015) 8454–8464.

[29] M.C. KUO, S.K. YEN, The process of electrochemical deposited hydroxyapatite coatings on biomedical titanium at room temperature, Mater. Sci. Eng. C. 20 (2002) 153–160. doi:10.1016/S0928-4931(02)00026-7.

[30] A.C. PEDREIRA DE FREITAS, L.C. ESPEJO, S.B. BOTTA, F. DE S. TEIXEIRA, M.A.A.C. LUZ, N. GARONE-NETTO, A.B. MATOS, M.C.B. DA S. SALVADORI, AFM analysis of bleaching effects on dental enamel microtopography, Appl. Surf. Sci. 256 (2010) 2915–2919. doi:10.1016/j.apsusc.2009.11.050.

[31] Y. WANG, M. WEI, J. GAO, Improve corrosion resistance of magnesium in simulated body fluid by dicalcium phosphate dihydrate coating, Mater. Sci. Eng. C. 29 (2009) 1311–1316. doi:10.1016/j.msec.2008.09.051.

[32] R.M. FONSECA, R.B. SOARES, R.G. CARVALHO, E.K. TENTARDINI, V.F.C. LINS, M.M.R. CASTRO, Corrosion behavior of magnetron sputtered NbN and $Nb_{1-x}Al_xN$ coatings on AISI 316L stainless steel, Surf. Coatings Technol. 378 (2019) 124987. doi:10.1016/j.surfcoat.2019.124987.

[33] M.E. ORAZEM, N. PÁÈRE, B. TRIBOLLET, Enhanced graphical representation of electrochemical impedance data, J. Electrochem. Soc. 153 (2006) B129–B136. doi:10.1149/1.2168377.

[34] M.T. FULMER, P.W. BROWN, Hydrolysis of dicalcium phosphate dihydrate to hydroxyapatite, J. Mater. Sci. Mater. Med. 9 (1998) 197–202. doi:10.1023/A:1008832006277.

[35] I.S. RONCEVIC, Z. GRUBAC, M. METIKOS-HUKOVIC, Electrodeposition of hydroxyapatite coating on AZ91D alloy for biodegradable implant application, Int. J. Electrochem. Sci. 9 (2014) 5907–5923.

[36] I. PETROV, B. ŠOPTRAJANOV, N. FUSON, J.R. LAWSON, Infra-red investigation of dicalcium phosphates, Spectrochim. Acta Part A Mol. Spectrosc. 23 (1967) 2637–2646. doi:10.1016/0584-8539(67)80155-7.

[37] J. XU, I.S. BUTLER, D.F.R. GILSON, FT-Raman and high-pressure infrared

spectroscopic studies of dicalcium phosphate dihydrate ($CaHPO_4 \cdot 2H_2O$) and anhydrous dicalcium phosphate (CaHPO4), Spectrochim. Acta - Part A Mol. Biomol. Spectrosc. 55 (1999) 2801–2809. doi:10.1016/S1386-1425(99)00090-6.

[38] A. ZAVATTINI, V.P. FEITOSA, F. MANNOCCI, F. FOSCHI, A. BABBAR, A. LUZI, L. OTTRIA, F. MANGANI, I. CASULA, S. SAURO, Bonding ability of experimental resin-based materials containing (ion-releasing)-microfillers applied on water-wet or ethanol-wet root canal dentine, Int. J. Adhes. Adhes. 54 (2014) 214–223. doi:https://doi.org/10.1016/j.ijadhadh.2014.06.007.

[39] A. RAINER, S.M. GIANNITELLI, F. ABBRUZZESE, E. TRAVERSA, S. LICOCCIA, M. TROMBETTA, Fabrication of bioactive glass-ceramic foams mimicking human bone portions for regenerative medicine, Acta Biomater. 4 (2008) 362–369. doi:10.1016/j.actbio.2007.08.007.

[40] D.M.M. DOS SANTOS, S.M. DE CARVALHO, M.M. PEREIRA, M. HOUMARD, E.H.M. NUNES, Freeze-cast composite scaffolds prepared from sol-gel derived 58S bioactive glass and polycaprolactone, Ceram. Int. 45 (2019) 9891–9900. doi:10.1016/j.ceramint.2019.02.030.

[41] E.A. AGUILAR-REYES, C.A. LEÓN-PATIÑO, E. VILLICAÑA-MOLINA, V.I. MACÍAS-ANDRÉS, L.P. LEFEBVRE, Processing and in vitro bioactivity of high-strength 45S5 glass-ceramic scaffolds for bone regeneration, Ceram. Int. 43 (2017) 6868–6875. doi:10.1016/j.ceramint.2017.02.107.

[42] D. SANTOS, T. MARTINS, S. CARVALHO, M. PEREIRA, M. HOUMARD, E. NUNES, Simple preparation of 58S bioactive glass/polycaprolactone composite scaffolds by freeze-drying under ambient conditions, Mater. Lett. 256 (2019) 126647(1-4). doi:10.1016/j.matlet.2019.126647.

[43] S. CHESHKOV, I.E. DIMITROV, V. JAKKAMSETTI, L. GOOD, D. KELLY, K. RAJASEKARAN, R.J. DEBERARDINIS, J.M. PASCUAL, A.D. SHERRY, C.R. MALLOY, Oxidation of [U-13C]glucose in the human brain at 7T under steady state conditions, Magn. Reson. Med. 78 (2017) 2065–2071. doi:10.1002/mrm.26603.

[44] O. CHARYEVA, O. DAKISCHEW, U. SOMMER, C. HEISS, R. SCHNETTLER, K.S. LIPS, Biocompatibility of magnesium implants in primary human reaming debris-derived cells stem cells in vitro, J. Orthop. Traumatol. 17 (2016) 63–73. doi:10.1007/s10195-015-0364-9.

[45] R. WILLUMEIT, J. FISCHER, F. FEYERABEND, N. HORT, U. BISMAYER, S. HEIDRICH, B. MIHAILOVA, Chemical surface alteration of biodegradable magnesium exposed to corrosion media, Acta Biomater. 7 (2011) 2704–2715. doi:10.1016/j.actbio.2011.03.004.

[46] J.H. LUNSFORD, The direct formation of H_2O_2 from H_2 and O_2 over palladium catalysts, in: J. Catal., 2003: pp. 455–460. doi:10.1016/S0021-9517(02)00070-2.

[47] G. GILLE, K. SIGLER, Oxidative stress and living cells, Folia Microbiol. (Praha). 40 (1995) 131–152. doi:10.1007/BF02815413.

[48] H.S. COSTA, M.F. ROCHA, G.I. ANDRADE, E.F. BARBOSA-STANCIOLI, M.M. PEREIRA, R.L. Orefice, W.L. Vasconcelos, H.S. Mansur, Sol-gel derived composite from bioactive glass-polyvinyl alcohol, in: J. Mater. Sci., 2008: pp. 494–502. doi:10.1007/s10853-007-1875-4.

5. MODIFICAÇÃO DA SUPERFÍCIE DO MAGNÉSIO COM REVESTIMENTO COMPÓSITO PARA APLICAÇÃO EM ENGENHARIA DE TECIDO ÓSSEO

Nesse trabalho, investigou-se a modificação superficial do compósito Mg/DCPD com recobrimento composto por PVA e BG. O teor de BG nas soluções de revestimento preparadas variou entre 2 e 10% vol./vol. Foi observado que os revestimentos compostos aumentaram a proteção anticorrosiva do Mg, o que foi verificado por EIS. Foi também demonstrado que a solubilidade do PVA em meios biológicos pode ser adaptada cruzando suas cadeias moleculares adjacentes com ácido cítrico (CA). A amostra contendo uma carga de BG de 10% vol./vol. foi a de maior resistência à corrosão, o que está relacionada com a grande espessura do revestimento obtido (cerca de 200 μm). Além disso, esta amostra favoreceu uma rápida formação de cristais HAp sobre a superfície composta, revelando sua biocompatibilidade. Ensaios de citometria de fluxo indicaram que estes compósitos apresentam alta viabilidade celular (superior 90%) quando são consideradas as células renais embrionárias humanas, reforçando seu uso promissor como biomaterial.

Submetido para-Surface & Coatings Technology.

SURFACE MODIFICATION OF MAGNESIUM WITH COMPOSITE COATINGS FOR APPLICATION IN BONE TISSUE ENGINEERING

ABSTRACT

Magnesium (Mg) and its alloys are promising candidates for use in bone tissue engineering due to their good biocompatibility and mechanical stability. Nonetheless, the fast biodegradation of Mg in physiological media inhibits its use as a bone graft. Aiming to improve its corrosion resistance, a dicalcium phosphate dehydrate (DCPD) coating was initially deposited on the hot-rolled Mg substrates by immersing them in a phosphating bath at room temperature for 24 h. Polyvinyl alcohol-bioactive glass (PVA-BG) composite coatings were then deposited on these materials. The samples prepared here were examined according to their structure, corrosion behavior, and biocompatibility. We observed that the composite coatings greatly increased the corrosion protection of Mg, and also accelerated the formation of HAp on its surface when soaked in a simulated body fluid (SBF) solution. Flow cytometry assays revealed that the composites prepared have high cell viability (over 90%) when immortalized human embryonic kidney cells are tested. The coating method suggested in this work is simple, environmentally friendly, safe, and easily scalable. It is the first time that this approach is reported in the literature, which highlights its novelty.

KEYWORDS: Magnesium; Bone tissue engineering; Polyvinyl alcohol; Bioactive glass; Corrosion behavior; Biocompatibility.

5.1. INTRODUCTION

It is estimated that over 2 million bone grafts are performed annually worldwide [1]. The best option would be to use autologous bone grafts, which do not require any processing and provide an osteoinductive graft material [2]. However, autologous tissue is limited by the graft size and shape, and by issues related to the donor site morbidity. Moreover, the amount of natural bone grafts currently available is far from meeting the clinical demands, especially considering the aging and obesity of the world population [3]. Consequently, great attention has been paid to synthetic materials that can repair or restore functions of defective systems. Therefore, metallic grafts have been widely investigated due to their higher mechanical stability compared to polymers and ceramics [4].

Metallic magnesium (Mg) and its alloys have been reported to show high biocompatibility to the human body [5–8]. These materials also display good mechanical and electrochemical behaviors, making Mg a promising material for application in bone tissue engineering [9,10]. However, the fast biodegradation of Mg in physiological media has been a significant concern in several works [11–14]. Aiming to decrease its biodegradation rate, Mg has been surface modified to create a protective layer and allow its persistence at the grafted site for longer periods [15,16]. This property is critical to ensure that the implant can maintain its mechanical integrity during the entire healing period. Despite the several works conducted in past years dealing with the Mg biocorrosion, researchers agree that the mechanisms involved in this process are far from a complete understanding, and much effort must be made to elucidate them [11,17].

In a previous work [18], we deposited dicalcium phosphate dihydrate (DCPD) coatings on hot-rolled Mg by a chemical conversion route. It is well established that hot rolling gives rise to fine-grained Mg samples with improved corrosion resistance [19]. In that study [18], Mg substrates were soaked at room temperature in a phosphating bath for times ranging from 6 h to 48 h. We observed that the specimens immersed in the phosphating bath for 24 h were those with the highest corrosion resistance, displaying an impedance modulus (|Z|) of 16×10^3 Ω.cm^2 at 30 mHz. On the other hand, the bare Mg substrate exhibited |Z| of 3.5×10^3 Ω.cm^2 at the same frequency, revealing that it corroded faster than the coated samples. The presence of DCPD also positively affected the biological behavior of Mg, promoting a rapid formation of hydroxyapatite (HAp) on its surface when soaked in a Kokubo's simulated body fluid (SBF): HAp was observed on DCPD-coated samples after the first day of soaking in SBF.

In this work, we deposited polyvinyl alcohol-bioactive glass (PVA-BG) composite films on DCPD-coated Mg substrates. As far as we know, this is the first time this approach is reported in the literature. PVA is a hydrophilic and biodegradable polymer widely used in tissue engineering [20,21], while BG is a bioceramic commonly employed to repair and regenerate damaged tissues and organs [22]. BG was initially developed by Hench and co-workers [23] by a melting-quenching method. Here we synthesized BG by the sol-gel process, which gives rise to samples with higher specific surface areas and pore volumes compared to melt-quenched specimens. Such properties play a key role in the biological response of biomaterials [24]. The substrates were dipped in an alcoholic solution of PVA-BG and air-dried at 90 °C. The obtained materials were examined by scanning electron microscopy (SEM), energy-dispersive X-ray spectroscopy (EDS), X-ray diffraction (XRD), Fourier transform infrared spectroscopy (FTIR), electrochemical impedance spectroscopy (EIS), laser granulometry, and N_2 sorption. We also evaluated the cytotoxicity of the prepared samples by flow cytometry. Their biocompatibility was examined after soaking in SBF for up to 21 days.

5.2. MATERIALS AND METHODS

5.2.1. PREPARATION OF Mg SUBSTRATES

Mg ingots (99.7% purity) were provided by RIMA (Bocaiúva-MG). Flat plates were obtained from these ingots after four hot-rolling passes at 300 °C in air. Substrates with dimensions about 20 mm× 20 mm × 1 mm were cut from these plates. The substrates were subsequently ground with silicon carbide papers of different abrasive grit sizes (up to #4000 grit), cleaned with deionized water, and sonicated at room temperature for 15 min in absolute ethanol (EtOH, 99.6%, Synth). As discussed earlier, hot-rolled Mg displays both a fine-grained microstructure and improved corrosion resistance. [19]

5.2.2. SOL-GEL SYNTHESIS OF BG

BG 58S (molar composition (%): $60SiO_2–36CaO–4P_2O_5$) was prepared by sol-gel process following a procedure described in detail elsewhere [25]. Briefly, an acidic aqueous solution (pH 2) was initially prepared by mixing deionized water and nitric acid (HNO_3, Synth, 70%).

The silicon precursor (Tetraethyl orthosilicate, TEOS, Aldrich, 98%) was dropwise added to this solution, and the molar ratio of TEOS: H_2O was adjusted to 12: 1. The as-prepared solution was kept under stirring at room temperature for 60 min. Triethyl phosphate (TEP, Aldrich, ≥ 99.8%) and calcium nitrate tetrahydrate (CNTH, Vetec, ≥ 98%) were then added to the solution, the latter being added 1 h after the former. The obtained solution was stirred for 1 h at room temperature and then poured into polytetrafluoroethylene (PTFE) molds and aged at 60 °C for 72 h. The as-prepared monoliths were powdered in an agate mortar and air-dried at 120 °C for up to 5 days. BG was subsequently heat-treated in air at 700 °C for 6 h using a heating rate of 1 °C.min^{-1}. BG particles were then dry milled for about 8 h in a ball mill to break the particle agglomerates.

5.2.3. COATING PROCESS

A DCPD layer was initially deposited on the hot-rolled substrates by a chemical conversion route [18]. The substrates were soaked at room temperature for 24 h in a solution of CNTH (12 g.L^{-1}), calcium oxide (CaO, Aldrich, 1.2 g.L^{-1}), and phosphoric acid (PAc, 85 wt.% in water, Aldrich, 8 mL.L^{-1}). The bath pH was kept constant at 2.8. After the immersion step, the DCPD-coated samples were rinsed with deionized water and air-dried at room temperature. Simultaneously, PVA pellets (M_w = 9,000 – 10,000 g.mol^{-1} / 80% hydrolyzed, Aldrich) were dissolved under stirring at room temperature in a solution of deionized water and EtOH (30 vol.%). The previously prepared BG particles were co-added with citric acid (CA, ≥ 99.5%, Aldrich) to this solution, and the CA loading was kept at 1 wt.% of the BG concentration. The BG loading in the prepared solutions varied from 2 vol.% (6.1 wt.%) to 10 vol.% (26.1 wt.%). The DCPD-coated substrates were dipped into the PVA/BG-containing solutions and removed at a withdrawal rate of 2 mm.s^{-1}. The samples were air-dried at 90 °C for about 5 min after each dip-coating step. Three dip-coating steps were applied to each sample. Specimens coated with DCPD were designated as Mg_DCPD, while samples coated with DCPD and PVA/BG composite films were labeled as Mg_DCPD_PVA/BG (X vol.%), where X represents the loading of BG. Figure 24 summarizes the experimental work performed to prepare the samples used in this work.

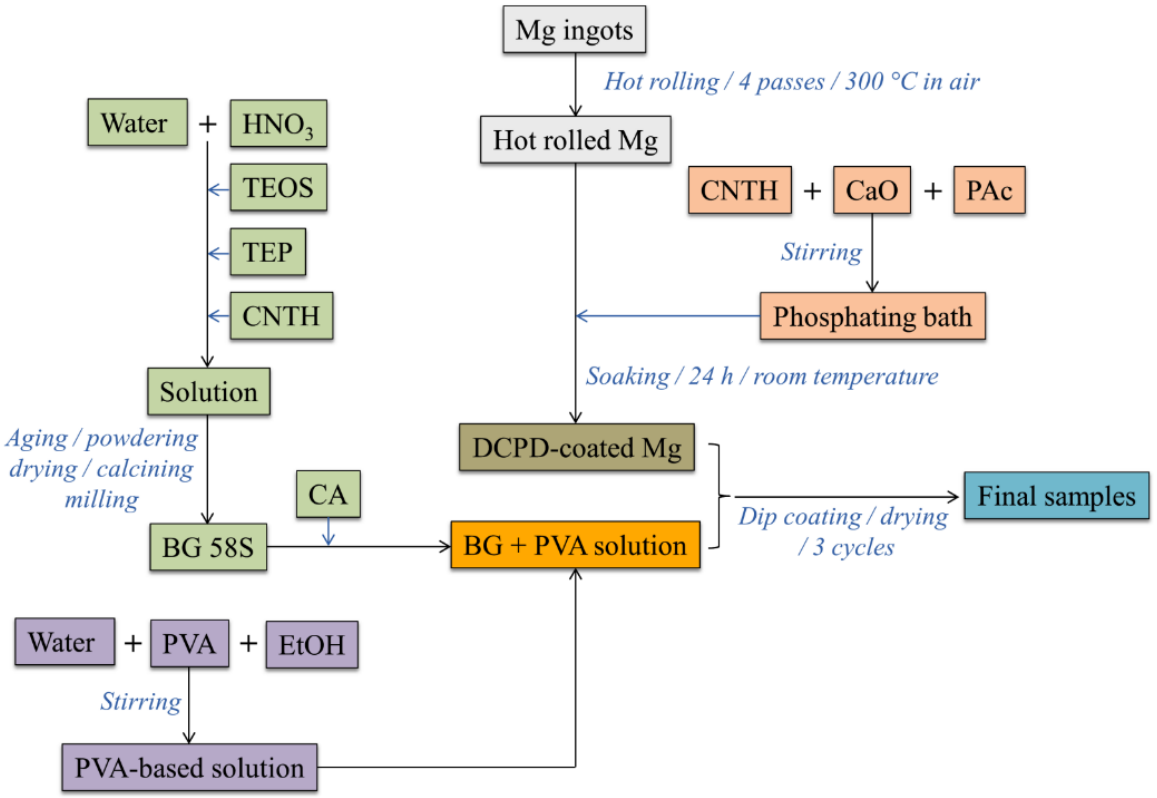

Figure 24 – Schematic representation of the methodology used to prepare the coated samples.

5.2.4. CHARACTERIZATIONS

SEM was conducted on a Jeol JSM-6360LV microscope at an accelerating voltage of 20 kV using samples previously sputter-coated with gold. EDS was carried out with the Thermo Noran system available in the electron microscope. XRD was carried out on a Philips Panalytical PW1710 diffractometer at a scanning rate of 0.06°.s^{-1}. CuKα (λ = 1.54 Å) was employed as the X-ray radiation source. FTIR was performed on a Bruker Alpha spectrometer, using an attenuated total reflectance (ATR) accessory and a diamond crystal as the reflective element. The spectra were taken at a resolution of 4 cm^{-1} and 128 scans. N_2 sorption was conducted on a Quantachrome Nova 1200e system, using samples previously degassed under vacuum at 100 °C overnight. The multipoint Brunauer-Emmett-Teller (BET) method and non-local density functional theory (NLDFT) were used to obtain the specific surface area and pore size distribution. Laser granulometry was performed on a Cilas 1064 granulometer and using the Fraunhofer method. These tests were carried out using filtered water as the dispersing medium and no surfactant. EIS was performed at room temperature on an Autolab PGSTAT 100 N potentiostat using SBF as the electrolyte. In these tests, three electrodes were used: the Mg sample as the working electrode, platinum as the counter-electrode, and saturated calomel as

the reference electrode. The surface area assessed in these tests was kept constant at 1.2 cm^2. Such experiments were carried out at the corrosion potential using an amplitude of 10 mV and at a frequency range from 10 kHz to 10 mHz. It was also used a previous open circuit potential (OCP) stabilization of 60 min.

5.2.5. *IN VITRO* ASSAYS

SBF was prepared following the procedure described by Kokubo and Takadama [26]. SBF mimics human blood plasma concerning ion concentration and pH. The HAp formation while soaking a material in this solution is an essential reference to endorse its bioactivity because HAp is responsible for binding the implant to the bone and ensuring biological functions during regeneration [27,28]. The samples were soaked in SBF at 36.5 °C and pH 7.4 for up to 21 days. They were removed from SBF at different times, rinsed with deionized water, and examined by SEM, XRD, and FTIR.

To evaluate the cytotoxicity profile of the prepared samples, a human cell line (immortalized embryonic kidney cells / ATCC® CRL-1573; HEK-293) was used. The cells were cultured in 50 mL cell culture flasks. Dulbecco's modified eagle medium (DMEM / Aldrich) (4500 $mg.L^{-1}$ glucose; 4 M glutamine; 11 $mg.L^{-1}$ sodium pyruvate; 3.7 $g.L^{-1}$ sodium bicarbonate) supplemented with fetal bovine serum (10%) and streptomycin (1%) was used as the culture medium. The cells were incubated at 37 °C in a CO_2 incubator (Thermo 311) with a controlled atmosphere (95% O_2; 5% CO_2) and humidity. After proper confluence, about 10^8 cells were transferred to cell culture plates with 12 wells in which the composites prepared here were previously added. The cells were seeded only over the samples' surface and kept at 37 °C for 24 h in a CO_2 incubator to cell adhesion. The following experimental groups were established (n = 3 per group): (i) sterile NaCl solution (0.9% (wt./vol.)), as negative control; (ii) DMSO solution (20 %), as positive control; (iii) samples. All experiments from cell culture and flow cytometry assays were carried out following the biosecurity standards described by the ISO 10993-5 [29]. All used materials were previously sterilized, and all steps of cell manipulation were performed in a biological safety cabinet BIOSEG 12, Class II type A1 (Veco Group, São Paulo, Brazil). Flow cytometry analysis was performed using a Fixable Viability Stain® V450-A (BD Biosciences - São Paulo, Brazil) kit, which was able to discriminate the living cells from the unviable ones. The tests were conducted in duplicates, and for each sample 10.000 events were acquired. Parameters such as side scattering (SSC), forward side scattering (FSC), and V450 emission were taken into consideration.

5.3. RESULTS AND DISCUSSION

5.3.1. STRUCTURAL CHARACTERIZATION

- BG 58S

Figure 25a displays an XRD pattern collected for BG 58S, where a broad halo commonly attributed to amorphous structures is observed [30]. It has been reported that the presence of an amorphous network favors the bioactivity of BG due to an improved ions exchange with the surrounding body [31–33]. The particle size distribution of BG after the milling stage is exhibited in Figure 25.b. This material has a mean particle size ($\bar{\phi}$) of 20 μm. The milling step is mandatory to break the particles agglomerates and ensure their good dispersion in the slurry used in dip-coating; the value assessed for $\bar{\phi}$ before the milling step was over 200 μm, which is related to large particle agglomerates. A well-dispersed suspension is required to obtain homogeneous coatings with no apparent defects. The inset displayed in Figure 25.b is associated with an SEM micrograph of BG. Particles with irregular shapes and sharp edges are observed in this image. These particles also have a broad size distribution, which agrees with the histogram displayed in Figure 25b.

Figure 25c shows the ATR-FTIR spectrum taken for BG. The absorption bands at 450 cm^{-1} and 1030 cm^{-1} are related to Si-O bonds [34]. The shoulder at 960 cm^{-1} is due to silanol groups (Si-OH) [35], while the band at 1630 cm^{-1} has been associated with physisorbed water [36]. The broad absorption bands centered at about 1425 cm^{-1} and 3450 cm^{-1} are attributed to C-O vibrations from CO_3 [37] and hydroxyl groups [36]. The duplet at 2350 cm^{-1} is due to atmospheric CO_2 [38]. The spectrum exhibited in Figure 25c reveals that BG was successfully prepared. Figure 25d displays an N_2 sorption isotherm obtained for this material. This curve can be classified as a type-IV isotherm with an H_2 hysteresis loop, revealing that BG has a mesoporous network [39]. The specific surface area of this material was estimated at 280 $m^2.g^{-1}$. The inset depicted in Figure 25d is related to the pore size distribution evaluated by the NLDFT method. One observes that the examined sample exhibits a significant presence of pores around 7.5 nm, which is within the mesopores size range. As discussed before, the high porosity observed in sol-gel-derived BG plays a crucial role in its biological response, favoring the bioabsorption and integration of BG with living tissues [24].

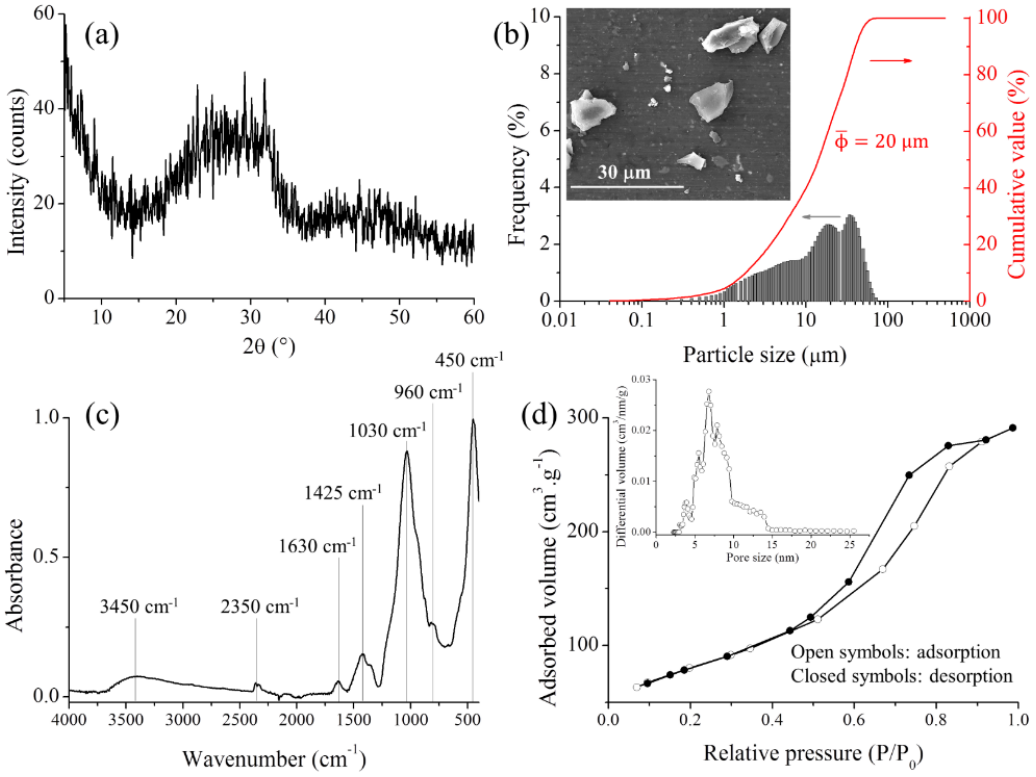

Figure 25 – (a) XRD pattern, (b) particle size distribution, (c) FTIR spectrum, and (d) N_2 sorption isotherm of the BG sample prepared here. Insets: (b) SEM micrograph of BG particles, and (d) pore size distribution evaluated by NLDFT method.

- HOT ROLLED Mg AND DCPD-COATED SAMPLES

Figure 26a displays SEM micrographs of an Mg substrate where grooves related to the hot rolling step are observed. Figure 26b shows a DCPD-coated sample after soaking in the phosphating bath. Flakes with a flower-like appearance are noted in these micrographs, which have already been associated with DCPD [40]. EDS examinations pointed out that these structures have a stoichiometric ratio of Ca: P equal to 1: 1, confirming that they can be due to DCPD. As depicted in Figure 26c, XRD also revealed the formation of DCPD on the Mg surface after soaking in the phosphating bath. The mechanisms associated with the formation of DCPD and its effect on the corrosion behavior of Mg are deeply discussed elsewhere [18]. The DCPD coating played an essential role in this work as an intermediate layer between the Mg substrate and PVA-BG top layer. We believe that the high porosity of DCPD allowed the penetration of the PVA-BG solution into it, favoring the top layer adhesion. Besides, as discussed further, DCPD contributes significantly to the corrosion resistance of Mg by acting as a first protective layer [18].

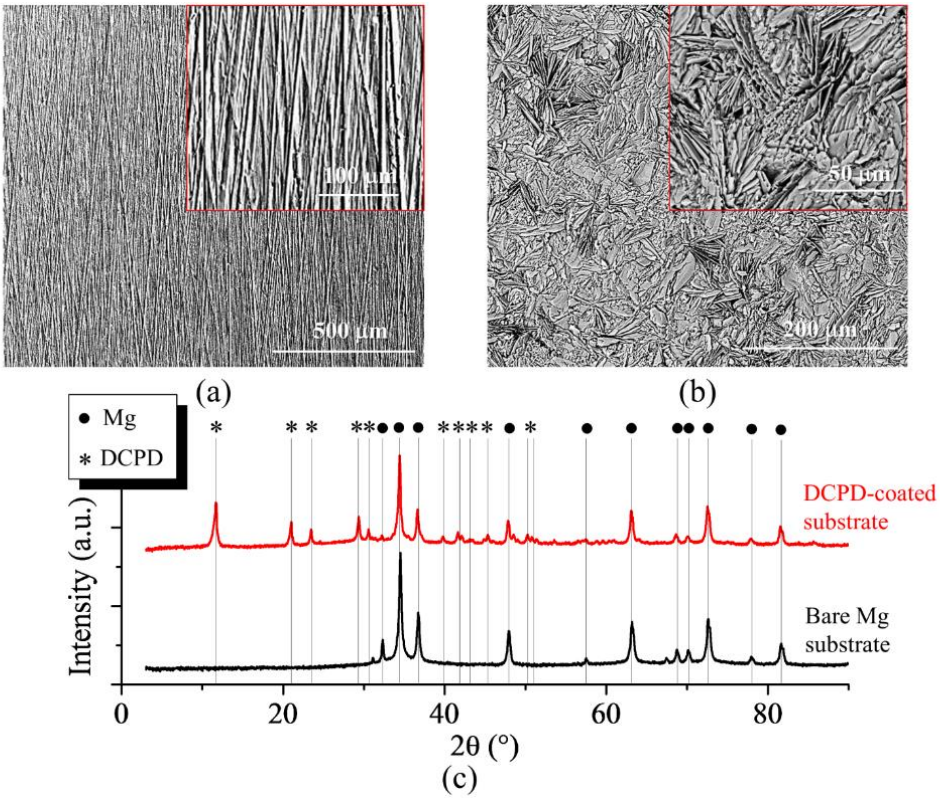

Figure 26 – SEM images of (a) bare and (b) DCPD-coated Mg substrates. (c) XRD patterns of an Mg sample before and after the deposition of DCPD on it. The JCPDS file numbers 35-0821 and 72-1240 were used as references for Mg and DCPD, respectively.

- SAMPLES COATED WITH PVA/BG COMPOSITE FILMS

Figure 27 exhibits SEM micrographs of Mg_DCPD_PVA/BG composites. One observes that the higher the loading of BG in the coating solution, the more visible the glass particles present on the substrate are. DCPD-related flakes are visible in Figures 27a and 27b which are associated with samples containing 2 and 6 vol.% BG loading, but are not noticeable in Figure 27c which is related to a specimen with 10 vol.% BG loading. It is worth noting that the deposition of PVA/BG films with a 10 vol.% BG loading led to homogeneous coatings, where no apparent defects are observed (Figure 27c). Figure 27 also depicts a schematic representation of the composites obtained. BG particles were kept adhered to the DCPD surface by the PVA molecular chains. As discussed earlier, the porosity of the DCPD allowed the penetration of PVA molecular chains into it, favoring the adhesion of the PVA/BG top layer. Figure 28 depicts the composition map of Mg_DCPD_PVA/BG (10 vol.%). From this Figure, it is possible to observe the spatial distribution of DCPD and BG in this composite, considering the arrangement of Ca, P, and Si.

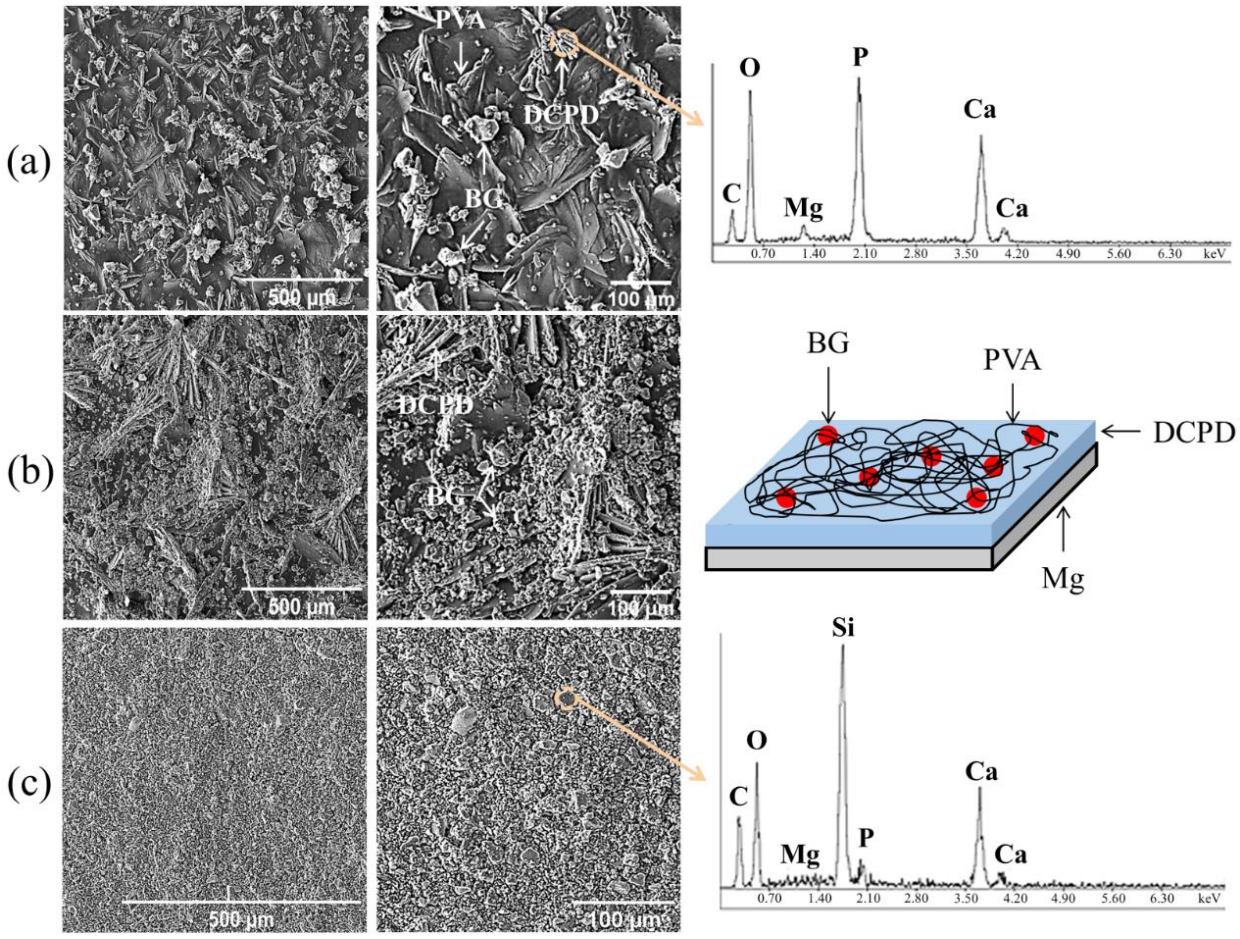

Figure 27 – SEM micrographs of Mg_DCPD_PVA/BG composites prepared using different BG loadings. The concentration of BG in (a), (b), and (c) are 2, 6, 10 vol.%, respectively.

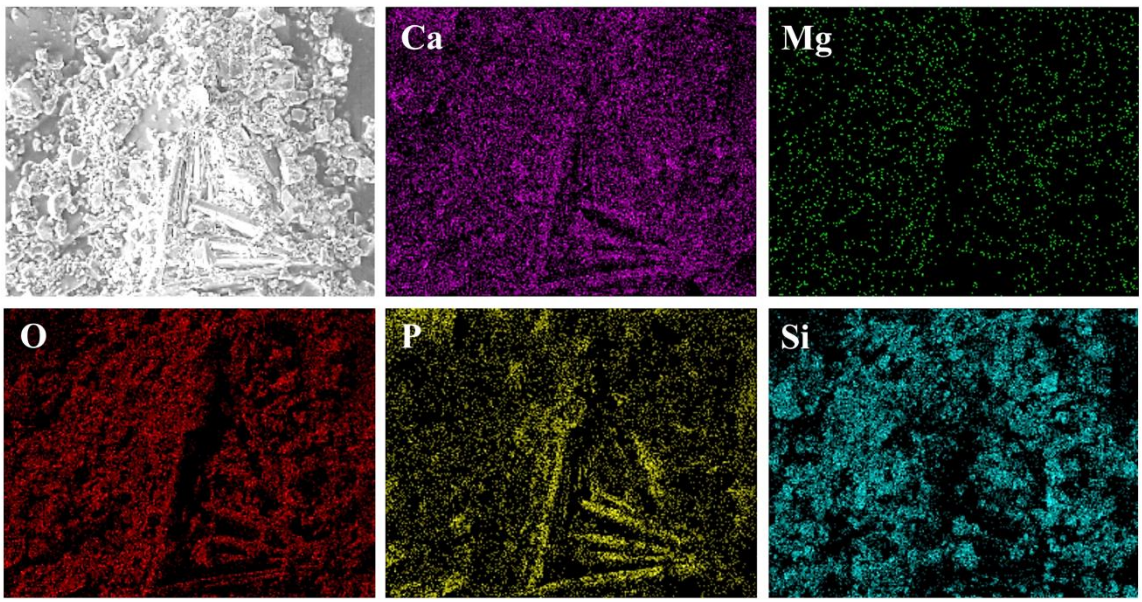

Figure 28 – Composition map obtained by EDS for Mg_DCPD_PVA/BG (10 vol.%).

Figure 29 displays an ATR-FTIR spectrum collected for Mg_DCPD_PVA/BG (10 vol.%). Reference spectra were taken for BG, PVA, CA, and DCPD and are also shown in Figure 28. The absorption bands at 400 cm^{-1}, 520 cm^{-1}, 575 cm^{-1}, and 650 cm^{-1} have been ascribed to the PO bending mode [41,42]. The bands at 785 cm^{-1}, 1200 cm^{-1}, and 1645 cm^{-1} are due to structural water [43]. The stretching of P–OH bonds is observed at 872 cm^{-1}, whereas the PO stretching mode can be identified at 985 cm^{-1}, 1054 cm^{-1}, and 1117 cm^{-1} [41–43]. The contributions due to BG increased the absorbance measured at about 400 cm^{-1} and 1000 cm^{-1}. As mentioned before, BG has two absorption bands at 450 cm^{-1} and 1030 cm^{-1} due to Si-O bonds [24] (Figure 25c), leading to a higher absorbance in these spectral ranges for the composite. It appears that the bands at 1435 cm^{-1} and 1716 cm^{-1} have contributions of CA and PVA. Such bands are ascribed to C–H bonds from CH_2 groups and the stretching vibration of carbonyl groups [44]. The peak at 2936 cm^{-1} seems to be related to PVA; it has been assigned to CH_2 groups of PVA backbone [45]. The band at 3154 cm^{-1} and the duplet at 3472 cm^{-1} and 3533 cm^{-1} seem to be related to DCPD; they have already been reported for DCPD films [46]. CA mainly contributes to the absorption band at 3255 cm^{-1}, which has been attributed to O–H bonds [47].

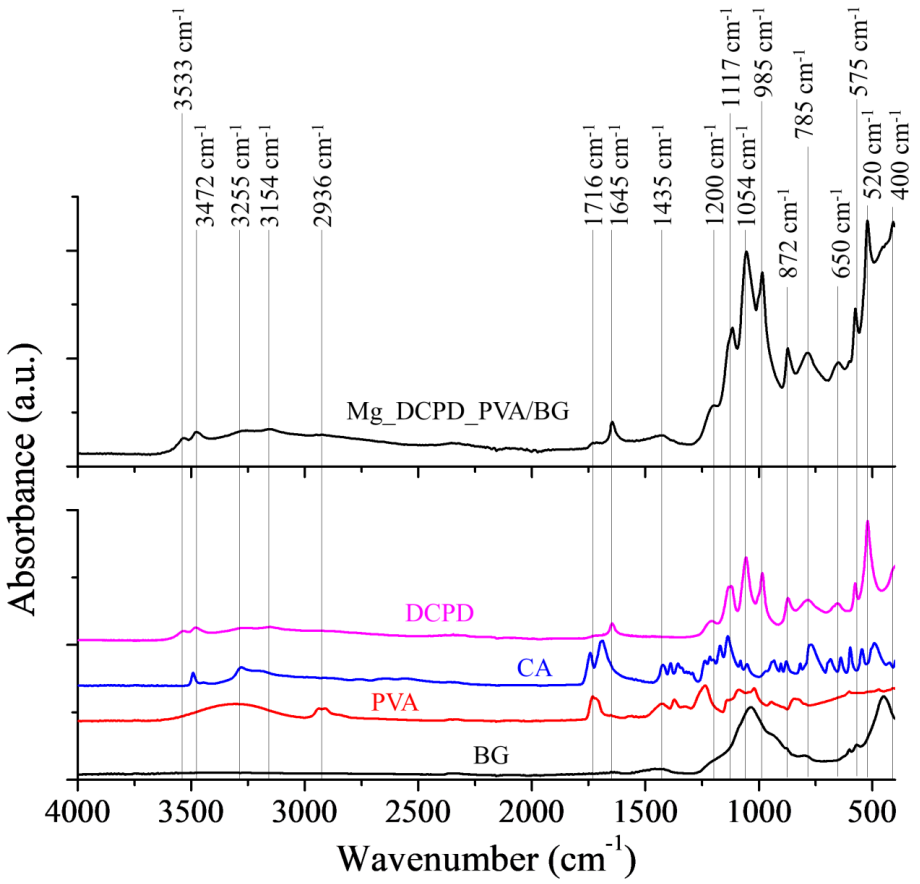

Figure 29 – Typical ATR-FTIR spectrum obtained for the Mg_DCPD_PVA/BG composites prepared here. The BG loading in this sample was 10 vol.%. Reference spectra of BG, CA, PVA, and DCPD are also exhibited in this Figure.

5.3.2. CORROSION TESTS

Figures 30a and 30b display the Bode plots obtained from EIS. It appears that three-to-four-time constants are observed in the examined materials. The first-time constant is associated with the interface between the PVA/BG composite films and SBF at high frequencies. Other time constants are observed as this coating degrades and new interfaces are created. It can be stated that Mg_DCPD_PVA/BG (10 vol.%) showed the highest corrosion resistance among the examined specimens, which can be observed from the high phase angle and |Z| obtained for this material. Figures 30c and 30d exhibit the equivalent electrical circuits modeled from the EIS curves. It is important to note that because they are not ideal capacitors, constant phase elements (CPEs) were also used to describe the capacitive properties of the examined samples. Figure 29c refers to the bare hot-rolled Mg, where Rs, R1, and R2 are assigned to the electrical resistances of SBF, MgO/Mg $(OH)_2$, and the Mg substrate. The mechanism attributed to the oxidation of Mg in aqueous media involves the oxidation of metal atoms to form ionic species and the release of electrons (Equation (5.1)). The reactions described in Equations (5.2) and

(5.3) occur in acidic environments, while Equations (5.4) and (5.5) take place in neutral and alkaline media [17,47].

$$Mg_{(s)} \longrightarrow Mg^{2+}_{(aq)} + 2e^- \quad (5.1)$$

$$2H^+_{(aq)} + 2e^- \longrightarrow H_{2(g)} \quad (5.2)$$

$$2H_2O_{(l)} + 2e^- \longrightarrow H_{2(g)} + 2OH^-_{(aq.)} \quad (5.3)$$

$$O_2 + 4H^+_{(aq)} + 4e^- \longrightarrow 2H_2O_{(l)} \quad (5.4)$$

$$O_2 + 2H_2O_{(l)} + 4e^- \longrightarrow 4OH^-_{(aq)} \quad (5.5)$$

The overall reaction for Mg corrosion can be written as given in Equation (5.6).

$$Mg_{(s)} + H_2O_{(l)} \longrightarrow Mg(OH)_{2(s)} + H_{2(g)} \quad (5.6)$$

It is important to mention the so-called negative difference effect (NDE) that takes place during the Mg corrosion. This phenomenon has been used to justify the anomalous occurrence of hydrogen evolution associated with the formation of H^+ ions and derived from an increase in applied current or electrical potential. However, the generation of H^+ is controversial because this species has never been detected experimentally. On the other hand, if Mg^+ could exist in the solution, it would be highly reactive and have a short lifetime of about a few microseconds. The mechanism for the formation of monovalent Mg is associated with Equations (5.7) and (5.8), where Mg^+ ions are produced as intermediate species (Equation (5.7)). They subsequently react with water, leading to the evolution of hydrogen (Equation (5.8)) [48].

$$Mg_{(s)} \longrightarrow Mg^+_{(aq)} + e^- \quad (5.7)$$

$$2Mg^+_{(aq)} + 2H^+_{(aq)} \longrightarrow 2Mg^{2+}_{(aq)} + H_{2(g)} \quad (5.8)$$

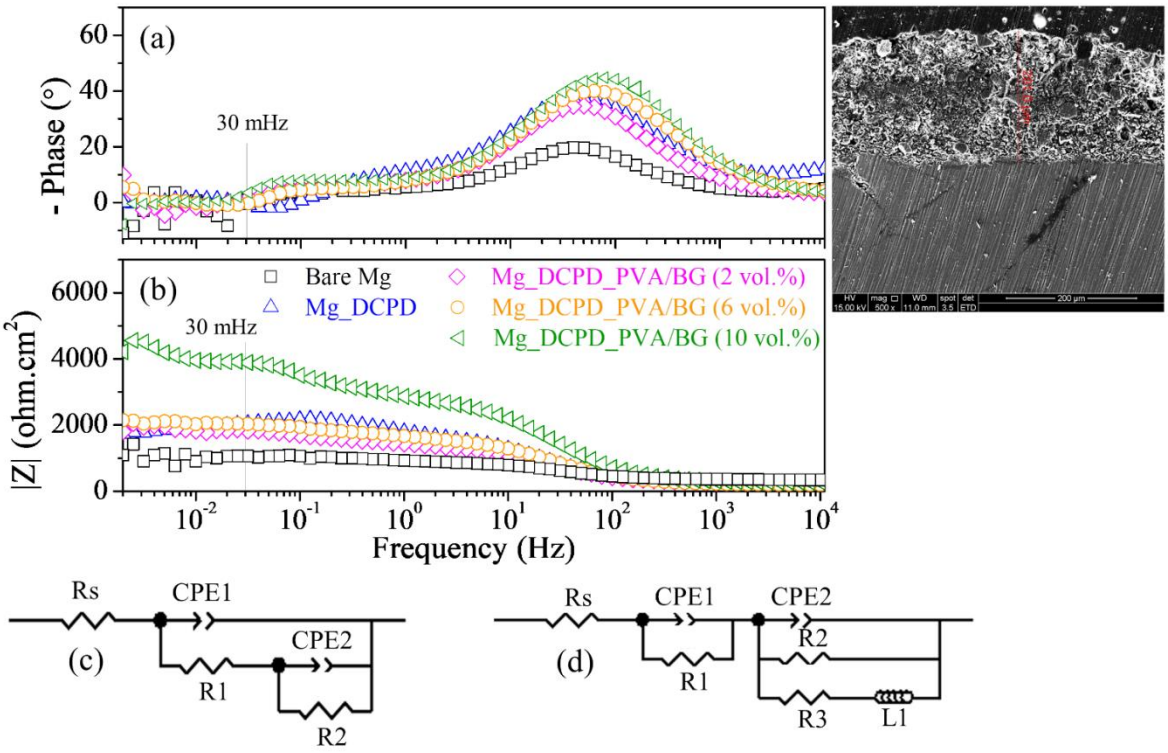

Figure 30 – Bode plots obtained from EIS tests: (a) phase angle and (b) impedance modulus as a function of frequency. Equivalent electrical circuits evaluated for (c) bare Mg and Mg_DCPD_PVA/BG, and (d) Mg_DCPD. Inset: cross-sectional SEM micrograph of Mg_DCPD_PVA/BG (10 vol.%).

CPE1 is associated with salts and corrosion products deposited on the loose outer layer of Mg, while CPE2 is due to an inner layer. Figures 30c and 30d are ascribed to Mg_DCPD_PVA/BG and Mg_DCPD, respectively. In such cases, CPE1 corresponds to the capacitive properties of the PVA/BG coating, where CPE2 is due to either an inner layer or the substrate/layer interface. R1 and R2 are related to the DCPD layer and a charge transfer resistance at the substrate/layer interface. An inductive loop L1 can be observed at low frequencies, and it has been assigned to the adsorption of Mg^{2+} ions at the solution/electrode interface. The electrical resistance R3 is attributed to these ions [49,50].

The values of |Z| assessed at 30 mHz were 1063 $\Omega.cm^2$, 2037 $\Omega.cm^2$, 1819 $\Omega.cm^2$, 2037 $\Omega.cm^2$, and 3890 $\Omega.cm^2$ for Mg, Mg_DCPD, Mg_DCPD_PVA/BG (2 vol.%), Mg_DCPD_PVA/BG (6 vol.%), Mg_DCPD_PVA/BG (10 vol.%), respectively. This frequency was taken as a reference because, at this value, the contributions due to resistive effects of SBF and the relaxation of adsorbed ions are minimized. The higher the value of |Z|, the more corrosion resistant the sample is. Therefore, the deposition of DCPD and PVA/BG

(10 vol.%) films significantly improved the corrosion resistance of Mg as the value of |Z| for this material changed from 1063 $\Omega.cm^2$ to 3890 $\Omega.cm^2$ after this step. This behavior could be associated with the thickness of the prepared coating. The thickness (h – m) of coatings obtained by dip-coating is described by the Landau-Levich equation [51] (Equation (5.9)), where η represents the solution viscosity (Pa.s), ν the withdrawal speed ($m.s^{-1}$), ρ the solution density ($kg.m^{-3}$), g the gravity acceleration (9.8 $m.s^{-2}$) and γ_{LV} the surface tension at the liquid-vapor interface ($N.m^{-1}$).

$$h = 0.94 \frac{(\eta.\upsilon)^{2/3}}{\gamma_{LV}{}^{1/6}.(\rho.g)^{1/2}} \quad (5.9)$$

We observed that the increase of the BG loading in the starting solution (deionized water + CA + PVA + BG) significantly increased its viscosity. Consequently, thicker coatings were obtained, which could justify the higher corrosion resistance of Mg_DCPD_PVA+BG (10 vol.%) compared to the other samples prepared in this study. As observed in the inset displayed in Figure 30b, the coating present on Mg_DCPD_PVA+BG (10 vol.%) was about 200 μm thick. Thinner coatings were noted for samples containing lower BG concentrations.

In a previous work [18], we investigated the corrosion resistance of DCPD-coated Mg specimens using Hank's balanced salt solution (HBSS). The value evaluated for |Z| at 30 mHz for the most resistant sample was 16×10^3 $\Omega.cm^2$. As already addressed, we observed in this work a |Z| value of about 3890 $\Omega.cm^2$ at 30 mHz for Mg_DCPD_PVA/BG (10 vol.%), revealing that it exhibits a lower corrosion resistance. At this point, it is worth discussing the corrosion behavior of Mg when soaked in either HBSS or SBF. SBF has a concentration of HCO_3^- ions around 4.2 $mmol.L^{-1}$, while this loading is 27 $mmol.L^{-1}$ in HBSS. It has been reported that a high concentration of HCO_3^- ions can slow down the Mg corrosion due to the precipitation of protective carbonates on its surface. Since SBF has a lower concentration of these species than HBSS, the degradation of Mg is more favored in the former than in the latter. Despite using a harsh chemical medium, the samples prepared in this work showed good corrosion resistance. From this finding, it is clear that the deposition of the PVA/BG films significantly improved the corrosion resistance of Mg.

Li *et al.* [52] investigated the corrosion behavior of an AZ31 Mg alloy in SBF after the deposition of DCPD/PLGA (poly(lactic-co-glycolic acid)) coatings on it. The authors observed that the values of |Z| at 0.01 Hz for the DCPD coating were higher than those evaluated for the

bare alloy. Moreover, an inductive loop was observed in all curves in the low-frequency region between 0.01 and 1 Hz. This loop is because of the relaxation reaction of intermediate products formed between the substrate and DCPD coating. Similar behavior was observed in this work for the bare Mg and Mg_DCPD. However, the Mg_DCPD_PVA/BG samples showed no such inductive loop, probably because Mg has uniform corrosion, unlike the AZ31 Mg alloy, which has localized corrosion [53].

5.3.3. BIOLOGICAL ASSAYS

- SOAKING TESTS IN SBF

Figures 31a and 31b show SEM micrographs of bare Mg and Mg_DCPD_PVA/BG (10 vol.%) after soaking in SBF for 7 days. While Mg experienced a noticeable degradation (Figure 31a), Mg_DCPD_PVA/BG (10 vol.%) gave rise to HAp crystals, as evidenced by the nodules highlighted in these images (Figure 31b). The mechanism of Mg corrosion is given in Equations (1) to (8). The formation of HAp in Mg_DCPD_PVA/BG (10 vol.%) was observed for soaking times as short as 1 day, reinforcing the high biocompatibility of the prepared composites. The inset of Figure 31b exhibits an SEM image of this composite after 21 soaking days. The presence of HAp nodules is clearly noticed in this micrograph.

Figure 32 brings FTIR spectra taken for Mg_DCPD_PVA/BG (10 vol.%) before and after its soaking in SBF for different times. A reference spectrum collected for HAp is also shown for reference purposes. The main absorption bands of HAp are observed at 560 cm^{-1}, 600 cm^{-1}, and 1020 cm^{-1}. Such bands have been attributed to PO_4^{3-} groups present in HAp [54]. These bands are observed in Mg_DCPD_PVA/BG (10 vol.%) and become more noticeable the longer the soaking time in SBF.

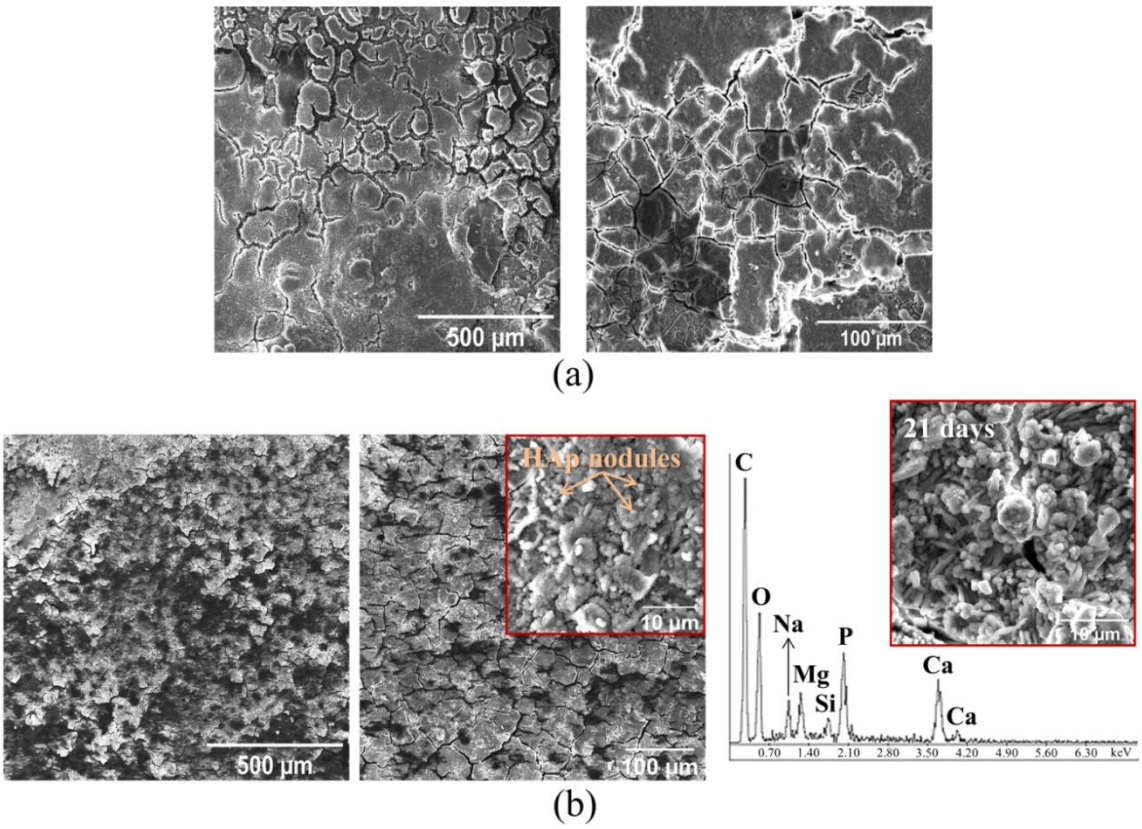

Figure 31 – SEM micrographs of (a) bare Mg and (b) Mg_DCPD_PVA/BG (10 vol.%) after 7 days of soaking in SBF. The EDS spectrum exhibited in Figure 7b was taken at a HAp nodule. The inset displayed in this image brings an SEM micrograph of Mg_DCPD_PVA/BG (10 vol.%) after 21 days of soaking in SBF.

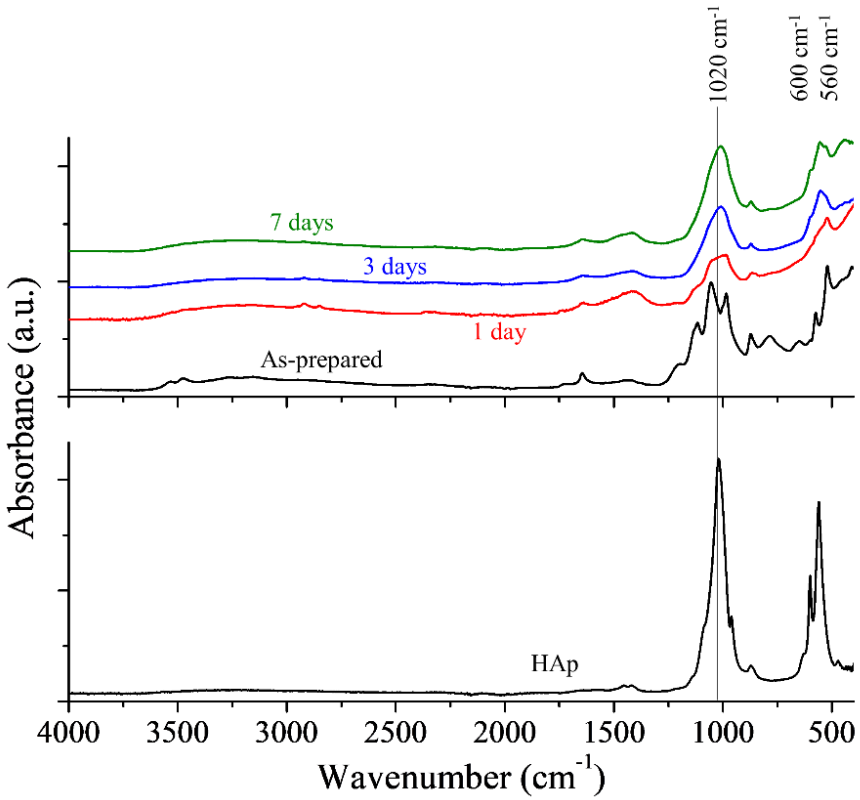

Figure 32 – ATR-FTIR spectra collected for Mg_DCPD_PVA/BG (10 vol.%) before and after immersion in SBF for 1, 3, and 7 days. A reference spectrum taken for a HAp sample is also exhibited.

Figure 33 depicts XRD patterns obtained for Mg_DCPD_PVA/BG (10 vol.%) before and after soaking in SBF for 7 days. Diffraction lines ascribed to Mg and DCPD are noticed in this material before the immersion in SBF. On the other hand, peaks associated with HAp are observed after its soaking in SBF for 7 days, which is in line with SEM, EDS, and FTIR (Figures 31 and 32).

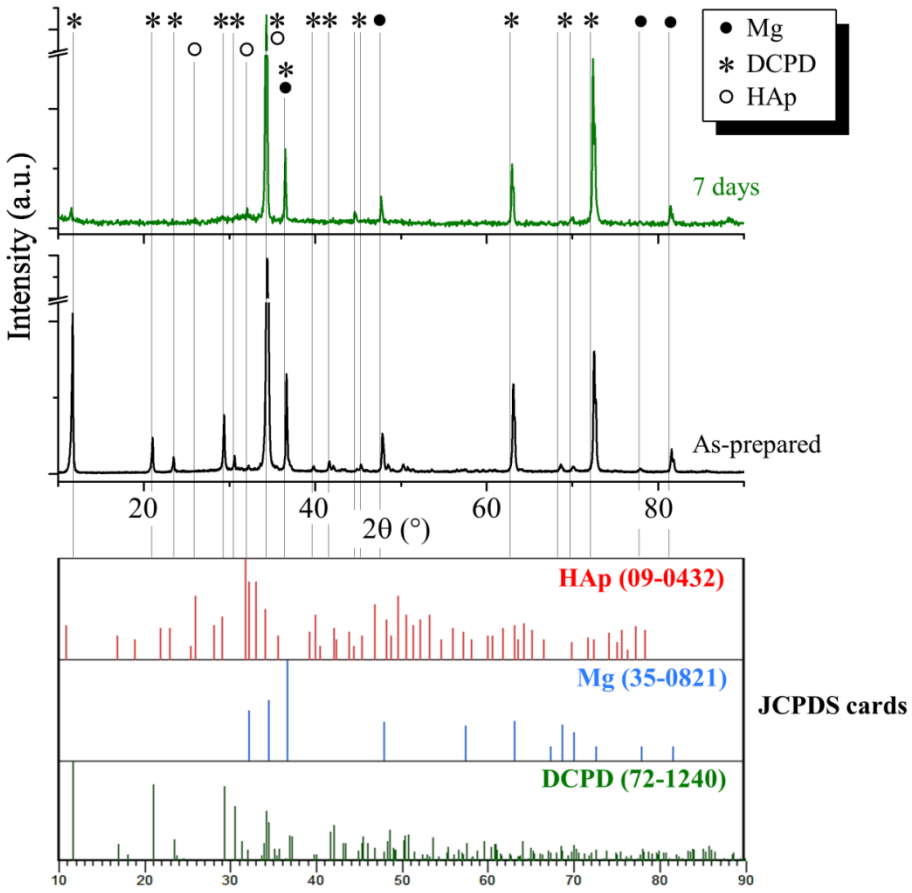

Figure 33 – DRX patterns of Mg_DCPD_PVA/BG (10 vol.%) (a) before and (b) after its soaking in SBF for 7 days. The JCPDS cards used the reference for HAp, Mg, and DCPD are also displayed for comparison purposes.

The PVA sample used in this work has both a low molecular weight (M_w = 9,000 – 10,000) and a low degree of hydrolysis (80%). These properties confer to this material a high solubility in water-based systems. Consequently, this polymer is rapidly biodegraded in biological media, allowing it to be easily eliminated by the human body [55]. Mansur and co-workers [56–58] investigated the degradation in SBF of PVA samples with the same molecular weight as that used here. They reported that PVA shows fast degradation in SBF, reaching a mass loss of about 50% after a soaking time of about 100 h. However, it did not show an additional mass loss after reaching this plateau, even after 500 h of soaking. Regardless of the fast degradation of PVA, the composite films tested here increased the corrosion resistance of Mg (Figure 30) and promoted a rapid formation of HAp crystals (Figures 31 to 33).

Mansur *et al.* [56–58] evaluated the use of glutaraldehyde as a cross-linker to increase the chemical stability of PVA. CA has also been widely used as a cross-linker to PVA. According to Salihu *et al.* [59], biomaterials cross-linked with CA, also called citrate-based biomaterials (CBBs), exhibit advanced *in vitro* and *in vivo* properties, making them suitable for various biomedical applications. Moreover, it has been reported that CA can also enhance the pH-responsiveness and antibacterial activity of PVA due to the presence of free carboxylic acid groups in the former [55]. It also deserves to mention that CA is inexpensive, environmentally friendly, and safe. Aiming to study the chemical stability of the composite films prepared here, we conducted the chemical modification of PVA with CA by stirring these materials in the presence of water at 90 °C for 24 h. During this step, CA can create cross-links between adjacent PVA molecular chains. The as-obtained mixture was then used in the preparation of Mg_DCPD_PVA/BG (10 vol.%) as previously described. We examined the as-prepared composites by SEM after 7 days of soaking in SBF. These results are provided in Figure 34. Figures 34a, 34b, and 34c are ascribed to samples prepared using CA concentrations of 2, 6, 10 wt.% of the BG loading, respectively. The coating prepared with a 2 wt.% CA loading exhibited a high porosity and gave rise to an expressive concentration of HAp after 7 days of soaking in SBF. On the other hand, increasing the CA loading to 6 or 10 wt.% led to cracked coatings as well as a poorer formation of HAp. It has been reported that CA can inhibit the formation of calcium phosphate phases due to its strong chelation with Ca^{2+} ions [60], which could explain the absence of HAp crystals in the sample prepared with a 10 wt.% CA loading (Figure 34c). Some HAp nodules are noticed in Figure 34b, but cracks are also observed on it. We noticed that the addition of CA at concentrations of 6 and 10 wt.% caused a significant increase in the viscosity of the dipping solution, which could favor the defects formation in the prepared coatings. Consequently, we recommend the addition of CA at a concentration of 2 wt.% of the BG loading to improve the chemical stability of PVA/BG films and maintain their biocompatibility. Nonetheless, it is worth stressing that despite the rapid degradation of the PVA sample used here, the prepared films increased the corrosion resistance of Mg and induced the formation of HAp. The chemical modification of PVA with CA will be addressed in more depth in a forthcoming paper.

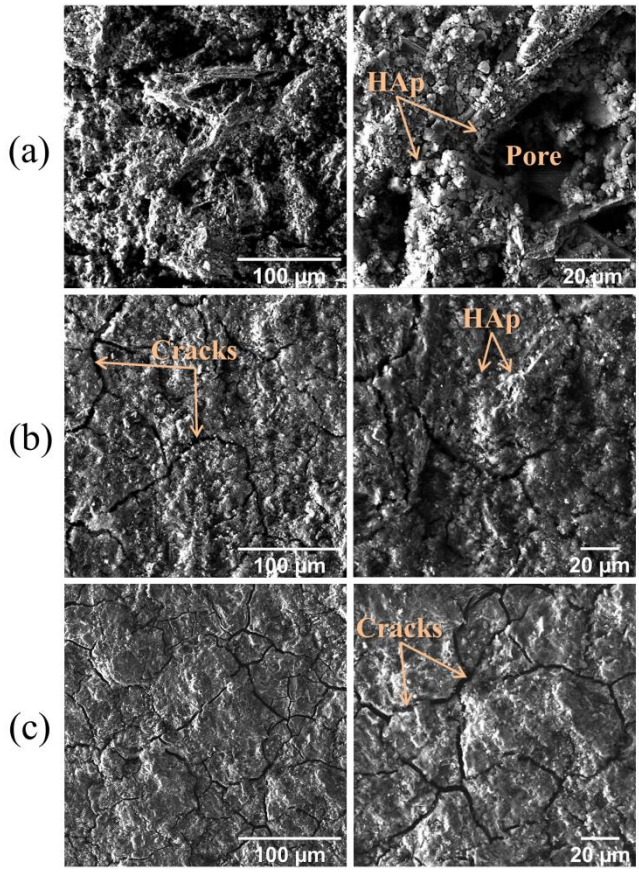

Figure 34- SEM micrographs of Mg_DCPD_PVA/BG (10 vol.%) samples prepared using CA as a cross-linker for PVA. The concentrations of CA were kept at (a) 2 wt.%, (b) 6 wt.%, and (c) 10 wt% of the BG loading. The scale bars exhibited in these images correspond to either 20 µm or 100 µm.

- FLOW CYTOMETRY

As Mg_DCPD_PVA/BG (10 vol.%) was the best performing sample in terms of corrosion behavior and HAp formation, it was used in the flow cytometry assays. Figure 35 displays the results obtained in these tests. Figures 35a and 35b show the scattering of the laser beam along its path (FSC) and its side scattering (SSC) measured at an angle of ninety degrees. FSC is proportional to the cell diameter and is mainly due to light diffraction at the cell surface. SCC, on the other hand, is associated with the light refracted or reflected at the interface between the laser and intracellular structures, providing information about the granularity of the examined cells. Figures 35a and 35b reveal that the cultured cells have a significant homogeneity in terms of size and structure. Similar patterns were also taken for the negative control group and are not shown. Figure 35c depicts SSC as a function of FSC. This graph reveals a low cytotoxicity profile, where a significant population of live cells (red dots) is observed. Figure 35.d displays

histograms where the patterns obtained for both the composite and the negative control group are superimposed. These histograms were obtained by using a fluorochrome compound with a maximum emission at 450 nm, which reacts with amines radicals present on the cells' surface and in the intracellular medium. Consequently, dead cells show an increased fluorescence when compared to living cells. The similar profile shown by the composite and negative control group reveals high cell viability of the former, which agrees with Figure 35c. A cell viability of (93.9 ± 1.6) % was evaluated, indicating that the examined composite did not interfere with the culture of the human cells used here. Figure 36 (supplementary material-Appendix) displays images taken by light microscopy for HEK-293 cells from the negative control group or seeded on the Mg_DCPD_PVA/BG (10 vol.%) surface. The cells identified in these images show similar morphologies, revealing that cell growth was not affected by the presence of Mg_DCPD_PVA/BG (10 vol.%).

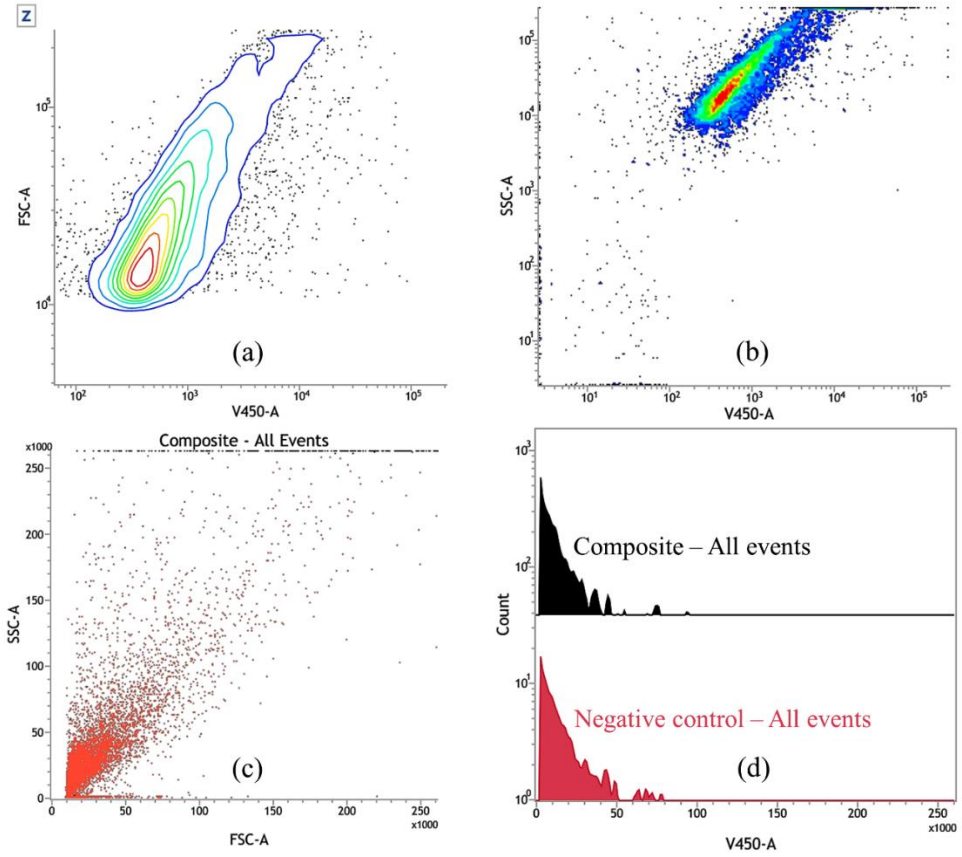

Figure 35 - Flow cytometry results of HEK-293 cells seeded on the surface of Mg_DCPD_PVA/BG (10 vol.%). (a) Contour plot of FSC versus V450-A. (b) Density plot of SSC versus V450-A. (c) SSC versus FSC, where the live cells are represented by red dots and the dead cells by purple dots. (d) Histograms of cells cultured on the composite surface and in the negative control group as a function of V450-A.

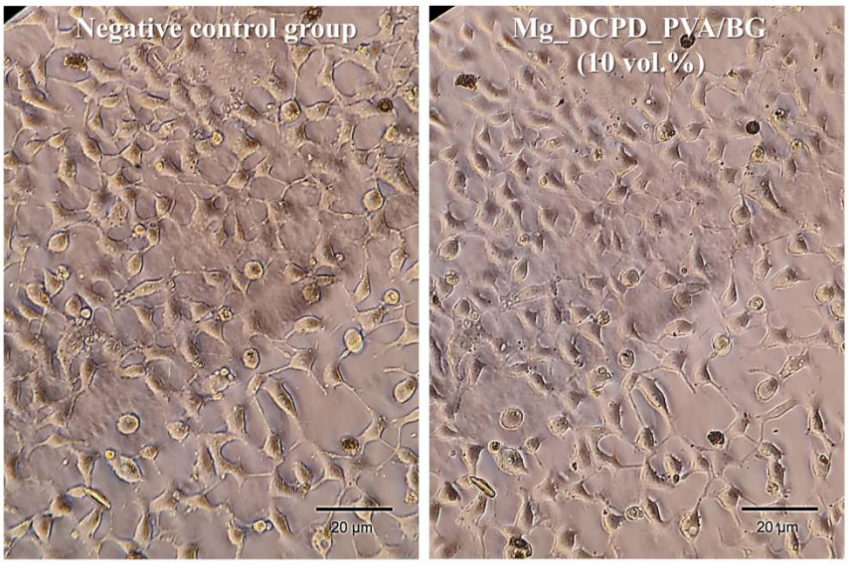

Figure 36- Light microscopy images of HEK-293 cells cultured in the negative control group or seeded on the Mg_DCPD_PVA/BG (10 vol.%) surface. The scale bars displayed in these images correspond to 20 µm.

Additional testing is needed to fully understand the biological behavior of the composites prepared here. Such tests could involve using human cells other than those used here and performing *in vivo* assays. However, such an approach is beyond the scope of this study. We successfully prepared composite coatings capable of providing corrosion protection to Mg, aiming to allow its use as a bone graft. Moreover, we showed that these materials did not present toxicity to immortalized human embryonic kidney cells, which reinforces their promising use as biomaterials.

5.4. CONCLUSIONS

In this work, we successfully modified the surface of hot-rolled Mg plates aiming to improve their corrosion behavior. Mg was initially coated with a DCPD layer by immersing it in a phosphating bath at room temperature for 24 h. Next, it was coated with a PVA/BG film by a dip-coating approach. PVA molecular chains played an essential role in keeping BG particles adhered to the Mg surface. We observed that the composite coatings increased the corrosion protection of Mg, which was verified in terms of |Z|: it increased from 1063 $\Omega.cm^2$ to 3890 $\Omega.cm^2$ after the deposition step. It was shown that the solubility of PVA in biological media can be tailored by cross-linking its adjacent molecular chains with CA (we suggest using a CA loading of 1 wt.% relative to the BG concentration). The sample containing a BG loading of 10 vol.% was the one with the highest corrosion resistance, which is related to the large

thickness of the coating obtained (about 200 μm). Moreover, this sample favored a rapid formation of HAp crystals on the composite surface, revealing its biocompatibility. Flow cytometry assays pointed out that these composites present high cell viability (over 90%) when human embryonic kidney cells are considered, which reinforces their promising use as biomaterials.

ACKNOWLEDGEMENTS

The authors thank the financial support from CAPES (PROEX) and CNPq (305013/2017-3 and 301423/2018-0). We also thank the UFMG microscopy center, Prof. Dagoberto Brandão, and Patrícia Azevedo for the support provided in the SEM analyses. Prof. Paulo Brandão, Prof. Vicente Buono, and Samuel Lima are recognized for the FTIR and XRD tests.

5.5. REFERENCES

[1] J.S. Han, H.K. Song, Bone substitutes: From basic to current update, J. Korean Fract. Soc. 33 (2020) 238–244. https://doi.org/10.12671/jkfs.2020.33.4.238.

[2] M.J. Meagher, H.E. Weiss-Bilka, M.E. Best, J.D. Boerckel, D.R. Wagner, R.K. Roeder, Acellular hydroxyapatite-collagen scaffolds support angiogenesis and osteogenic gene expression in an ectopic murine model: Effects of hydroxyapatite volume fraction, J. Biomed. Mater. Res. - Part A. 104 (2016) 2178–2188. https://doi.org/10.1002/jbm.a.35760.

[3] W. Wang, K.W.K. Yeung, Bone grafts and biomaterials substitutes for bone defect repair: A review, Bioact. Mater. 2 (2017) 224–247. https://doi.org/10.1016/j.bioactmat.2017.05.007.

[4] H. Breme, V. Biehl, N. Reger, E. Gawalt, Chapter 1a Metallic Biomaterials: Introduction, in: W. Murphy, J. Black, G. Hastings (Eds.), Handbook of Biomaterial Properties, Springer New York, New York, NY, 2016: pp. 151–158. https://doi.org/10.1007/978-1-4939-3305-1_14.

[5] L.C. Trincă, M. Fântânariu, C. Solcan, A.E. Trofin, L. Burtan, D.M. Acatrinei, S. Stanciu, B. Istrate, C. Munteanu, In vivo degradation behavior and biological activity of some new Mg–Ca alloys with concentration's gradient of Si for bone grafts, Appl. Surf. Sci. 352 (2015) 140–150. https://doi.org/10.1016/j.apsusc.2015.03.136.

[6] L. Li, M. Zhang, Y. Li, J. Zhao, L. Qin, Y. Lai, Corrosion and biocompatibility improvement of magnesium-based alloys as bone implant materials: A review, Regen. Biomater. 4 (2017) 129–137. https://doi.org/10.1093/rb/rbx004.

[7] L.-C. Zhang, M. Xu, Y.-D. Hu, F. Gao, T. Gong, T. Liu, X. Li, C.-J. Pan, Biofunctionization of biodegradable magnesium alloy to improve the in vitro corrosion resistance and biocompatibility, Appl. Surf. Sci. 451 (2018) 20–31. https://doi.org/10.1016/j.apsusc.2018.04.235.

[8] S. Höhn, S. Virtanen, A.R. Boccaccini, Protein adsorption on magnesium and its alloys: A review, Appl. Surf. Sci. 464 (2019) 212–219. https://doi.org/10.1016/j.apsusc.2018.08.173.

[9] M. Pogorielov, E. Husak, A. Solodivnik, S. Zhdanov, Magnesium-based biodegradable alloys: Degradation, application, and alloying elements, Interv. Med. Appl. Sci. 9 (2017) 27–38. https://doi.org/10.1556/1646.9.2017.1.04.

[10] C.L.P. Silva, A.C. Oliveira, C.G.F. Costa, R.B. Figueiredo, M. de Fátima Leite, M.M. Pereira, V.F.C. Lins, T.G. Langdon, Effect of severe plastic deformation on the biocompatibility and corrosion rate of pure magnesium, J. Mater. Sci. 52 (2017) 5992–6003. https://doi.org/10.1007/s10853-017-0835-x.

[11] J. Gonzalez, R.Q. Hou, E.P.S. Nidadavolu, R. Willumeit-Römer, F. Feyerabend, Magnesium degradation under physiological conditions – Best practice, Bioact. Mater. 3 (2018) 174–185. https://doi.org/10.1016/j.bioactmat.2018.01.003.

[12] Y. Chen, J. Li, W. Yang, S. Gao, R. Cao, Enhanced corrosion protective performance of graphene oxide-based composite films on AZ31 magnesium alloys in 3.5 wt% NaCl solution, Appl. Surf. Sci. 493 (2019) 1224–1235. https://doi.org/10.1016/j.apsusc.2019.07.101.

[13] Y. Wu, Y. Wang, S. Tian, Y. Jing, J. Zhuang, L. Guo, D. Jia, Y. Zhou, Hydrothermal fabrication of rGO/Apatite layers on AZ31 magnesium alloy for enhanced bonding strength and corrosion resistance, Appl. Surf. Sci. 470 (2019) 430–438. https://doi.org/10.1016/j.apsusc.2018.11.086.

[14] J. Kuang, Z. Ba, Z. Li, Z. Wang, J. Qiu, The study on corrosion resistance of superhydrophobic coatings on magnesium, Appl. Surf. Sci. 501 (2020) 144137. https://doi.org/10.1016/j.apsusc.2019.144137.

[15] Z. Xi, C. Tan, L. Xu, N. Yang, Q. Li, Preparation of novel functional Mg/O/PCL/ZnO

composite biomaterials and their corrosion resistance, Appl. Surf. Sci. 351 (2015) 410–415. https://doi.org/10.1016/j.apsusc.2015.05.163.

[16] M.D. Wadge, J. McGuire, B.V.T. Hanby, R.M. Felfel, I. Ahmed, D.M. Grant, Tailoring the degradation rate of magnesium through biomedical nano-porous titanate coatings, J. Magnes. Alloy. 9 (2021) 336–350. https://doi.org/10.1016/j.jma.2020.07.001.

[17] M. Esmaily, J.E. Svensson, S. Fajardo, N. Birbilis, G.S. Frankel, S. Virtanen, R. Arrabal, S. Thomas, L.G. Johansson, Fundamentals and advances in magnesium alloy corrosion, Prog. Mater. Sci. 89 (2017) 92–193. https://doi.org/10.1016/j.pmatsci.2017.04.011.

[18] J. de O. Braga, S.M. de Carvalho, L.M.C. Silva, R.B. Soares, V.F.C. Lins, E.M. Mazzer, M. Houmard, R.B. Figueiredo, E.H.M. Nunes, Fabrication and characterization of dicalcium phosphate coatings deposited on magnesium substrates by a chemical conversion route, Surf. Coatings Technol. 386 (2020) 125505. https://doi.org/10.1016/j.surfcoat.2020.125505.

[19] F. Cao, Z. Shi, G.-L. Song, M. Liu, M.S. Dargusch, A. Atrens, Influence of hot rolling on the corrosion behavior of several Mg–X alloys, Corros. Sci. 90 (2015) 176–191. https://doi.org/10.1016/j.corsci.2014.10.012.

[20] Y. Zhao, Y. Zhou, X. Wu, L. Wang, L. Xu, S. Wei, A facile method for electrospinning of Ag nanoparticles/poly (vinyl alcohol)/carboxymethyl-chitosan nanofibers, Appl. Surf. Sci. 258 (2012) 8867–8873. https://doi.org/10.1016/j.apsusc.2012.05.106.

[21] A. Kumar, S.S. Han, PVA-based hydrogels for tissue engineering: A review, Int. J. Polym. Mater. Polym. Biomater. 66 (2017) 159–182. https://doi.org/10.1080/00914037.2016.1190930.

[22] N. Rocton, H. Oudadesse, B. Lefeuvre, H. Peisker, K. Rbii, Fine analysis of interaction mechanism of bioactive glass surface after soaking in SBF solution: AFM and ICP-OES investigations, Appl. Surf. Sci. 505 (2020) 144076. https://doi.org/10.1016/j.apsusc.2019.144076.

[23] L.L. Hench, R.J. Splinter, W.C. Allen, T.K. Greenlee, Bonding mechanisms at the interface of ceramic prosthetic materials, J. Biomed. Mater. Res. 5 (1971) 117–141. https://doi.org/10.1002/jbm.820050611.

[24] D.M.M. dos Santos, S.M. de Carvalho, M.M. Pereira, M. Houmard, E.H.M. Nunes, Freeze-cast composite scaffolds prepared from sol-gel derived 58S bioactive glass and

polycaprolactone, Ceram. Int. 45 (2019) 9891–9900. https://doi.org/10.1016/j.ceramint.2019.02.030.

[25] M.M. Pereira, A.E. Clark, L.L. Hench, Calcium phosphate formation on sol-gel-derived bioactive glassesin vitro, J. Biomed. Mater. Res. 28 (1994) 693–698. https://doi.org/10.1002/jbm.820280606.

[26] T. Kokubo, H. Takadama, How useful is SBF in predicting in vivo bone bioactivity?, Biomaterials. 27 (2006) 2907–2915. https://doi.org/10.1016/j.biomaterials.2006.01.017.

[27] M.N. Rahaman, D.E. Day, B. Sonny Bal, Q. Fu, S.B. Jung, L.F. Bonewald, A.P. Tomsia, Bioactive glass in tissue engineering, Acta Biomater. 7 (2011) 2355–2373. https://doi.org/10.1016/j.actbio.2011.03.016.

[28] M. Elbadawi, Z.J. Wally, I.M. Reaney, Porous hydroxyapatite-bioactive glass hybrid scaffolds fabricated via ceramic honeycomb extrusion, J. Am. Ceram. Soc. 101 (2018) 3541–3556. https://doi.org/10.1111/jace.15514.

[29] ISO/International Organization for Standardization, ISO 10993-5 Biological evaluation of medical devices - Part 5: Tests for cytotoxicity: in vitro methods, Int. Organ. Stand. 3 Ed (2009) 42. https://doi.org/10.1016/j.transproceed.2009.12.077.

[30] M. Fuchs, E. Gentleman, S. Shahid, R.G. Hill, D.S. Brauer, Therapeutic ion-releasing bioactive glass ionomer cements with improved mechanical strength and radiopacity, Front. Mater. 2 (2015) 63–74. https://doi.org/10.3389/fmats.2015.00063.

[31] A. Hoppe, N.S. Güldal, A.R. Boccaccini, A review of the biological response to ionic dissolution products from bioactive glasses and glass-ceramics, Biomaterials. 32 (2011) 2757–2774. https://doi.org/10.1016/j.biomaterials.2011.01.004.

[32] Z. Imran, Bioactive glass: A material for the future, World J. Dent. 3 (2012) 199–201. https://doi.org/10.5005/jp-journals-10015-1156.

[33] J. McAndrew, C. Efrimescu, E. Sheehan, D. Niall, Through the looking glass; Bioactive glass S53P4 (BonAlive®) in the treatment of chronic osteomyelitis, Ir. J. Med. Sci. 182 (2013) 509–511. https://doi.org/10.1007/s11845-012-0895-5.

[34] H.Y. Jung, R.K. Gupta, E.O. Oh, Y.H. Kim, C.M. Whang, Vibrational spectroscopic studies of sol-gel derived physical and chemical bonded ORMOSILs, J. Non. Cryst. Solids. 351

(2005) 372–379. https://doi.org/10.1016/j.jnoncrysol.2005.01.004.

[35] H. Yoshino, K. Kamiya, H. Nasu, IR study on the structural evolution of sol-gel derived SiO_2 gels in the early stage of conversion to glasses, J. Non. Cryst. Solids. 126 (1990) 68–78. https://doi.org/10.1016/0022-3093(90)91024-L.

[36] R.M. Almeida, C.G. Pantano, Structural investigation of silica gel films by infrared spectroscopy, J. Appl. Phys. 68 (1990) 4225–4232. https://doi.org/10.1063/1.346213.

[37] A. Li, H. Ren, Y. Cui, C. Wang, X. Zhou, H. Lin, D. Qiu, Detailed structure of a new bioactive glass composition for the design of bone repair materials, J. Non. Cryst. Solids. 475 (2017) 10–14. https://doi.org/10.1016/j.jnoncrysol.2017.07.027.

[38] P.J. Ogren, Using the asymmetric stretch band of atmospheric CO_2 to obtain the C=O bond length, J. Chem. Educ. 79 (2002) 117–119. https://doi.org/10.1021/ed079p117.

[39] M. Thommes, K. Kaneko, A. V. Neimark, J.P. Olivier, F. Rodriguez-Reinoso, J. Rouquerol, K.S.W. Sing, Physisorption of gases, with special reference to the evaluation of surface area and pore size distribution (IUPAC Technical Report), Pure Appl. Chem. 87 (2015) 1051–1069. https://doi.org/10.1515/pac-2014-1117.

[40] M.A.F. Zaludin, Z.A. Zahid Jamal, M.N. Derman, M.Z. Kasmuin, Fabrication of calcium phosphate coating on pure magnesium substrate via simple chemical conversion coating: Surface properties and corrosion performance evaluations, J. Mater. Res. Technol. 8 (2019) 981–987. https://doi.org/10.1016/j.jmrt.2018.06.017.

[41] I. Petrov, B. Šoptrajanov, N. Fuson, J.R. Lawson, Infra-red investigation of dicalcium phosphates, Spectrochim. Acta Part A Mol. Spectrosc. 23 (1967) 2637–2646. https://doi.org/10.1016/0584-8539(67)80155-7.

[42] J. Xu, I.S. Butler, D.F.R. Gilson, FT-Raman and high-pressure infrared spectroscopic studies of dicalcium phosphate dihydrate ($CaHPO_4 \cdot 2H_2O$) and anhydrous dicalcium phosphate ($CaHPO_4$), Spectrochim. Acta - Part A Mol. Biomol. Spectrosc. 55 (1999) 2801–2809. https://doi.org/10.1016/S1386-1425(99)00090-6.

[43] A. Zavattini, V.P. Feitosa, F. Mannocci, F. Foschi, A. Babbar, A. Luzi, L. Ottria, F. Mangani, I. Casula, S. Sauro, Bonding ability of experimental resin-based materials containing (ion-releasing)-microfillers applied on water-wet or ethanol-wet root canal dentine, Int. J. Adhes. Adhes. 54 (2014) 214–223.

https://doi.org/https://doi.org/10.1016/j.ijadhadh.2014.06.007.

[44] A. Kharazmi, N. Faraji, R.M. Hussin, E. Saion, W.M.M. Yunus, K. Behzad, Structural, optical, opto-thermal and thermal properties of ZnS–PVA nanofluids synthesized through a radiolytic approach, Beilstein J. Nanotechnol. 6 (2015) 529–536. https://doi.org/10.3762/bjnano.6.55.

[45] J. Gaume, A. Rivaton, S. Thérias, J.-L. Gardette, Influence of nanoclays on the photochemical behaviour of poly(vinyl alcohol), Polym. Degrad. Stab. 97 (2012) 488–495. https://doi.org/10.1016/j.polymdegradstab.2012.01.022.

[46] I. V Smirnov, J. V Rau, M. Fosca, A. De Bonis, A. Latini, R. Teghil, V.I. Kalita, A.Y. Fedotov, S. V Gudkov, A.E. Baranchikov, V.S. Komlev, Structural modification of titanium surface by octacalcium phosphate via Pulsed Laser Deposition and chemical treatment, Bioact. Mater. 2 (2017) 101–107. https://doi.org/10.1016/j.bioactmat.2017.03.002.

[47] D. Xu, F. Lei, H. Chen, L. Yin, Y. Shi, I. Xie, One-step hydrothermal synthesis and optical properties of self-quenching-resistant carbon dots towards fluorescent ink and as nanosensors for Fe^{3+} detection, RSC Adv. 9 (2019) 8290–8299. https://doi.org/10.1039/C8RA10570G.

[48] S. Bender, J. Goellner, A. Heyn, S. Schmigalla, A new theory for the negative difference effect in magnesium corrosion, Mater. Corros. 63 (2012) 707–712. https://doi.org/10.1002/maco.201106225.

[49] Y. Xin, T. Hu, P.K. Chu, Degradation behaviour of pure magnesium in simulated body fluids with different concentrations of HCO_3^-, Corros. Sci. 53 (2011) 1522–1528. https://doi.org/10.1016/j.corsci.2011.01.015.

[50] W. Zai, X. Zhang, Y. Su, H.C. Man, G. Li, J. Lian, Comparison of corrosion resistance and biocompatibility of magnesium phosphate (MgP), zinc phosphate (ZnP) and calcium phosphate (CaP) conversion coatings on Mg alloy, Surf. Coatings Technol. 397 (2020) 125919. https://doi.org/10.1016/j.surfcoat.2020.125919.

[51] L. Landau, B. Levich, Dragging of a liquid by a moving plate, in: P. Pelcé (Ed.), Dynamics of Curved Fronts, Academic Press, San Diego, 1988: pp. 141–153. https://doi.org/10.1016/B978-0-08-092523-3.50016-2.

[52] X. Li, Z. Weng, W. Yuan, X. Luo, H.M. Wong, X. Liu, S. Wu, K.W.K. Yeung, Y.

Zheng, P.K. Chu, Corrosion resistance of dicalcium phosphate dihydrate/poly(lactic-co-glycolic acid) hybrid coating on AZ31 magnesium alloy, Corros. Sci. 102 (2016) 209–221. https://doi.org/10.1016/j.corsci.2015.10.010.

[53] Z. Wen, C. Wu, C. Dai, F. Yang, Corrosion behaviors of Mg and its alloys with different Al contents in a modified simulated body fluid, J. Alloys Compd. 488 (2009) 392–399. https://doi.org/10.1016/j.jallcom.2009.08.147.

[54] H. Gheisari, E. Karamian, M. Abdellahi, A novel hydroxyapatite - Hardystonite nanocomposite ceramic, Ceram. Int. 41 (2015) 5967–5975. https://doi.org/10.1016/j.ceramint.2015.01.033.

[55] M. Sabzi, M.J. Afshari, M. Babaahmadi, N. Shafagh, pH-dependent swelling and antibiotic release from citric acid crosslinked poly(vinyl alcohol) (PVA)/nano silver hydrogels, Colloids Surfaces B Biointerfaces. 188 (2020) 110757. https://doi.org/10.1016/j.colsurfb.2019.110757.

[56] L.L.S. Dias, H.S. Mansur, C.L. Donnici, M.M. Pereira, Synthesis and characterization of chitosan-polyvinyl alcohol-bioactive glass hybrid membranes, Biomatter. 1 (2011) 114–119. https://doi.org/10.4161/biom.1.1.17449.

[57] H.S. Costa, A.A.P. Mansur, M.M. Pereira, H.S. Mansur, Engineered hybrid scaffolds of Poly(vinyl alcohol)/bioactive glass for potential bone engineering applications: Synthesis, characterization, cytocompatibility, and degradation, J. Nanomater. 2012 (2012) 1–16. https://doi.org/10.1155/2012/718470.

[58] H.S. Mansur, H.S. Costa, A.A.P. Mansur, M. Pereira, 3D-macroporous hybrid scaffolds for tissue engineering: Network design and mathematical modeling of the degradation kinetics, Mater. Sci. Eng. C. 32 (2012) 404–415. https://doi.org/10.1016/j.msec.2011.11.012.

[59] R. Salihu, S.I. Abd Razak, N. Ahmad Zawawi, M. Rafiq Abdul Kadir, N. Izzah Ismail, N. Jusoh, M. Riduan Mohamad, N. Hasraf Mat Nayan, Citric acid: A green cross-linker of biomaterials for biomedical applications, Eur. Polym. J. 146 (2021) 110271. https://doi.org/10.1016/j.eurpolymj.2021.110271.

[60] S.-H. Rhee, J. Tanaka, Effect of citric acid on the nucleation of hydroxyapatite in a simulated body fluid, Biomaterials. 20 (1999) 2155–2160. https://doi.org/10.1016/S0142-9612(99)00118-0.

6. CONSIDERAÇÕES FINAIS

6.1. CONCLUSÕES

É fato que o Mg, quando presente em meio fisiológico, possui alta taxa de degradação. Visando aumentar sua resistência à corrosão, nesse estudo buscou-se modificar a superfície desse material com revestimentos biocompatíveis. Com base nos resultados desta pesquisa, as seguintes conclusões são destacadas:

- Revestimentos de DCPD foram depositados com sucesso sobre o Mg laminado a quente por meio da sua imersão em banho fosfatizante. Os recobrimentos obtidos apresentaram boa aderência e espessuras entre 5 e 14 μm.

- Os recobrimentos de DCPD produzidos após 24 h de imersão em banho fosfatizante apresentaram maiores valores de módulos de impedância (|Z|) em comparação ao Mg sem recobrimento e aos demais recobertos e, consequentemente, melhor resposta à corrosão. Isso se deve ao filme formado apresentar elevada espessura e não possuir defeitos em sua estrutura.

- As amostras revestidas com DCPD e tratadas a 100 °C durante 6 h apresentaram defeitos superficiais. Essa característica teve grande influência no ensaio eletroquímico de EIS, comprometendo a resistência à corrosão dessas amostras.

- Em relação à cinética de formação de HAp em solução de Hank, observou-se que o Mg recoberto com DCPD depositado após 24 h de imersão apresentou uma rápida formação de HAp na superfície do material, sendo isto notado logo nas primeiras 24 h de imersão.

- Ensaios de MTT e LIVE/DEAD foram empregados na avaliação da citotoxicidade do Mg com DCDP (CaP-24 h) e Mg puro sem recobrimento. Foi observado que o material recoberto exibiu grande viabilidade, não se mostrando citotóxico às células testadas (viabilidade superior a 70%). Em contrapartida, o magnésio puro apresentou viabilidade inferior a 70%, justificado pela liberação de $H_{2(g)}$ durante a corrosão do Mg e pela formação de H_2O_2 no meio fisiológico, aumentado assim o estresse oxidativo das células presente no meio.

- Revestimentos biocompósitos (PVA/BG) com diferentes cargas de BG foram depositados sobre o Mg anteriormente recoberto com DCPD (CaP-24h) utilizando o método de dip-coating.

- O revestimento de PVA/BG com carga de 10% vol./vol. de BG apresentou melhor resposta no ensaio de EIS. Isso se deve à elevada espessura do recobrimento (cerca de 200 μm)

- A deposição do recobrimento biocompósito no Mg com DCPD (CaP-24h) aumentou o valor do módulo de impedância; o valor de |Z| que era de 1063 $\Omega.cm^2$ para Mg com DCPD aumentou para 3890 $\Omega.cm^2$ com a camada de PVA/BG na frequência de 30 mHz.

- As amostras preparadas foram imersas em SBF durante 21 dias. Porém, notou-se a formação de HAp na superfície do material biocompósito com 10% vol./vol. de BG após as primeiras 24 h de imersão.

- Ensaios de citometria de fluxo demonstraram uma alta viabilidade celular para o material recoberto com filme biocompósito (10% vol. de BG).

6.2. SUGESTÕES PARA TRABALHOS FUTUROS

- Realização de ensaios mecânicos do Mg revestido.

- Utilização de outros fluidos corporais simulados para comparação de resultados, uma vez que houve diferenças nos ensaios eletroquímicos realizados com HBSS e SBF.

- Desenvolvimento de metodologias para avaliação da taxa de biodegradação e da degradação total do Mg recoberto quando presente em meio corporal simulado.

- Utilização de diferentes agentes de formação de ligações cruzadas (*cross-linkers*) para redução da taxa de degradação/dissolução do PVA em meios aquosos.

- Produção de *scaffolds* de PVA/BG para avaliação por meio de ensaio gravimétrico da taxa de degradação desses materiais em meios corporais simulados.

APÊNDICE

- PROCESSAMENTO MECÂNICO E CARACTERIZAÇÃO DO Mg UTILIZADO NESSE ESTUDO

Os lingotes de Mg utilizados nesse trabalho foram fornecidos pela empresa Rima localizada em Bocaiúva-MG. Esse material possui pureza de 99,7 %p./p. segundo o fabricante. O Mg foi inicialmente conformado utilizando a técnica de laminação a quente a uma temperatura de 400 °C. Durante esse processo o rolo de laminação foi mantido a 25 °C. Foram realizados 4 passes com 20% de redução da espessura da amostra a cada passe até que se atingisse a espessura de 1 mm. O objetivo dessa etapa foi promover o refinamento de grão do Mg e garantir que ele exibisse resistência mecânica e geometria adequadas para sua utilização em implantes ósseos. Ademais, é descrito na literatura que o refinamento de grão do Mg promove também a melhoria da sua resistência à oxidação em meios fisiológicos.

Figura 37- Laminação do Mg comercialmente puro. (a) Mg passando através dos rolos de laminação e (b) Mg após o seu processamento.

A microestrutura do Mg após seu processamento foi avaliada por microscopia óptica (Figura 38). O tamanho de grão para a amostra fundida era próximo a 505 μm, enquanto as amostras deformadas por laminação apresentam grãos com tamanho em torno de 11,5 μm. A microestrutura do material fundido apresentou-se de forma heterogênea com grãos grosseiros,

enquanto na microestrutura do material laminado (Figura 38) nota-se grãos bimodais e alongados. Tal fato se deve pela temperatura de processamento ter sido maior que a temperatura de recristalização do Mg, o que leva à recristalização dinâmica do material. SILVA *et al.* (2017) também processaram amostras de Mg por laminação e encontraram valor de tamanho de grão igual à 16 µm, com microestrutura semelhante à observada desse estudo.

ft

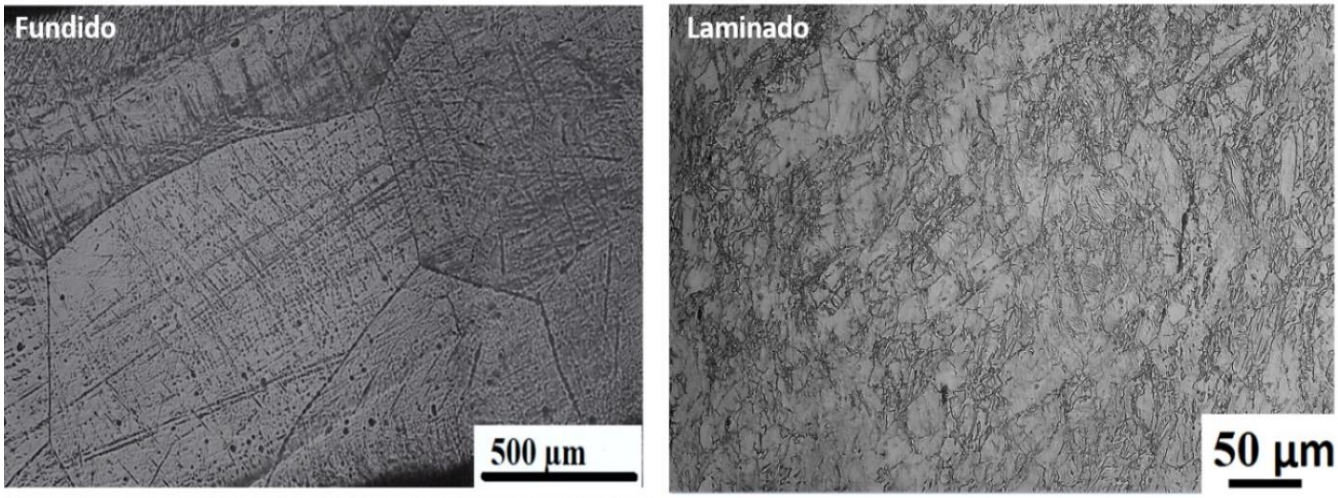

Figura 38- Microestrutura do Mg (a) fundido e (b) laminado.